Fermilab FERMILAB-THESIS-1997-23

space holder for signature page

A Search for Chargino-Neutralino Production at the Fermilab Tevatron Collider

by
Benn Tannenbaum

B.A., Physics, Grinnell College, 1990
M.S., Physics, Michigan State University, 1993

Doctor of Philosophy
Physics

December, 1997

To my parents,
for teaching me to ask ‘why’

Acknowledgements

The road to any Ph.D. is a long one. Mine, however, has been especially winding, and there are many people who contributed to this degree in one way or another.

Working as a member of a collaboration as large as CDF means nothing is done alone. Many people helped me greatly with my analysis, especially Stephan Lammel and Teruki Kamon. Jeff Wolinski, James Done, Steve Tether and Yukihiro Kato all helped in their own way. I also had many useful discussions with Michael Gold, Jerry Stephenson, Greg Anderson and Norman Gelfand. Naturally, without the rest of the collaboration we would have neither detector nor data.

Earning this degree took longer than it should have, and I almost gave up many times. Many people were very supportive and kept me going. Thanks to Todd Huffman for being my personal cheering section, to Tim Thomas for suggesting I transfer to UNM, and to John Matthews for taking the chance and accepting me. Thanks to the many people who kept me sane: Mike Jaeger in E. Lansing; Petar Maksimovic, Wasiq Bokhari, Tushar Shah, Steve Pappas, Randy Hans and Lenny Apanasevich in Batavia; and Steve Worm, Sheila Hutcherson, the Bruners and the Thomases in Albuquerque. Thanks to Norman Gelfand and the rest of the Friday lunch crowd. Thanks to Carl Bromberg and Joey Huston, my advisors at Michigan State University, for teaching me how to be a good experimentalist. To Mark Schneider, my advisor at Grinnell, for teaching me how (and why!) to keep a good logbook. To Andrew Hsieh, my Chinese History professor at Grinnell, for teaching me how to write. Many thanks to Will and Evelyn Freeman, my track coaches at Grinnell, for teaching me to push myself. Thanks to the people who played soccer and ultimate frisbee and went cycling. Nothing helps remove stress like kicking your collaborators in the shin.

Thanks to my parents for instilling in me a love of learning, a constant curiosity. I don't think I stood a chance of ever being anything but a scientist.

Finally, I am certain I would have never completed my Ph.D. without the love and support of my (now unfortunately ex-) girlfriend, Aleks Kuzminski. You believed in me when no one else did and never let me quit. Your faith in me never wavered. I will always treasure the years we had together.

A Search for Chargino-Neutralino Production at the Fermilab Tevatron Collider

by
Benn Tannenbaum

Doctor of Philosophy
Physics

December, 1997

A Search for Chargino-Neutralino Production at the Fermilab Tevatron Collider

by

Benn Tannenbaum

Bachelor of Arts, Physics, Grinnell College, 1990
Master of Science, Physics, Michigan State University, 1993
Doctor of Philosophy, Physics, University of New Mexico, 1997

ABSTRACT

We have searched for evidence of supersymmetry with the Collider Detector at Fermilab using trilepton events in $p\overline{p}$ collisions at $\sqrt{s} = 1.8$ TeV. In the Minimal Supersymmetric Standard Model (MSSM), we expect trilepton events from chargino-neutralino ($\tilde{\chi}_1^{\pm}\tilde{\chi}_2^0$) pair production, with subsequent decay into leptons. In all possible combinations of electron and muon channels, we observe no candidate events in 107 pb^{-1} of data. We present limits on chargino and neutralino production within the framework of a supergravity inspired MSSM: $\sigma_{\tilde{\chi}_1^{\pm}\tilde{\chi}_2^0}\cdot\mathrm{BR}(\tilde{\chi}_1^{\pm}\tilde{\chi}_2^0 \rightarrow 3\ell + X) < 0.34$ pb and $\mathrm{M}_{\tilde{\chi}_1^{\pm}} > 81.5$ GeV/c^2 for $\tan\beta = 2$, $\mu = -600$ GeV/c^2 and $\mathrm{M}_{\tilde{q}} = \mathrm{M}_{\tilde{g}}$. We also present limits on a SU(5)×U(1) supergravity model and a 4 and 1/2 parameter Minimal SUGRA model.

Table of Contents

Acknowledgements **iv**

List of Figures **x**

List of Tables **xiv**

Chapter 1. Introduction **1**

Chapter 2. Theory and Motivation **3**

2.1 Overview of Supersymmetry 5

2.1.1 The Minimal Supersymmetric Model 5

2.1.2 Reducing the parameter space 6

2.1.3 Benefits of SUSY 23

2.2 Supersymmetric particle spectrum 24

2.3 Supersymmetric discovery channels 26

2.4 Background 28

2.5 Naturalness 29

Chapter 3. Apparatus **33**

3.1 The Tevatron 33

3.2 The Collider Detector at Fermilab 35

3.2.1 Calorimeters 37

3.2.2 Central Muon Chambers 40

3.2.3 Central Tracking Chamber 40

3.2.4 Vertex Detector 42

3.2.5 Additional Detector Components 42

3.2.6 Trigger 43

3.2.7 QFL: The CDF Detector Simulation package 44

Chapter 4. Data Analysis **46**

4.1 Bank Creation 46

4.1.1 ELES banks 46

4.1.2 CMUO banks 47

4.1.3 CMIO banks . . . 47
4.1.4 TRKS banks . . . 47
4.1.5 VTVZ banks . . . 48
4.1.6 METS banks . . . 48
4.2 Event selection . . . 48
4.2.1 Dilepton Selection (Skimming) . . . 49
4.2.2 Trilepton Selection (Skimming) . . . 59
4.2.3 Trilepton Selection (Analysis) . . . 59
4.3 Bad Run Removal . . . 70
4.4 Cosmic Ray Removal . . . 70
4.4.1 CMCOS . . . 70
4.4.2 Angle plus timing . . . 71
4.5 Vertex Requirements . . . 76
4.6 Background Removal . . . 77
4.6.1 Real trilepton events . . . 78
4.6.2 Dilepton plus misidentified lepton events . . . 81
4.6.3 Missing Transverse Energy Measurement . . . 83
4.6.4 Estimate of Expected Background . . . 87

Chapter 5. Limits on the SiMSSM parameter space **89**
5.1 Monte Carlo Simulation techniques . . . 89
5.1.1 Trigger Simulation . . . 90
5.2 Limit setting method . . . 91
5.2.1 N_{exp}: Systematic Uncertainty . . . 92
5.2.2 ϵ^{tot}: Detection Efficiency . . . 93
5.2.3 $\int \mathcal{L}dt$: Integrated Luminosity . . . 98
5.3 Limits on the SiMSSM . . . 98
5.4 Limits on other models . . . 113
5.4.1 SU(5)×U(1) Supergravity model . . . 113
5.4.2 SUGRA . . . 120

Chapter 6. Conclusion **129**

Bibliography **134**

List of Figures

2.1 The extrapolation of the Standard Model gauge couplings to very high energies. . . . 4
2.2 Chargino mass as a function of μ and the gluino mass. 9
2.3 Chargino mass as a function of μ and $\tan\beta$. 10
2.4 Chargino mass as a function of $\tan\beta$ and gluino mass. 11
2.5 LSP mass as a function of μ and gluino mass. 12
2.6 LSP mass as a function of μ and $\tan\beta$. 13
2.7 LSP mass as a function of $\tan\beta$ and gluino mass. 14
2.8 Neutralino mass as a function of μ and gluino mass. 15
2.9 Neutralino mass as a function of μ and $\tan\beta$. 16
2.10 Neutralino mass as a function of $\tan\beta$ and gluino mass. 17
2.11 Neutralino Higgsino fraction as a function of μ and $\tan\beta$. 18
2.12 Neutralino Higgsino fraction as a function of μ and $\tan\beta$. 19
2.13 Neutralino Higgsino fraction as a function of μ and gluino mass. 20
2.14 Neutralino Higgsino fraction as a function of μ and gluino mass. 21
2.15 Neutralino Higgsino fraction as a function of μ and gluino mass. 22
2.16 The extrapolation of the Standard Model gauge couplings to very high energies within the framework of SUSY. 24
2.17 Feynman diagrams for fermionic and bosonic contributions to the Higgs' self-energy. 25
2.18 Associated $\tilde{\chi}_1^{\pm}\tilde{\chi}_2^0$ production at the Tevatron. 28
2.19 Three body decay modes for charginos and neutralinos. 29
2.20 Two body decay modes for charginos and neutralinos. 30
2.21 Naturalness of the lightest chargino. 31
2.22 The naturalness of a variety of different sparticles. 32

3.1 Overview of the accelerator complex at Fermilab. 34
3.2 A perspective view of CDF. 36
3.3 A one quarter view of CDF. 37
3.4 The $\eta - \phi$ segmentation of the calorimeters in the CDF detector. 39
3.5 The $\eta - \phi$ muon coverage for the central region of the CDF detector. 41

4.1 Distributions for CEM electrons which pass the tight ID cuts. 53
4.2 Distributions for CEM electrons which pass the tight ID cuts. 54

4.3 Distributions for CEM electrons which pass the loose ID cuts. 55
4.4 Distributions for CEM electrons which pass the loose ID cuts. 56
4.5 Distributions for PEM electrons which pass the loose ID cuts. 57
4.6 Two body mass for opposite sign electron pairs. 58
4.7 Distributions for CMU/P muons which pass the tight ID cuts. 60
4.8 Distributions for CMU/P muons which pass the tight ID cuts. 61
4.9 Distributions for CMU/P muons which pass the loose ID cuts. 62
4.10 Distributions for CMU/P muons which pass the loose ID cuts. 63
4.11 Distributions for CMX muons which pass the loose ID cuts. 64
4.12 Distributions for CMX muons which pass the loose ID cuts. 65
4.13 Distributions for CMIO muons which pass the loose ID cuts. 66
4.14 Two body mass for opposite sign muon pairs. 67
4.15 Two body mass for opposite sign muon pairs in the J/ψ region. 68
4.16 Cosmic ray filter status bit for candidate CMU/P and CMX muons. 72
4.17 Event display for a typical cosmic ray. 73
4.18 Maximum and middle opening angles for the three possible lepton pair combinations for a sample Monte Carlo point. 74
4.19 Maximum and middle opening angles for the three possible lepton pair combinations for $Z^0 \rightarrow \mu\mu$ events with a third μ (data). 75
4.20 Maximum and middle opening angles for the three possible lepton pair combinations for the trilepton data set. 75
4.21 The difference in time for muon pairs. 76
4.22 The difference in timing for $Z^0 \rightarrow \mu\mu$ events (from data) with a third muon in the event. 77
4.23 Isolation for leptons from b quark decays. 79
4.24 Opening angle for lepton pairs from b quark decays. 80
4.25 Two-body masses for diboson background events. 82
4.26 Opening angle for background due to Drell-Yan processes. 84
4.27 Dilepton mass for background due to Drell-Yan processes. 85
4.28 Missing transverse energy for each of the types of background. 86

5.1 The detection efficiency as a function of $\mathrm{M}(\tilde{\chi}_1^{\pm})$. 94
5.2 The detection efficiency as a function of $\mathrm{M}(\tilde{\chi}_1^{\pm})$ for a variety of points in SiMSSM space. 95
5.3 The detection efficiency as a function of $\mathrm{M}(\tilde{\chi}_1^{\pm})$ comparing individual SiMSSM points to an overall fit. 96

5.4 The detection efficiency as a function of $M(\tilde{\chi}_1^{\pm})$ for a variety of points in SiMSSM space, constraining $\tan\beta = 2$. 97

5.5 Production cross section times branching ratio to leptons for $\tilde{\chi}_1^{\pm}\tilde{\chi}_2^0$ production as a function of $\tilde{\chi}_1^{\pm}$ mass for $\tan\beta = 2$, and $\mu = -400$ GeV/c^2. 101

5.6 Production cross section times branching ratio to leptons for $\tilde{\chi}_1^{\pm}\tilde{\chi}_2^0$ production as a function of $\tilde{\chi}_1^{\pm}$ mass for light squarks. 102

5.7 Lower limit on $M(\tilde{\chi}_1^{\pm})$ as a function of $M(\tilde{q})/M(\tilde{g})$. 103

5.8 Production cross section times branching ratio to leptons for $\tilde{\chi}_1^{\pm}\tilde{\chi}_2^0$ production as a function of $\tilde{\chi}_1^{\pm}$ mass for $\tan\beta = 2$, and $M(\tilde{q}) = M(\tilde{g})$ 104

5.9 Lower limit of $M(\tilde{\chi}_1^{\pm})$ as a function of μ. 105

5.10 Production cross section times branching ratio to leptons for $\tilde{\chi}_1^{\pm}\tilde{\chi}_2^0$ production as a function of $\tilde{\chi}_1^{\pm}$ mass for $\tan\beta = 1.1$, $M(\tilde{q}) = M(\tilde{g})$ and $\mu = -400$ GeV/c^2. 106

5.11 Production cross section times branching ratio to leptons for $\tilde{\chi}_1^{\pm}\tilde{\chi}_2^0$ production as a function of $\tilde{\chi}_1^{\pm}$ mass for $\tan\beta = 1.5$, $M(\tilde{q}) = M(\tilde{g})$ and $\mu = -400$ GeV/c^2. 107

5.12 Production cross section times branching ratio to leptons for $\tilde{\chi}_1^{\pm}\tilde{\chi}_2^0$ production as a function of $\tilde{\chi}_1^{\pm}$ mass for $\tan\beta = 2$, $M(\tilde{q}) = M(\tilde{g})$ and $\mu = -400$ GeV/c^2. 108

5.13 Production cross section times branching ratio to leptons for $\tilde{\chi}_1^{\pm}\tilde{\chi}_2^0$ production as a function of $\tilde{\chi}_1^{\pm}$ mass for $\tan\beta = 4$, $M(\tilde{q}) = M(\tilde{g})$ and $\mu = -400$ GeV/c^2. 109

5.14 Production cross section times branching ratio to leptons for $\tilde{\chi}_1^{\pm}\tilde{\chi}_2^0$ production as a function of $\tilde{\chi}_1^{\pm}$ mass for $\tan\beta = 8$, $M(\tilde{q}) = M(\tilde{g})$ and $\mu = -400$ GeV/c^2. 110

5.15 Lower limit on $M(\tilde{\chi}_1^{\pm})$ as a function of $\tan\beta$. 111

5.16 Production cross section times branching ratio to leptons for $\tilde{\chi}_1^{\pm}\tilde{\chi}_2^0$ production as a function of $\tilde{\chi}_1^{\pm}$ mass for $\tan\beta = 2$ and $\mu = -400$ GeV/c^{2}and $M(\tilde{q}) = 500$ GeV/c^2. . . 112

5.17 The acceptance for all four trilepton modes for SU(5) $\times$ U(1) model production of trileptons. 118

5.18 $\sigma \cdot BR$ versus $\tilde{\chi}_1^{\pm}$ mass for SU(5) $\times$ U(1) model production of trileptons. 119

5.19 Detection efficiency using the SUGRA model. 122

5.20 Production cross section times branching ratio to leptons for $\tilde{\chi}_1^{\pm}\tilde{\chi}_2^0$ production as a function of $\tilde{\chi}_1^{\pm}$ mass for SUGRA. 123

6.1 The naturalness of a variety of different sparticles. 130
6.2 Production cross section for a variety of processes at the upgraded Tevatron. 132

List of Tables

1.1 The fermionic particles of the Standard Model. 2
1.2 The bosonic particles of the Standard Model. 2

2.1 Standard Model and SUSY particle spectrum. 27

3.1 Summary of the properties of the various CDF calorimeter systems. 38
3.2 Summary of efficiencies for lepton IDs. 45

4.1 Skimming selection criteria for CEM and PEM electrons. 50
4.2 Skimming selection criteria for CMU/P, CMX and CMIO muons. 50
4.3 Number of CEM and PEM electrons left after each lepton identification cut. 52
4.4 Number of CMU/P, CMX and CMIO muons left after each lepton identification cut. 59
4.5 Analysis lepton selection cuts for CEM and PEM electrons. 65
4.6 Analysis lepton selection cuts for CMU/P, CMX and CMIO muons. 69
4.7 Number of CEM and PEM electrons left after each analysis lepton identification cut. 69
4.8 Number of CMU/P, CMX and CMIO muons left after each analysis lepton identification cut. 74
4.9 Expected background after each cut. 87
4.10 Number of data, expected background and signal Monte Carlo after each cut. 88

5.1 The Level 2 triggers used in this analysis. 91
5.2 Input and output parameters for the SiMSSM points scanned. 113
5.3 Input and output parameters for the SiMSSM points scanned (cont.). 114
5.4 Input and output parameters for the SiMSSM points scanned (cont.). 115
5.5 Input and output parameters for the SiMSSM points scanned (cont.). 116
5.6 Input and output parameters for the SiMSSM points scanned (cont.). 117
5.7 The input and output parameters used to examine the SU(5) $\times$ U(1) model. 120

5.8 Masses of the $\tilde{\chi}_1^{\pm}$, $\tilde{\chi}_2^0$, $\tilde{\chi}_1^0$ for the points examined in the SU(5) $\times$ U(1) model. 120
5.9 Input and output parameters for the SUGRA points scanned. 124
5.10 Input and output parameters for the SUGRA points scanned. 125
5.11 Output parameters for the SUGRA points scanned. 126
5.12 Output parameters for the SUGRA points scanned (cont.). 127
5.13 Output parameters for the SUGRA points scanned (cont.). 128

6.1 Limits on $\tilde{\chi}_1^{\pm}$ and $\tilde{\chi}_2^0$ masses in the SiMSSM framework. 131

6.2 Limits on $\tilde{\chi}_1^{\pm}$ and $\tilde{\chi}_2^0$ masses in the SU(5)×U(1) framework. 131

6.3 Limit on $\tilde{\chi}_1^{\pm}$ and $\tilde{\chi}_2^0$ masses in the Minimal SUGRA model. 131

6.4 Lower limits for several searches during Run II. 133

Chapter 1

Introduction

> **phys·ics** (fiz′iks) *n.* the science dealing with the properties, changes, interaction, etc. of matter and energy in which energy is considered to be continuous (**classical physics**), including electricity, heat, optics, mechanics, etc., and now also dealing with the atomic scale of nature in which energy is considered to be discrete (**quantum physics**), including such branches as atomic, nuclear, and solid-state physics [1]

Particle, or high energy, physics, is the study of quarks and leptons and their interactions. Just as cells compose living organisms, atoms compose molecules and protons, neutrons and electrons compose atoms, the various quarks compose neutrons and protons. The theory describing the quarks and leptons is known as the Standard Model. Just as Mendeleev's periodic table organizes the elements into columns and rows according to composition, the Standard Model groups the quarks and leptons into families by charge and mass. Tables 1.1 and 1.2 list the known particles. In addition to the quarks and leptons, there are particles which mediate the four known forces: the photon (γ) mediates the electromagnetic force, the $W^{\pm}$ and Z^0 mediate the the weak force, the gluon (g) mediates the strong force and the graviton mediates gravity[1].

The Standard Model is the combination of two other theories, the electroweak theory of Weinberg, Salam and Glashow (WSG) , and Quantum Chromodynamics (QCD). QED, the part of the electroweak theory that describes the interactions of electrons, muons and taus with photons, is one of the most successful theories in all of science. The remainder of the WSG theory describes the charged and neutral weak interactions. QCD describes the interaction of quarks via the strong force.

[1]The graviton is a postulated particle which has not yet been seen. Since gravity is significantly weaker than the other three forces, its mediator is much more difficult to detect.

Table 1.1: The fermionic particles of the Standard Model. The quarks in the top row have charge $+\frac{2}{3}$ times the electron charge, while the quarks in the second row have charge -$\frac{1}{3}$ times the electron charge. All of the leptons in the third row have charge -1 and all of the neutrinos are neutral. The quarks can interact via any of the four forces, the leptons via all but the strong force, and the neutrinos can interact via the weak and gravitational forces. All particles have been observed experimentally except the ν_τ.

quarks	up	u	charm	c	top	t
	down	d	strange	s	bottom	b
leptons	electron	e	muon	μ	tau	τ
	electron neutrino	ν_e	muon neutrino	ν_μ	tau neutrino	ν_τ

Table 1.2: The bosonic particles of the Standard Model. All bosons have been observed except the graviton (G).

Boson	Force Mediated
photon (γ)	Electromagnetic
$W^\pm$	Charged Weak
Z^0	Neutral Weak
gluon (g)	Strong
graviton (G)	Gravity

Overall, the Standard Model has been very successful. However, it leaves many questions unanswered. Many theories have been proposed to answer these questions. This dissertation is a search for evidence of physics beyond the Standard Model. Chapter 2 describes the theory examined, Chapter 3 the apparatus used, Chapter 4 the analysis techniques and Chapter 5 the limits reached. Chapter 6 draws some conclusions.

Chapter 2

Theory and Motivation

The Standard Model has proven to be a very effective low energy[1] theory– a theory that is accurate in the currently accessible energy spectrum. Its two major components, Quantum Chromodynamics (QCD) [2] and the electroweak theory of Weinberg, Salam and Glashow [3], predict the interaction of quarks, leptons and the gauge bosons well. The theory is so successful that the existence of the top quark was accepted long before its discovery. The production cross sections (σ) and decay branching ratios for the various interactions are accurately predicted. In fact, there is very little experimental evidence for any physics beyond the Standard Model.

There are, however, many unanswered questions about the Standard Model and the universe in which we live. Many of these questions deal with mass. For example,

- Depending on the parameterization used, either the masses of all of the quarks and leptons or the couplings of the leptons and quarks to the vacuum expectation value of the Higgs boson are free. Why? Why does the Standard Model not predict the masses of the particles? Why are there three generations?

- The mass of the top quark is 176 GeV/c^2 [4]. The mass of the other quark in its isospin doublet, the bottom quark, is $\simeq$ 4.5 GeV/c^2. The ratio of the top to bottom mass is almost 40! The ratio of charm to strange mass is $\simeq$ 7.5 and the ratio of up to down mass is $\simeq$ 0.5 [5]. Why is the top quark so massive, and why is it so much more massive than its isospin partner?

- The mediator of the electromagnetic force, the photon, and the mediator of the strong force, the gluon, are both massless. Why are the mediators of the weak force, the $W^{\pm}$ and the Z^0,

[1] "Low energy", of course, depends on the beholder. For this dissertation low energy implies energies of the TeV (10^{12} eV) scale or less.

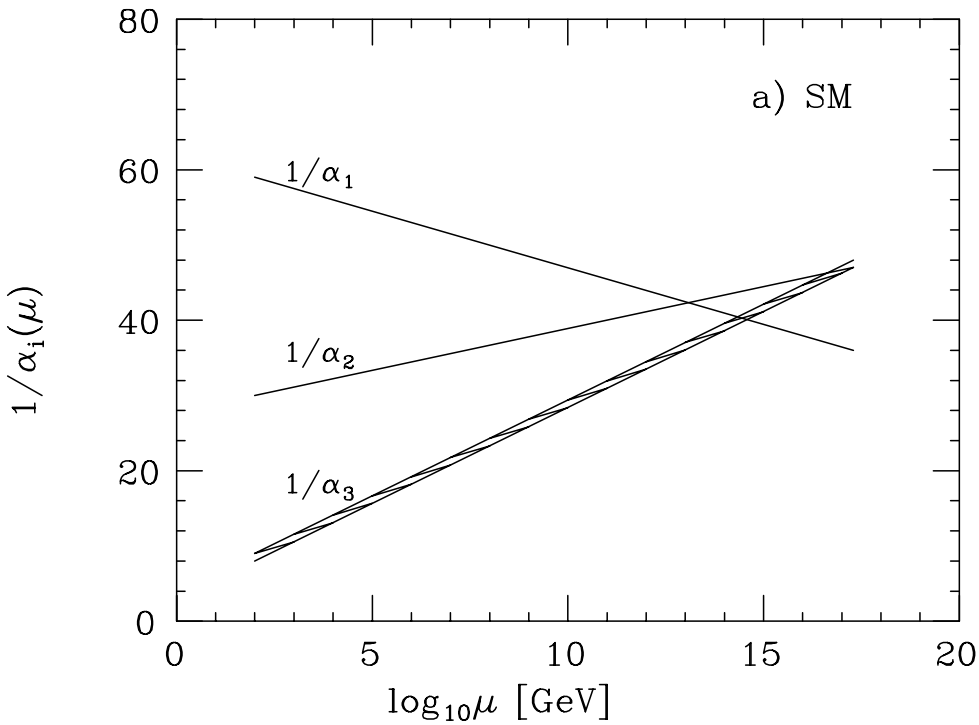

Figure 2.1: The extrapolation of the Standard Model gauge couplings to very high energies. α_1 is the $\mathrm{SU(1)}_{\mathrm{hypercharge}}$ coupling constant, α_2 is the $\mathrm{SU(2)}_{\mathrm{weak}}$ coupling constant and α_3 is the $\mathrm{SU(3)}_{\mathrm{strong}}$ coupling constant. Adapted from [6].

massive? Why are they so massive? What sets the scale for electroweak symmetry breaking?

- The Standard Model does not need to include the Higgs boson. The Higgs mechanism is inserted *ad hoc* to provide a mechanism for electroweak symmetry breaking and further gives masses to the quarks and leptons. It is a mechanism that works, but it may not be the right one.

- Early physics research led to the realization that electricity and magnetism are different aspects of the same force. The prediction and subsequent discovery of the $W^{\pm}$ and Z^0 led to the realization that, above certain energies, the electromagnetic and weak forces are different aspects of the same force. However, the SM-based extrapolation of precise measurements at LEP clearly show (Figure 2.1) that the strong, electromagnetic and weak forces do not unify at any energy. They do approach a common value, but do not meet at a point. We currently believe that there must exist a theory of everything in which all the forces unify: a Grand Unified Theory (GUT). This is not possible within the framework of the SM.

- Grand Unified Theories require a scalar particle to provide the mechanism for breaking the

symmetry at the Grand Unified scale. However, its mass (on the order of the GUT scale: 10^{16} GeV/c^2) must be specified to great accuracy to provide for the physics at the weak scale. This is known as the fine tuning or hierarchy problem.

- Current measurements of the rate of rotation of some distant galaxies do not match with the visible mass. This appears to imply that there must be some additional, unseen, mass that allows these galaxies to rotate as quickly as they do.

All of these facts lead us to believe that there must be a theory beyond the Standard Model. Many have been proposed, such as quark compositness (or technicolor), left-right symmetric models and SUperSYmmetry (SUSY). Each of these models solves some or all of the above problems and each has their own set of strengths and weaknesses. A weakness common to all of them is a total lack of experimental evidence for any of them. At present SUSY is a very popular theory and is generating interest in both the theoretical and experimental communities.

In the remainder of this Chapter, I will briefly describe the basic principles of SUSY and why SUSY is of interest, describe the particle spectrum, discuss signals and backgrounds germane to this analysis, and discuss naturalness.

2.1 Overview of Supersymmetry

The theory behind SUSY is complex and a complete introduction is beyond the scope of this dissertation. A quick search of the SPIRES data base [7] lists over 7,000 papers on the topic of SUSY. A good starting point for further reading can be found in Refs. [8, 9, 10] and the references within. However, an introduction is appropriate, especially as there are few references that are comprehensible to the experimentalist at first reading: the transition from the SUSY Lagrangian to the constrained model we use is difficult.

2.1.1 The Minimal Supersymmetric Model

In the SM, each particle is described by several quantum numbers: spin, charge, mass, isospin, etc. All quarks and leptons are fermions, meaning they have half-integral spin. The mediators of the various forces are all bosons and thus have integral spin. SUSY supposes that for each particle with an integral spin, there exists a particle with the same charge, isospin, etc., but with half-integral spin. Likewise, for each half-integral spin particle there exists an integral spin partner. The names of these new particles are related to the names of the original particles: the scalar partners to the fermions are the *s*fermions (such as *s*leptons and *s*quarks) and the partners to the gauge bosons gain an -*ino* (such as Higgs*ino*). The Minimal Supersymmetric Model (MSSM) gives each particle a superpartner and requires two Higgs doublets and their superpartners. This more than doubles the

particle spectrum and greatly increases the number of free parameters to over 100. A few reasonable assumptions (described in the following sections) reduce the number of free parameters to six[2].

The second Higgs doublet is necessary to cancel anomalies [8]. The second doublet also allows one to use one doublet to give masses to the up-type quarks and the neutrinos, and the other doublet to give masses to the down-type quarks and the charged leptons.

2.1.2 Reducing the parameter space

The MSSM in its purest form has over 100 free parameters. One of my complaints about the SM was that it had too many free parameters. By adding SUSY I seem to have made the problem worse! To reduce the number of free parameters we can make certain model assumptions that are either based on observed or desired physics. The resulting model is unfortunately also sometimes known as the MSSM. I shall refer to it as the SiMSSM (Supergravity-inspired MSSM).

Grand Unified Theories (GUTs)

If we require unification of the coupling constants at the GUT scale ("the GUT hypothesis" provided by supergravity [11]), we are led to the following relationships:

$$\left.\begin{aligned} M_{\widetilde{W}} &= \frac{\alpha_2}{\alpha_3} M_{\tilde{g}} \\ M_{\widetilde{B}} &= \frac{5\alpha_1}{3\alpha_2} M_{\widetilde{W}} \end{aligned}\right\} \tag{2.1}$$

where $\widetilde{W}$ and $\widetilde{B}$ are the weak eigenstates of the SUSY partners to the SM electroweak gauge bosons and the α_i are the hypercharge, weak isospin, and strong coupling constants at the appropriate scale, respectively. At the Tevatron scale ($\sqrt{s} = 1.8$ TeV) $\alpha_1 = 0.00781$, $\alpha_2 = 0.03397$ and $\alpha_3 = 0.120$ [5]. The 5/3 arises from the use of SU(5) as the unifying group. SU(5) is the smallest group that can unify U(1)×SU(@)×SU(3) [12]. Equation 2.1 causes $M_{\widetilde{W}}$ and $M_{\widetilde{B}}$ to be functions of only $M_{\tilde{g}}$, since the α_i are well measured quantities.

Renormalization Group Equations

We relate the slepton ($\widetilde{\ell}$) and sneutrino ($\widetilde{\nu}$) masses to the squark ($\tilde{q}$) and gluino ($\tilde{g}$) masses through the Renormalization Group Equations as inspired by supergravity models [13]. These relations are made at the GUT scale and must be rescaled (or renormalized) to the TeV scale where we currently

[2]See *e.g.* Ref. [10] for more details.

work:

$$\left.\begin{array}{rcl} M^2_{\tilde{\ell}_L} & = & M^2_{\tilde{q}} - 0.73 M^2_{\tilde{g}} - 0.27 M^2_Z \cos 2\beta \\ M^2_{\tilde{\ell}_R} & = & M^2_{\tilde{q}} - 0.78 M^2_{\tilde{g}} - 0.23 M^2_Z \cos 2\beta \\ M^2_{\tilde{\nu}_L} & = & M^2_{\tilde{q}} - 0.73 M^2_{\tilde{g}} + 0.5 M^2_Z \cos 2\beta \end{array}\right\} \tag{2.2}$$

We assume the masses of all generations of each type of slepton ($\widetilde{\ell}_L$, $\widetilde{\ell}_R$ and $\widetilde{\nu}_L$) to be degenerate. These relations are calculated by averaging similar equations which do not assume degenerate generations [14]. This is acceptable since this analysis is largely affected by the masses of only the first generation squarks. The masses of the $\widetilde{\ell}$s depend mainly on the difference in mass of the $\tilde{q}$s and $\tilde{g}$s.

R-parity and the Lightest Supersymmetric Partner

The MSSM allows the imposition of a global symmetry, so we assign each particle and superparticle a new multiplicative quantum number, $R \equiv (-)^{B+L+2S}$ where B is the baryon number, L is the lepton number and S is the spin of the particle. Thus, SM particles have $R = +1$ and SUSY particles have $R = -1$. If we require R-parity to be conserved, we then require the creation of SUSY particles in pairs. By requiring SUSY particles to be created in pairs, we must then have a lightest sparticle (LSP) that is stable. An electrically or color charged LSP causes many problems [15] so the LSP is generally assumed to be the lightest neutralino ($\tilde{\chi}^0_1$). Experimentally, the LSP can be thought of as a heavy neutrino: it will manifest itself as missing energy. The LSP is also an excellent candidate for cold dark matter [16].

Remaining free parameters

To continue reducing the number of free parameters, we further assume that the first and second generation squarks are degenerate in mass. This is an acceptable assumption, as this analysis is mainly affected by the masses of the first generation squarks. After making all the above assumptions, we are left with only a handful of free parameters: $\tan\beta$, μ, $\mathrm{M}_{\tilde{g}}$, $\mathrm{M}_{\tilde{q}}$, A_T, and M_{H_A}. $\tan\beta$ is the ratio of the vacuum expectation values for the two Higgs doublets:

$$\tan\beta = (\langle H_2\rangle / \langle H_1\rangle) \tag{2.3}$$

$$v^2 = \langle H_1\rangle^2 + \langle H_2\rangle^2 \tag{2.4}$$

where $v = 246$ GeV is fixed by the $W^\pm$ mass. $\tan\beta$ serves mainly to control the Higgsino vs gaugino content of the charginos ($\tilde{\chi}^\pm_i$) and neutralinos ($\tilde{\chi}^0_i$) (see Section 2.2 for explanations of these particles). μ is the un-mixed Higgsino mass (sometimes referred to as the supersymmetry-conserving Higgs mass parameter) and sets the scale for SUSY. It also has an effect on the Higgsino vs gaugino content of the charginos and neutralinos. $\mathrm{M}_{\tilde{g}}$ is the gluino mass and $\mathrm{M}_{\tilde{q}}$ is the common

squark mass. A_T is the Higgs-squark-squark trilinear interaction for the top squark, and M_{H_A} is the mass of the pseudoscalar Higgs boson.

This analysis, which is a search for $\tilde{\chi}_1^{\pm}\tilde{\chi}_2^0$ production, is obviously concerned with their masses and couplings. As will be seen below, once we know the masses and couplings of $\tilde{\chi}_1^{\pm}$, $\tilde{\chi}_1^0$, $\tilde{\chi}_2^0$ and sleptons (and to some degree, the squarks), we can begin to set limits on the production of SUSY particles.

In the regime where $M_{Z^0} \ll |M_i \pm \mu|$ the masses of $\tilde{\chi}_1^{\pm}$, $\tilde{\chi}_1^0$ and $\tilde{\chi}_2^0$ are functions solely of μ, $\tan\beta$ and the mass of the gluino [17]:

$$m_{\chi_1^{\pm}} = M_{\widetilde{W}} - \frac{M_W^2\left(M_{\widetilde{W}} + \mu\sin 2\beta\right)}{\mu^2 - M_{\widetilde{W}}^2} \tag{2.5}$$

$$\begin{aligned} m_{\chi_1^0} &= M_{\widetilde{B}} + \sin^2\theta_W \frac{m_Z^2(M_{\widetilde{B}} + \mu\sin 2\beta)}{(M_{\widetilde{B}}^2 - \mu^2)} \\ m_{\chi_2^0} &= M_{\widetilde{W}} + \cos^2\theta_W \frac{m_Z^2(M_{\widetilde{W}} + \mu\sin 2\beta)}{(M_{\widetilde{W}}^2 - \mu^2)} \end{aligned} \tag{2.6}$$

where $M_{\tilde{B}}$ and $M_{\widetilde{W}}$ are determined using Equation 2.1, θ_W ($\sin^2\theta_W = 0.234$) is the Weinberg mixing angle, M_W (= 80.33 GeV/c^2) is the $W^{\pm}$ mass and M_Z (= 91.187 GeV/c^2) is the Z^0 mass. The slepton masses are determined by Equations 2.2 and are functions of the squark and gluino masses and $\tan\beta$. Figures 2.2-2.10 show $M_{\tilde{\chi}_1^{\pm}}$, $M_{\tilde{\chi}_1^0}$ and $M_{\tilde{\chi}_2^0}$ as functions of $\tan\beta$, μ and $M_{\tilde{g}}$. Note that the masses of each particle is primarily a function of $M_{\tilde{g}}$, and not of either $\tan\beta$ or μ.

The Higgsino and gaugino content of the neutralinos can be determined using [17]:

$$\begin{pmatrix} \tilde{\chi}_1^0 \\ \tilde{\chi}_2^0 \\ \tilde{\chi}_3^0 \\ \tilde{\chi}_4^0 \end{pmatrix} = \begin{pmatrix} 1 & 0 & \frac{s_\theta(s_\beta+c_\beta)m_Z}{\sqrt{2}(\mu-M_{\widetilde{B}})} & \frac{s_\theta(s_\beta-c_\beta)m_Z}{\sqrt{2}(\mu+M_{\widetilde{B}})} \\ 0 & 1 & -\frac{c_\theta(s_\beta+c_\beta)m_Z}{\sqrt{2}(\mu-M_{\widetilde{W}})} & -\frac{c_\theta(s_\beta-c_\beta)m_Z}{\sqrt{2}(\mu+M_{\widetilde{W}})} \\ -\frac{s_\theta(s_\beta+c_\beta)m_Z}{\sqrt{2}(\mu-M_{\widetilde{B}})} & \frac{c_\theta(s_\beta+c_\beta)m_Z}{\sqrt{2}(\mu-M_{\widetilde{W}})} & 1 & 0 \\ -\frac{s_\theta(s_\beta-c_\beta)m_Z}{\sqrt{2}(\mu+M_{\widetilde{B}})} & \frac{c_\theta(s_\beta-c_\beta)m_Z}{\sqrt{2}(\mu+M_{\widetilde{W}})} & 0 & 1 \end{pmatrix} \begin{pmatrix} \widetilde{B} \\ \widetilde{W}_3 \\ \widetilde{H}_A \\ \widetilde{H}_S \end{pmatrix} \tag{2.7}$$

where s_x (c_x) is the sine (cosine) of the appropriate angle. It is immediately obvious that the $\tilde{\chi}_1^0$ is mainly $\tilde{B}$ with some Higgsino content and the $\tilde{\chi}_2^0$ is mainly $\tilde{W}_3$ with some Higgsino content. Figures 2.11-2.15 show the Higgsino fraction of $\tilde{\chi}_2^0$ as a function of $\tan\beta$, μ and $M_{\tilde{g}}$.

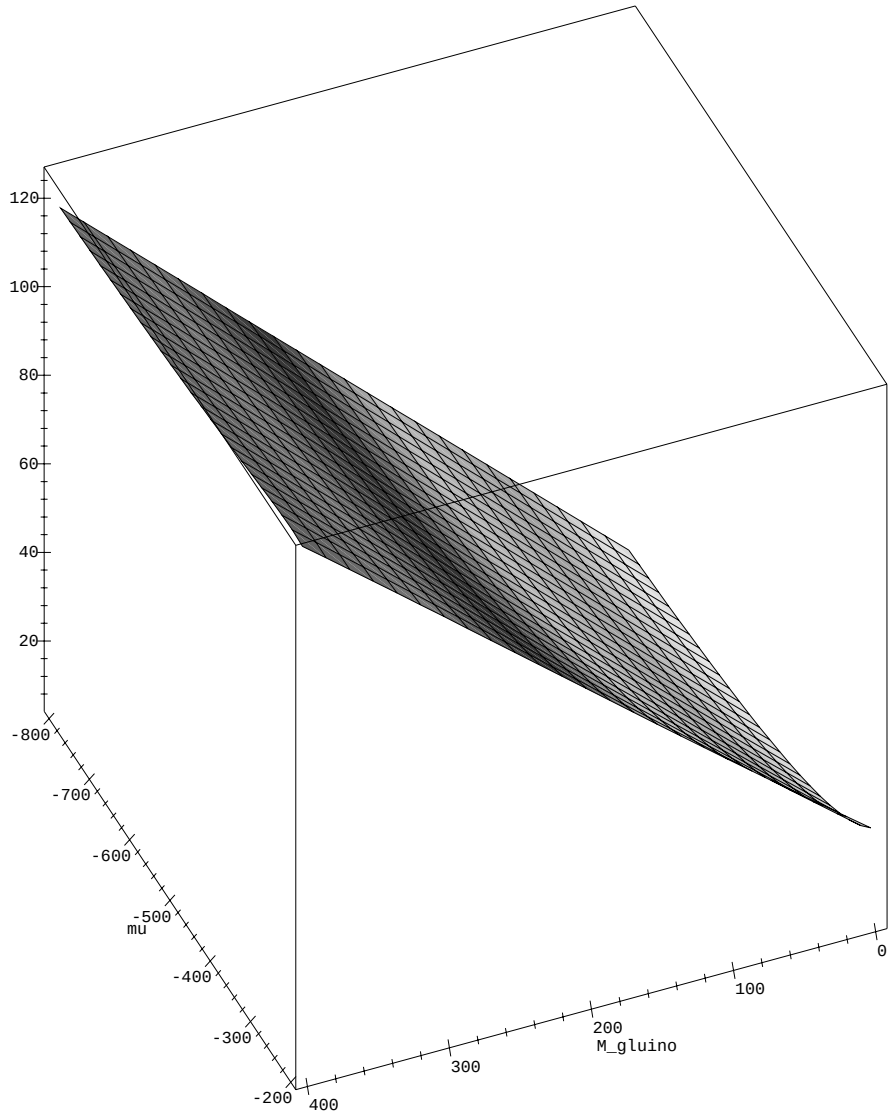

Figure 2.2: $M_{\tilde{\chi}_1^\pm}$ (vertical axis; in GeV/c^2) as a function of μ (left axis; in GeV/c^2) and $M_{\tilde{g}}$ (right axis; in GeV/c^2) for $\tan\beta = 2$. Note that the $\tilde{\chi}_1^\pm$ mass has little μ dependence. The shading in this and the following figures is an artifact of the program used to generate the plots.

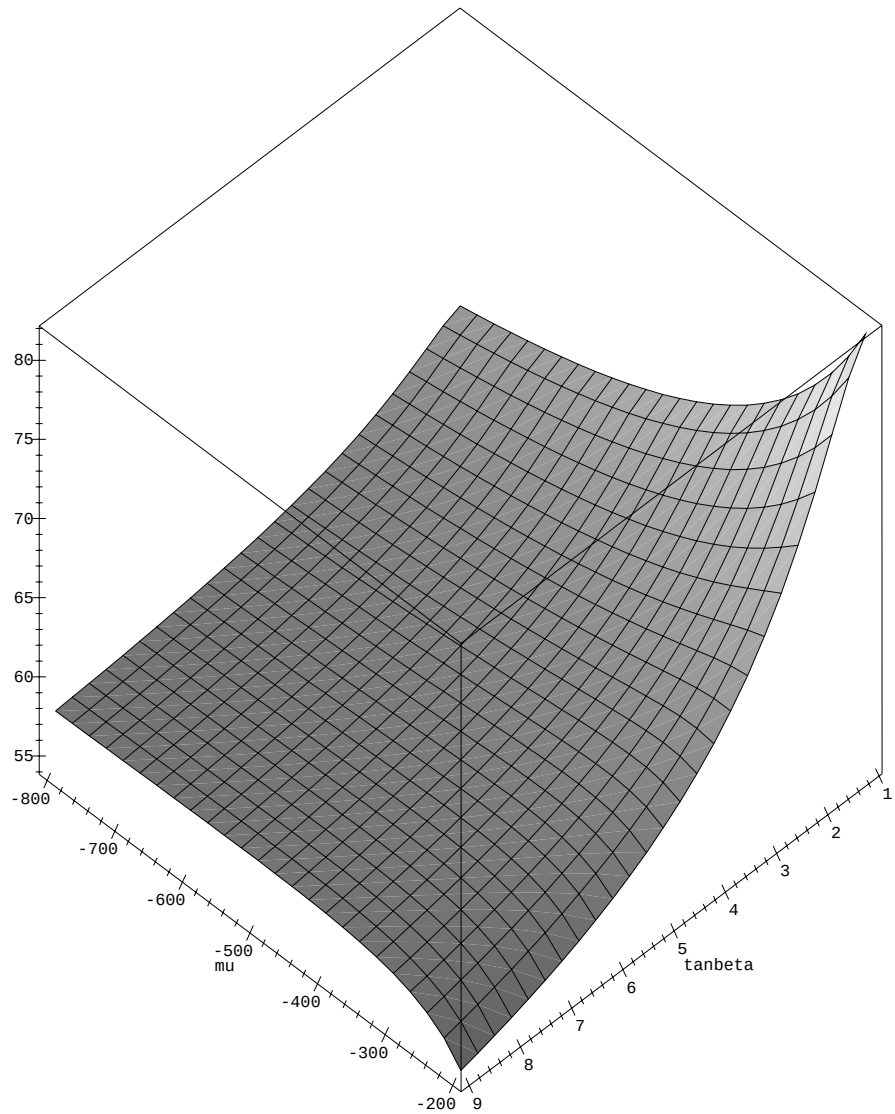

Figure 2.3: $M_{\tilde{\chi}_1^\pm}$ (vertical axis; in GeV/c^2) as a function of μ (left axis; in GeV/c^2) and $\tan\beta$ (right axis) for $M_{\tilde{g}} = 200$ GeV/c^2. Note that the vertical axis has a range of only 15 GeV/c^2; the $\tilde{\chi}_1^\pm$ mass has much smaller dependence on μ and $\tan\beta$ than on $M_{\tilde{g}}$.

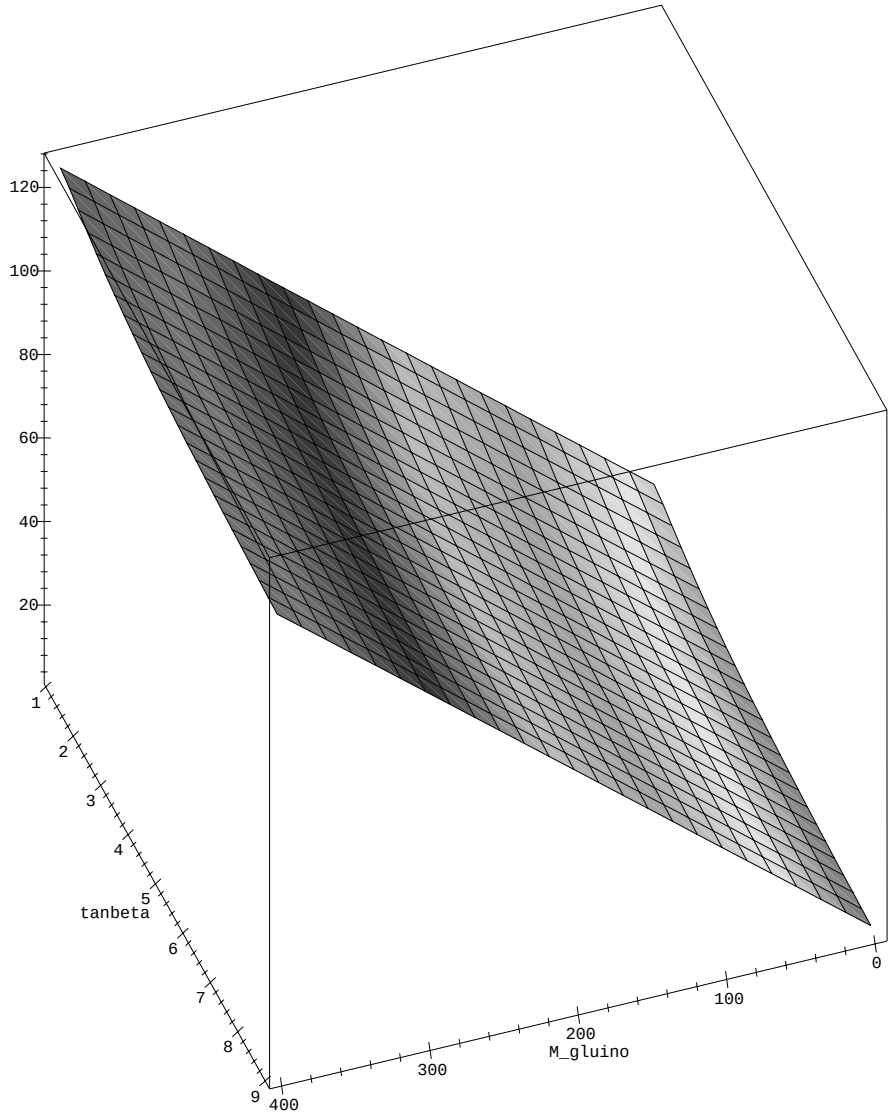

Figure 2.4: $M_{\tilde{\chi}_1^\pm}$ (vertical axis; in GeV/c^2) as a function of $\tan\beta$ (left axis) and $M_{\tilde{g}}$ (right axis; in GeV/c^2) for $\mu = -400$ GeV/c^2. Note that the mass has little $\tan\beta$ dependence.

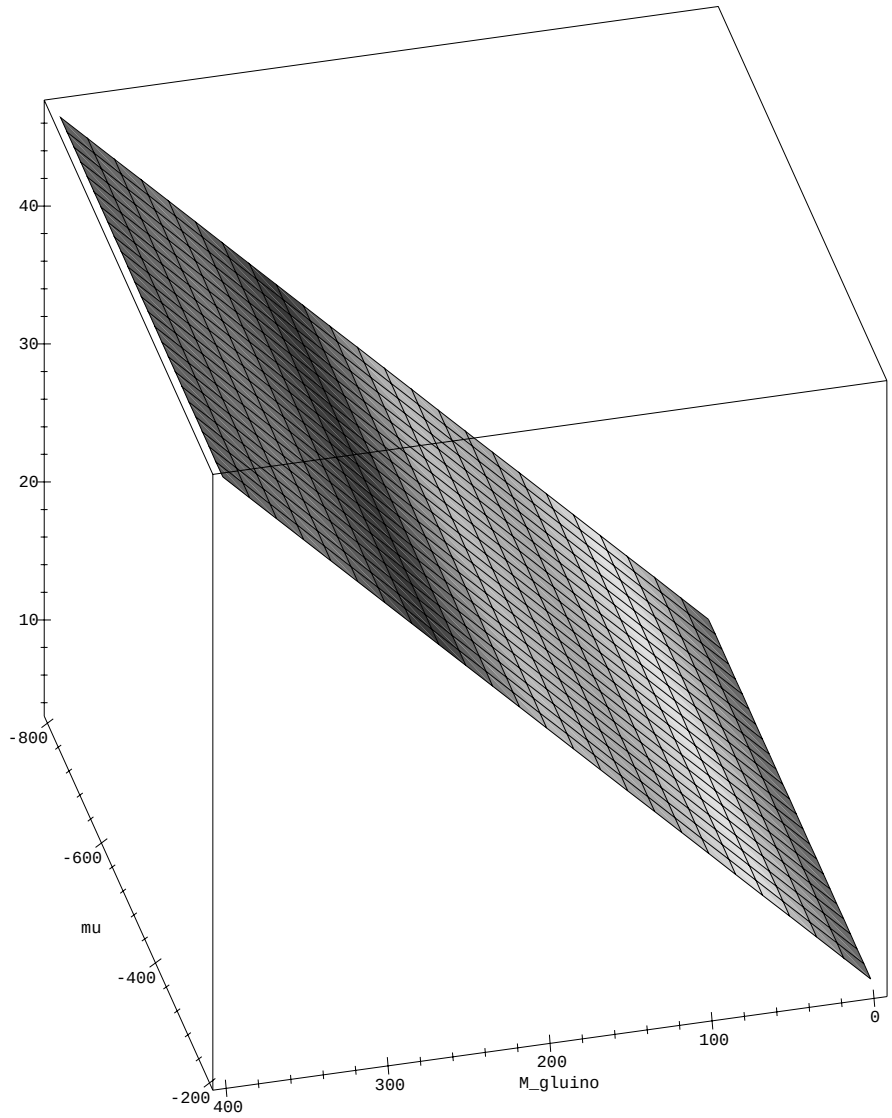

Figure 2.5: $M_{\tilde{\chi}_1^0}$ (vertical axis; in GeV/c^2) as a function of μ (left axis; in GeV/c^2) and $M_{\tilde{g}}$ (right axis; in GeV/c^2) for $\tan\beta = 2$. Note that the mass is largely independent of μ.

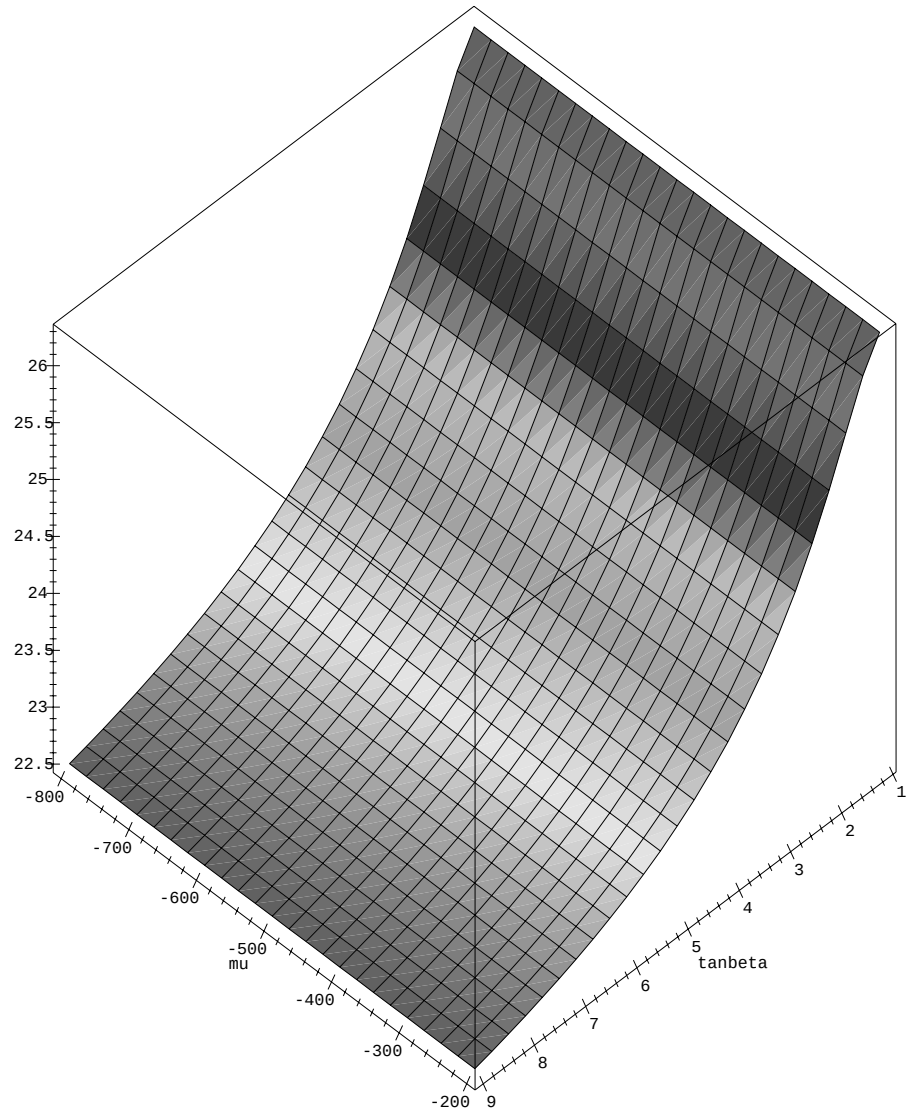

Figure 2.6: $M_{\tilde{\chi}_1^0}$ (vertical axis; in GeV/c^2) as a function of μ (left axis; in GeV/c^2) and $\tan\beta$ (right axis) for $M_{\tilde{g}} = 200$ GeV/c^2. Note that the mass is independent of μ and only weakly depends on $\tan\beta$ (the vertical scale only spans 4 GeV/c^2).

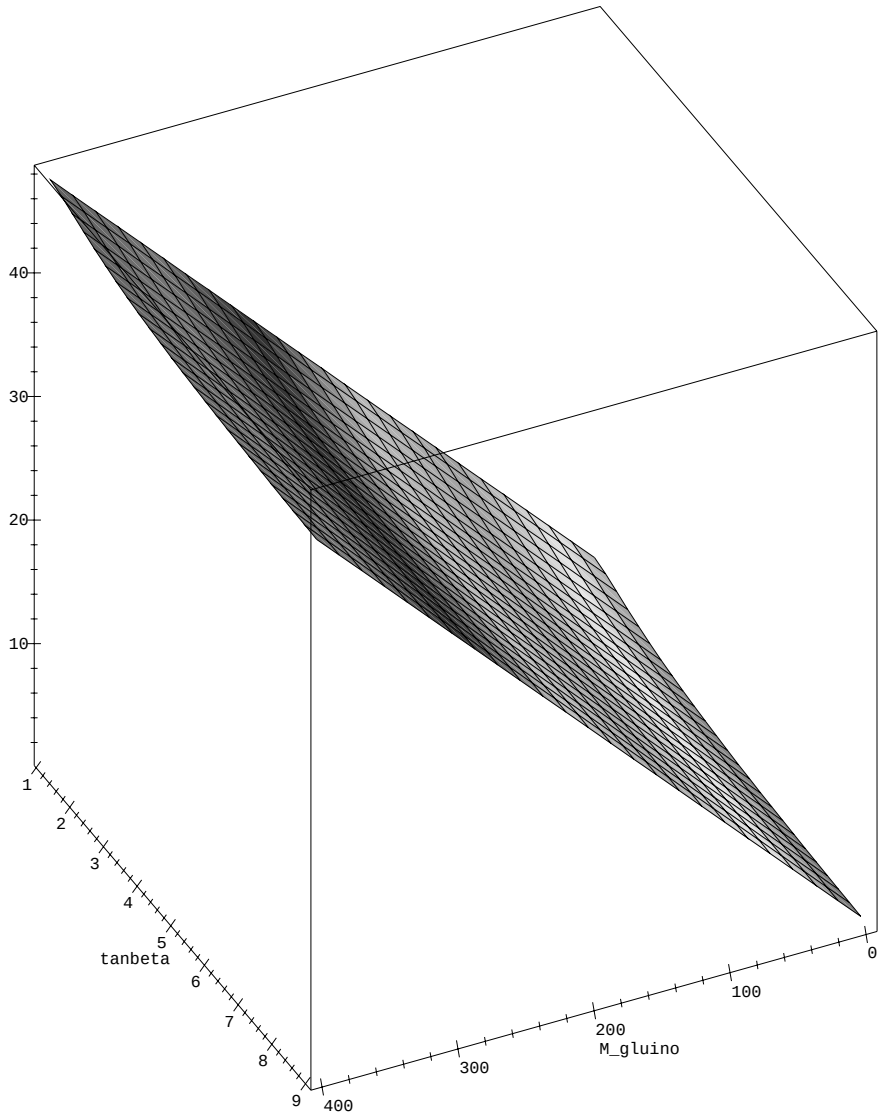

Figure 2.7: $M_{\tilde{\chi}_1^0}$ (vertical axis; in GeV/c^2) as a function of $\tan\beta$ (left axis) and $M_{\tilde{g}}$ (right axis; in GeV/c^2) for $\mu = -400$ GeV/c^2.

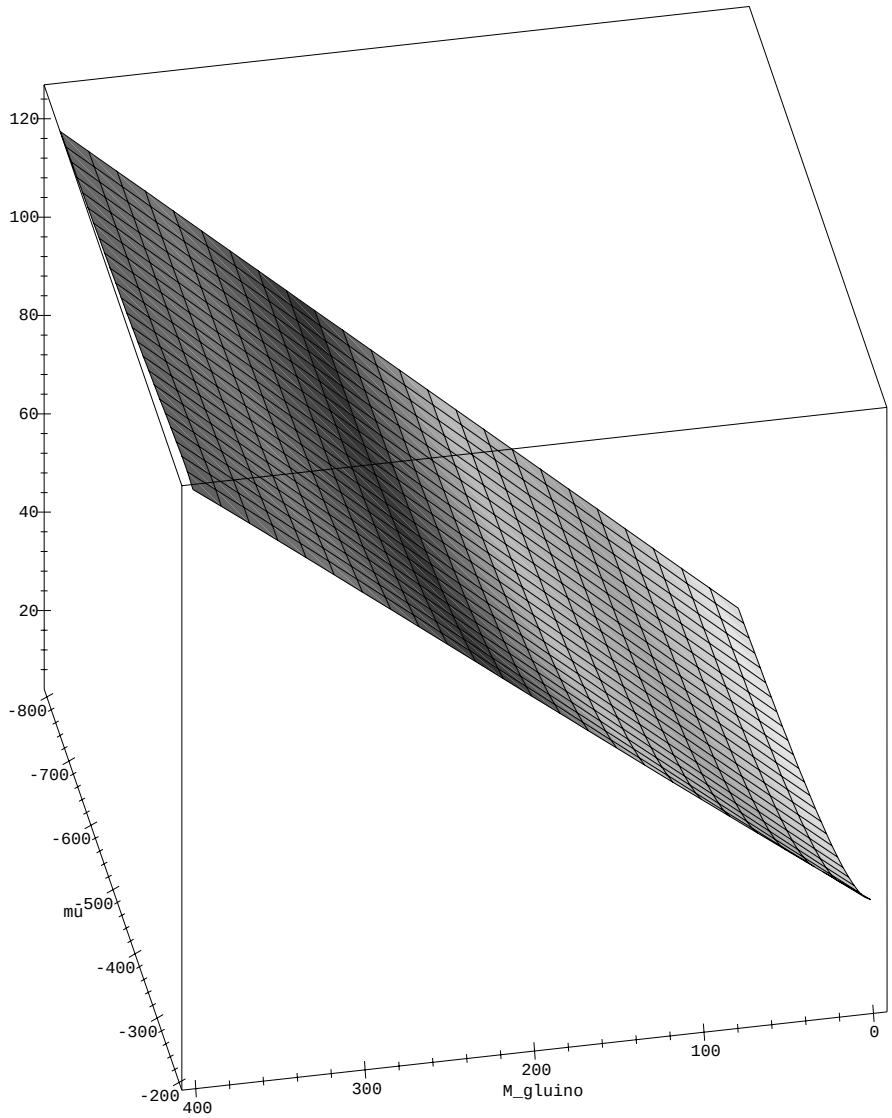

Figure 2.8: $M_{\tilde{\chi}_2^0}$ (vertical axis; in GeV/c^2) as a function of μ (left axis; in GeV/c^2) and $M_{\tilde{g}}$ (right axis; in GeV/c^2) for $\tan\beta = 2$.

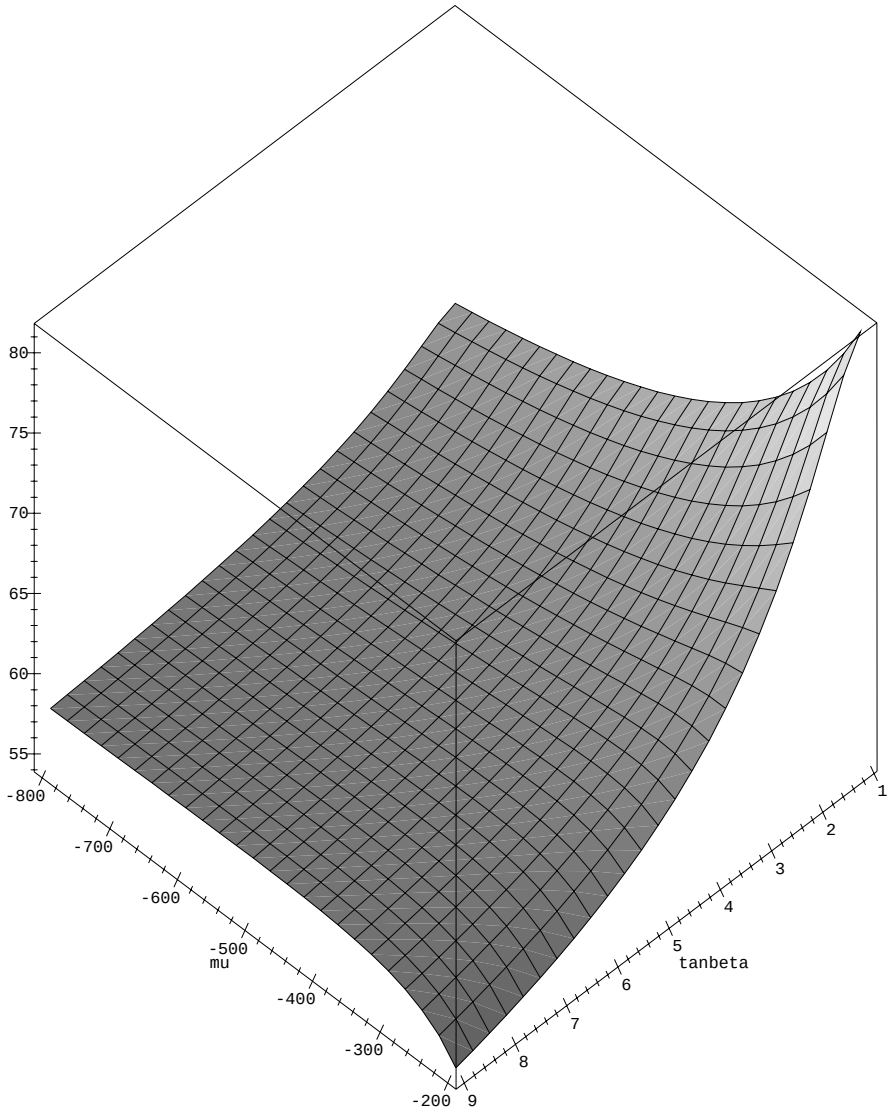

Figure 2.9: $M_{\tilde{\chi}_2^0}$ (vertical axis; in GeV/c^2) as a function of μ (left axis; in GeV/c^2) and $\tan\beta$ (right axis) for $M_{\tilde{g}} = 200$ GeV/c^2.

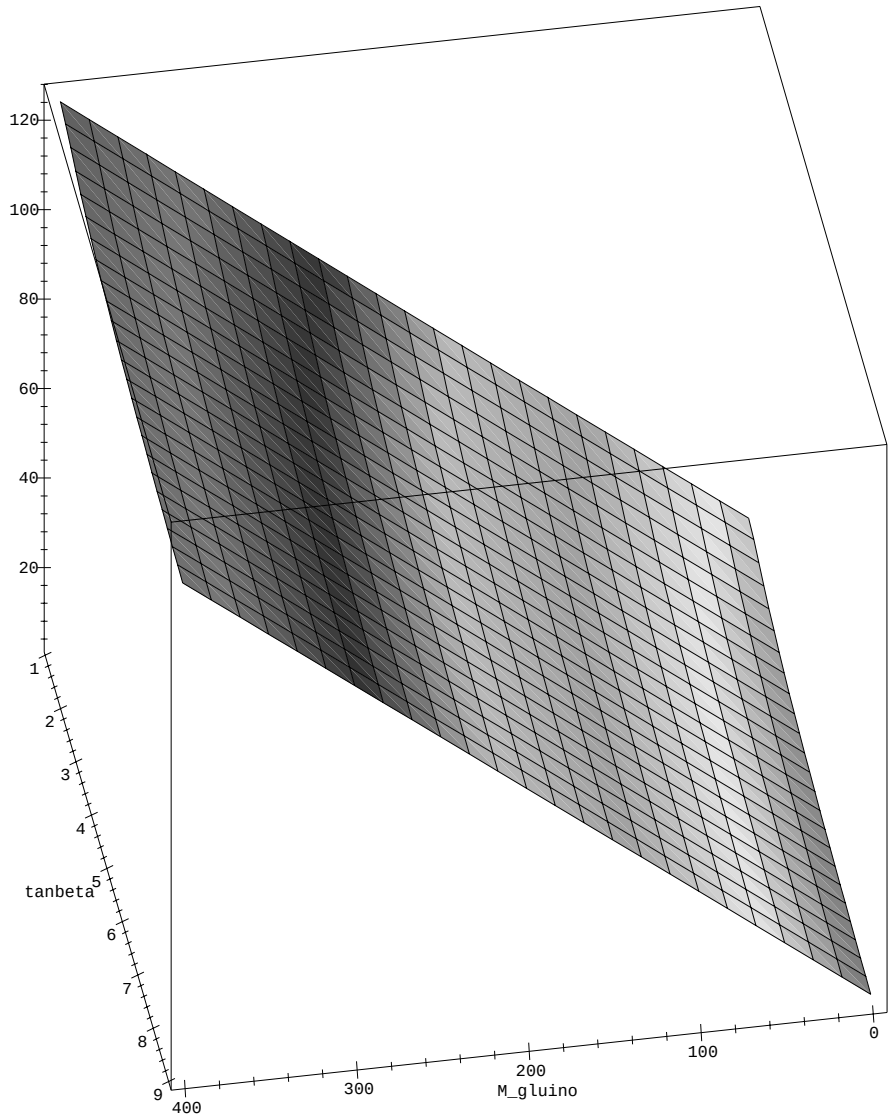

Figure 2.10: $M_{\tilde{\chi}_2^0}$ (vertical axis; in GeV/c^2) as a function of $\tan\beta$ (left axis) and $M_{\tilde{g}}$ (right axis; in GeV/c^2) for $\mu = -400$ GeV/c^2.

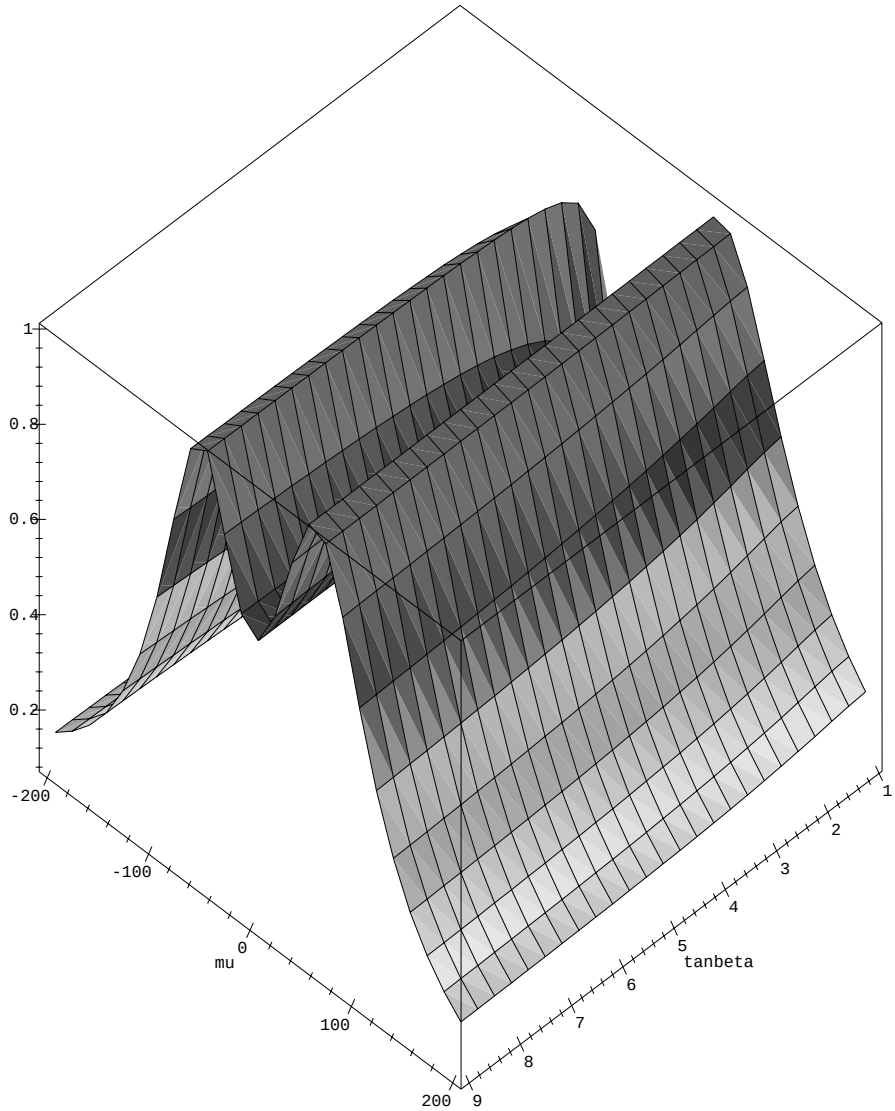

Figure 2.11: Higgsino fraction of $\tilde{\chi}_2^0$ as a function of μ (left axis; in GeV/c^2) and $\tan\beta$ for $M_{\tilde{g}} =$ 200 GeV/c^2 and $-200 \leq \mu \leq 200$ GeV/c^2.

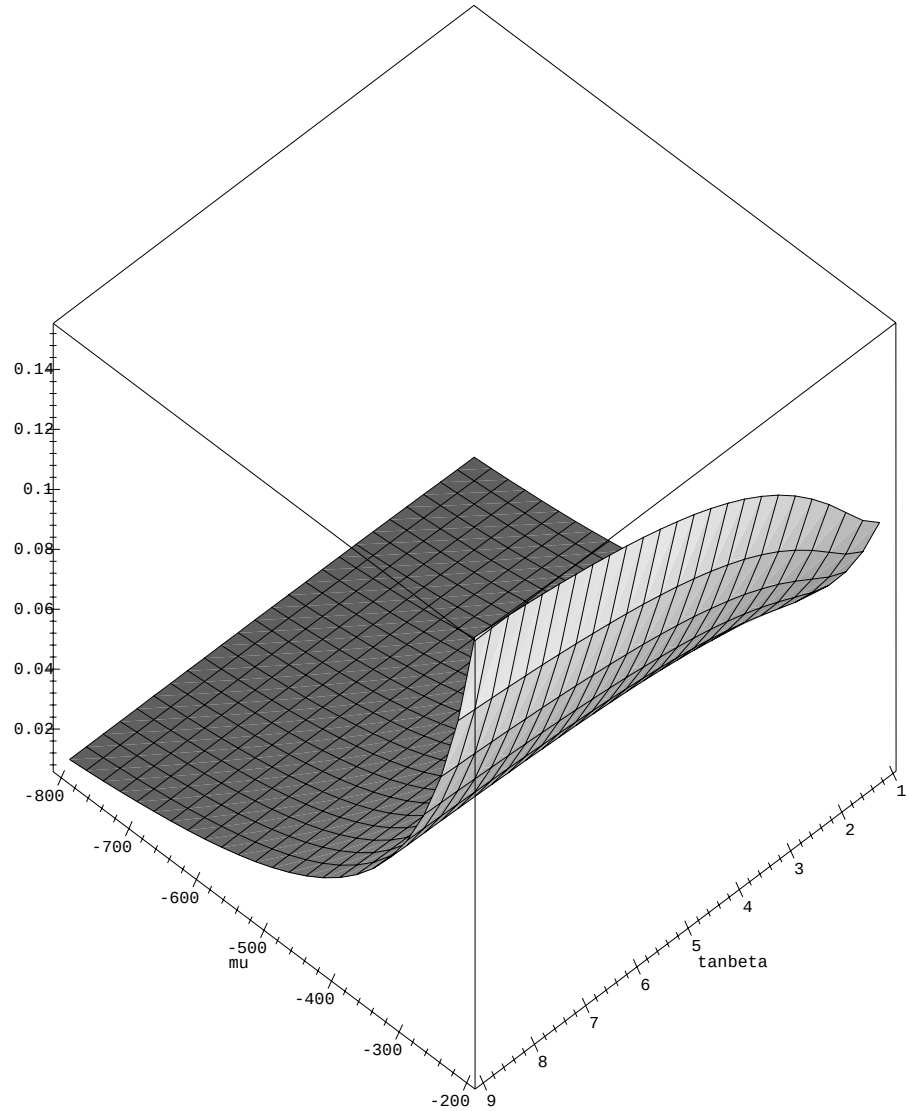

Figure 2.12: Higgsino fraction of $\tilde{\chi}_2^0$ as a function of μ (left axis; in GeV/c^2) and $\tan\beta$ for $M_{\tilde{g}} =$ 200 GeV/c^2 and $-800 \leq \mu \leq -200$ GeV/c^2.

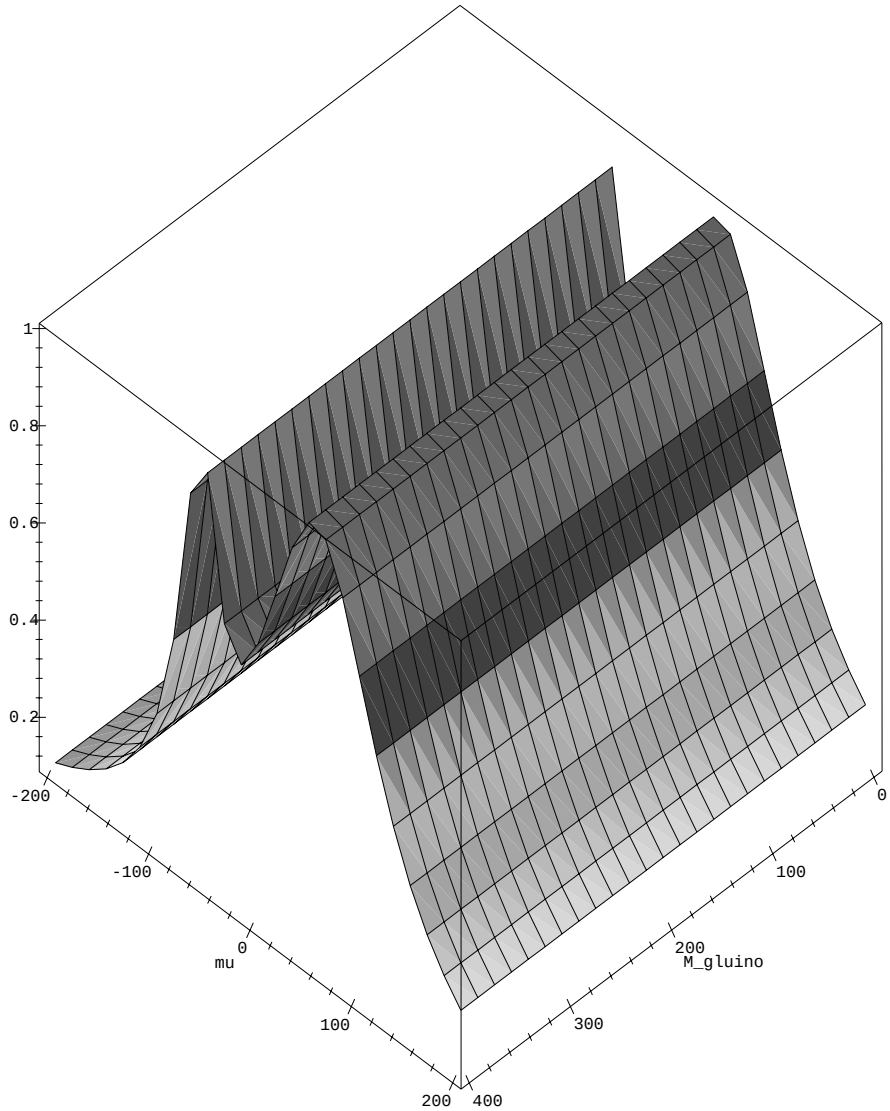

Figure 2.13: Higgsino fraction of $\tilde{\chi}_2^0$ as a function of μ (left axis; in GeV/c^2) and $M_{\tilde{g}}$ (right axis; in GeV/c^2) for $\tan\beta = 2$ and $-200 \leq \mu \leq 200$ GeV/c^2.

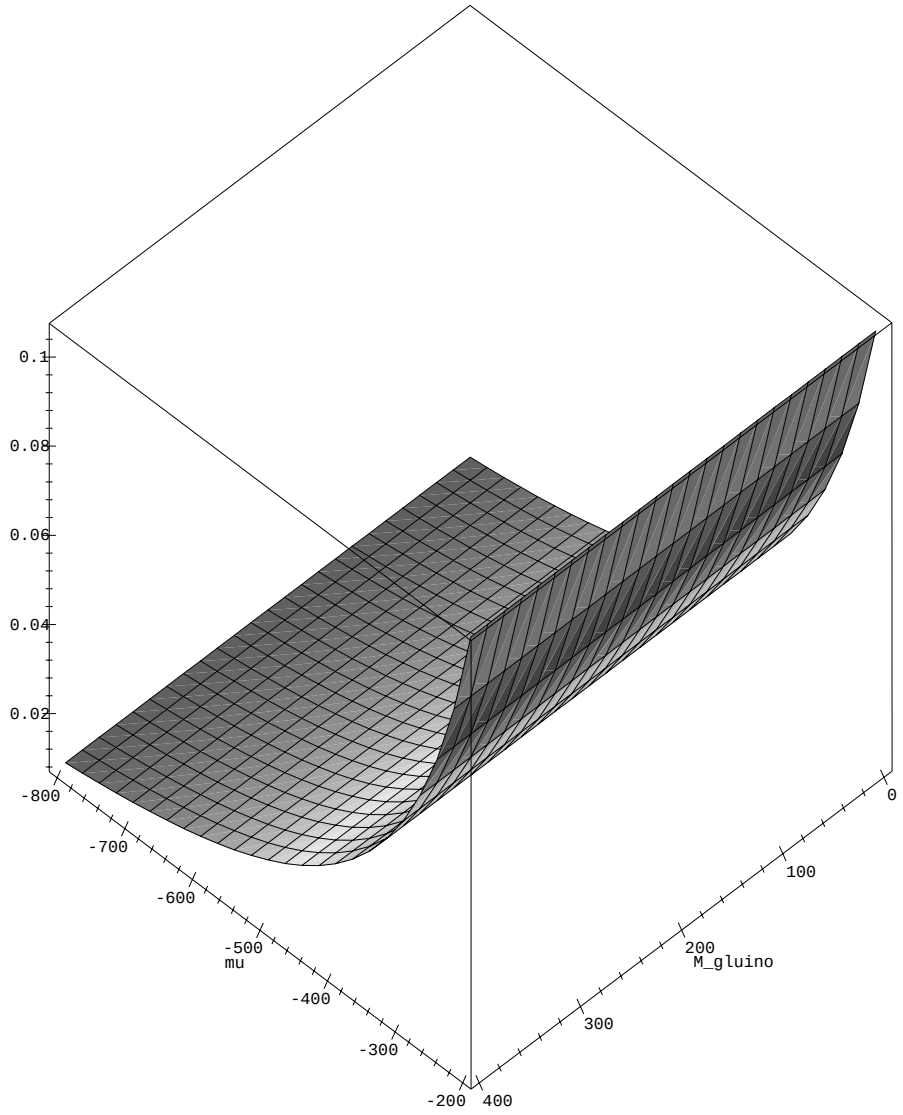

Figure 2.14: Higgsino fraction of $\tilde{\chi}_2^0$ as a function of μ (left axis; in GeV/c^2) and $M_{\tilde{g}}$ (right axis; in GeV/c^2) for $\tan\beta = 2$ and $-800 \leq \mu \leq -200$ GeV/c^2.

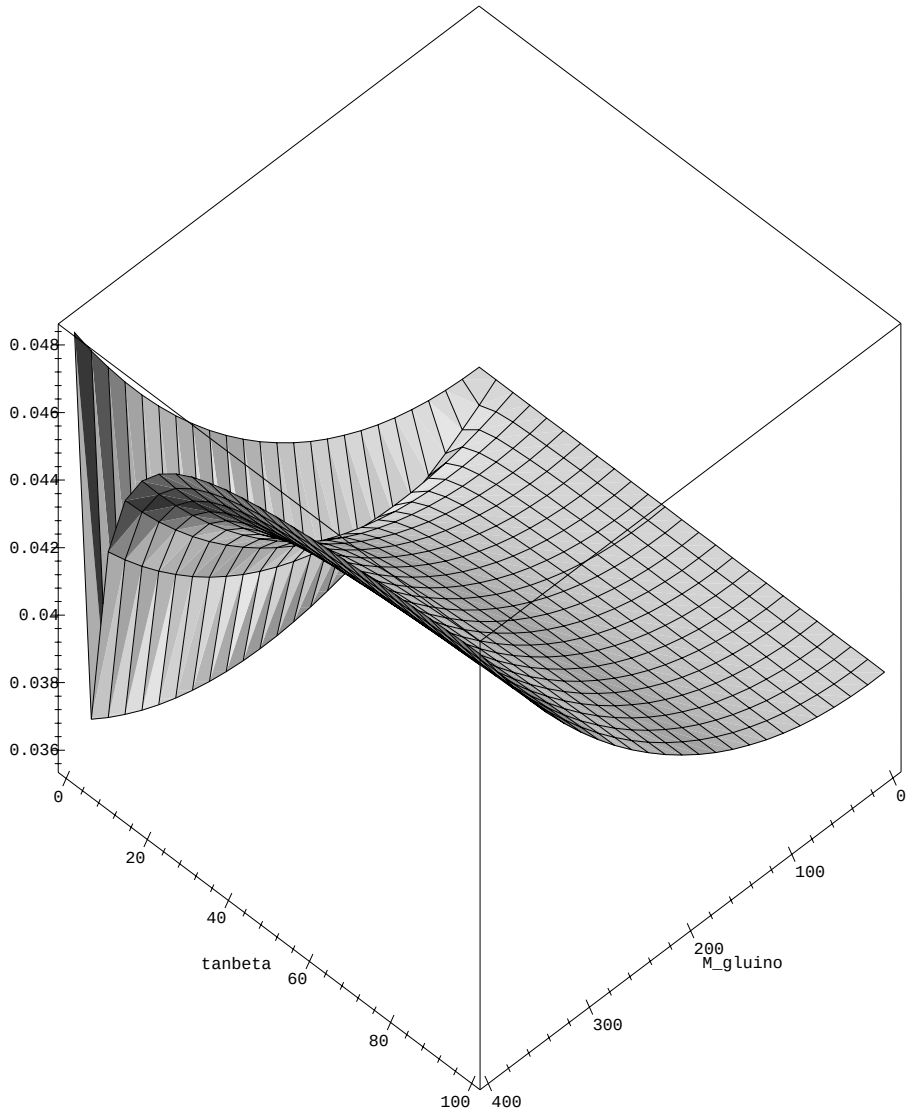

Figure 2.15: Higgsino fraction of $\tilde{\chi}_2^0$ as a function of $\tan\beta$ (left axis) and $M_{\tilde{g}}$ (right axis; in GeV/c^2) for $\mu = -400$.

2.1.3 Benefits of SUSY

Supersymmetry does not solve all of the problems of the Standard Model. For example, it is not a Grand Unified Theory. However, it does address many of the unanswered questions:

- In the Standard Model we have 17 free parameters[3]. In the MSSM we have over 100. However, if we make the model assumptions described above, we have a model with only six additional free parameters. This model, which contains far more particles than the SM, is more tightly constrained.
- In the SM there is no explanation for the heavy top quark. In the MSSM a heavy quark is required [18].
- The MSSM allows one to set the scale for electroweak symmetry breaking at ~ 100 GeV.
- SUSY *requires* the Higgs mechanism to remove divergences.
- While SUSY does not require gauge unification, it provides a mechanism (Equation 2.1) for unifying the coupling constants (as shown in Figure 2.16) and can thus be a GUT. This is not possible in the SM.
- SUSY describes phenomenology for higher mass scales than does the SM.
- SUSY provides a simple solution to the fine tuning or hierarchy problem. The rules for Feynman diagrams state that if we have two almost identical 1-loop diagrams, where one diagram has a fermion and the other has a boson (see Fig. 2.17), these two diagrams will cancel exactly. If these masses are not identical, the divergences are only logarithmic in nature and can be removed via renormalization. Thus, there is no need to fine-tune the masses of any of the particles at the GUT scale as their effects on particle masses will not be seen at the weak scale. This also provides a mechanism to cancel several other quadratic divergences; see Ref. [8] for a full explanation.
- Finally, SUSY provides an excellent candidate for cold dark matter in the form of the LSP.

There is no experimental evidence for SUSY. However, the above reasons make SUSY a compelling theory for experimentalists to explore.

[3]Six quark masses, three lepton masses, four KM matrix angles, α_{QED}, $\sin^2\theta_W$, M_{Z^0} and M_H.

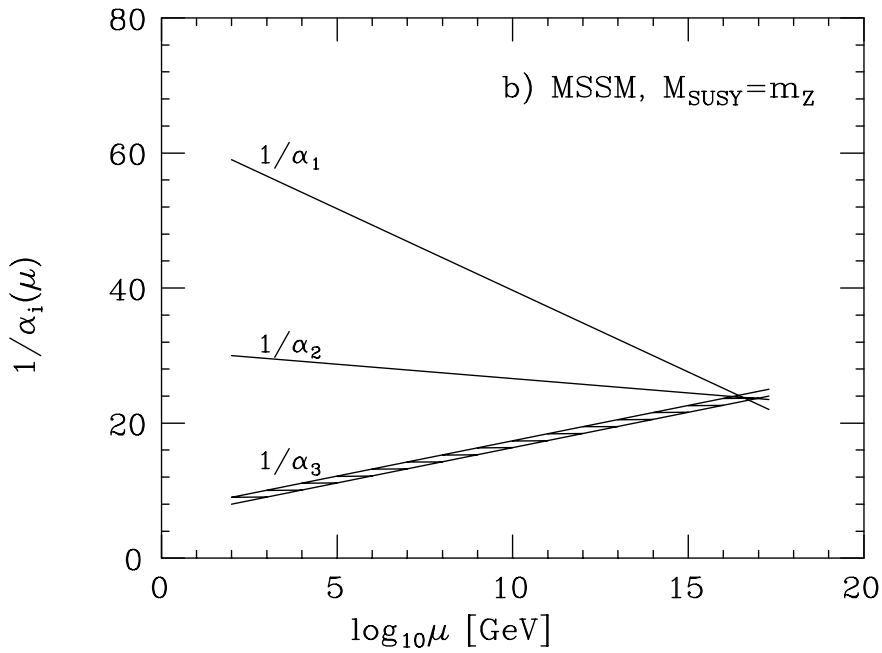

Figure 2.16: The extrapolation of the Standard Model gauge couplings to very high energies within the framework of SUSY with SU(5) unification. Note that, unlike in the SM case, the gauge couplings meet at a point. In addition, the scale of unification is higher than possible in the SM alone. This is a positive feature, especially in the context of proton decay. α_1 is the $\mathrm{SU(1)}_{\mathrm{hypercharge}}$ coupling constant, α_2 is the $\mathrm{SU(2)}_{\mathrm{weak}}$ coupling constant and α_3 is the $\mathrm{SU(3)}_{\mathrm{strong}}$ coupling constant. Adapted from [6].

2.2 Supersymmetric particle spectrum

In an earlier section I stated that in SUSY each particle gains a superpartner, effectively doubling the particle spectrum. That is somewhat misleading. For example, the quarks and leptons are spin-$\frac{1}{2}$ and thus exist in left- and (except possibly for the neutrinos) right-handed versions. How can a scalar superpartner have chirality? In the SM the left- and right-handed fermions are degenerate in mass. In SUSY the chiral labels correspond to different mass eigenstates.

The electroweak sector is more complex. In the Standard Model, we have the massless electroweak bosons $W^{\pm}$, W^3 and B. We also have an isospin doublet of complex scalar fields ϕ:

$$\phi = \begin{pmatrix} H^+ \\ H^0 \end{pmatrix} \text{ with } \begin{array}{l} H^+ \equiv (\phi_1 + i\phi_2)/\sqrt{2} \\ H^0 \equiv (\phi_3 + i\phi_4)/\sqrt{2} \end{array}$$

Three of the four degrees of freedom of the Higgs are 'eaten'[4] to give mass to the $W^{\pm}$ and the Z^0.

[4] 'Eaten' refers to the Higgs mechanism, which is beyond the scope of this dissertation. See, for example, Ref. [19]

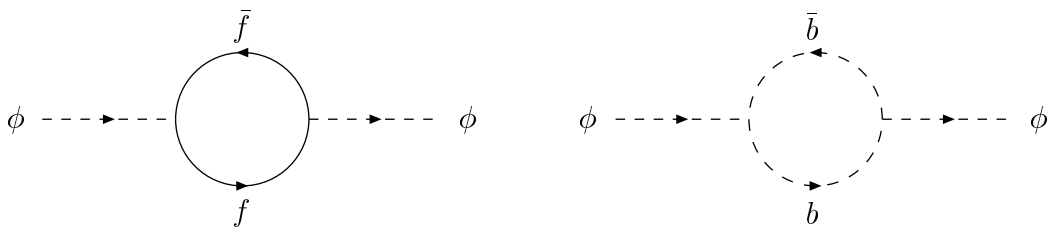

Figure 2.17: Feynman diagrams for fermionic (left) and bosonic (right) contributions to the Higgs' self-energy. The rules for Feynman diagrams state that if the same diagrams exist for both bosons and fermions of exactly the same mass, they cancel exactly.

The remaining degree of freedom is the physical, massive, Higgs H.

In SUSY things are much more complex. We again have the SM massless bosons $W^{\pm}$, W^3 and B. However, we now have *two* Higgs doublets

$$\begin{pmatrix} H^+ \\ H^0 \end{pmatrix}_u^{Y=+1} \text{ and } \begin{pmatrix} H^0 \\ H^- \end{pmatrix}_d^{Y=-1}.$$

Both doublets are needed to give masses to the up-type and down-type quarks and to cancel anomalies. As before, three of the degrees of freedom of the Higgs become the longitudinal polarization states of the $W^{\pm}$ and the Z^0. We now have *five* remaining degrees of freedom, which correspond to five physical Higgs: h^0, H^0, A^0 and $H^{\pm}$. We also have SUSY partners for each of the SM weak eigenstates:

$$\widetilde{W}^{\pm}, \widetilde{W}^3, \tilde{B}, \begin{pmatrix} \tilde{H}_1^+ \\ \tilde{H}_1^0 \end{pmatrix}_u \text{ and } \begin{pmatrix} \tilde{H}_2^0 \\ \tilde{H}_2^- \end{pmatrix}_d$$

These combine to form mass eigenstates:

$$\widetilde{W}^{\pm}, \tilde{H}_1^+, \tilde{H}_2^- \Longrightarrow \tilde{\chi}_1^{\pm}, \tilde{\chi}_2^{\pm}$$

and

$$\widetilde{W}^3, \tilde{B}, \tilde{H}_1^0, \tilde{H}_2^0 \Longrightarrow \tilde{\chi}_1^0, \tilde{\chi}_2^0, \tilde{\chi}_3^0, \tilde{\chi}_4^0$$

in order of increasing mass.

Note that we start and end with the same number of particles. In SM only, we have $W^{\pm}$ (2 charge $\cdot$ 2 helicity), W^3 (2 helicity), B (2 helicity), H^+ (2 doublet $\cdot$ 1 helicity) and H^0 (2 doublet

or [20].

$\cdot$ 1 helicity) for a total of 12 weak eigenstates and $W^{\pm}$ (2 charge $\cdot$ 3 helicity), Z^0 (3 helicity), γ (2 helicity), and H (1 helicity) again for a total for 12 physical (mass) eigenstates. For SUSY, we have

$$\begin{array}{ll} W^{\pm} & (2\cdot 2) \\ W^3 & (1\cdot 2) \\ B & (1\cdot 2) \\ H^+ & (1\cdot 2) \\ H^0 & (1\cdot 2) \\ H^0 & (1\cdot 2) \\ H^- & (1\cdot 2) \\ \hline & 16 \end{array} \Longrightarrow \begin{array}{ll} W^{\pm} & (2\cdot 3) \\ Z^0 & (1\cdot 3) \\ \gamma & (1\cdot 2) \\ h^0 & (1\cdot 1) \\ H^0 & (1\cdot 1) \\ A^0 & (1\cdot 1) \\ H^{\pm} & (2\cdot 1) \\ \hline & 16 \end{array}$$

for the SM particles, and

$$\begin{array}{ll} \widetilde{W}^{\pm} & (2\cdot 2) \\ \widetilde{W}^3 & (1\cdot 2) \\ \tilde{B} & (1\cdot 2) \\ \tilde{H}_1^+ & (1\cdot 2) \\ \tilde{H}_1^0 & (1\cdot 2) \\ \tilde{H}_2^- & (1\cdot 2) \\ \tilde{H}_2^0 & (1\cdot 2) \\ \hline & 16 \end{array} \Longrightarrow \begin{array}{ll} \widetilde{\chi}_1^{\pm} & (2\cdot 2) \\ \widetilde{\chi}_2^{\pm} & (2\cdot 2) \\ \widetilde{\chi}_1^0 & (1\cdot 2) \\ \widetilde{\chi}_2^0 & (1\cdot 2) \\ \widetilde{\chi}_3^0 & (1\cdot 2) \\ \widetilde{\chi}_4^0 & (1\cdot 2) \\ \hline & 16 \end{array}$$

for the SUSY partners. Notice further that, as needed, we have the same number of SM particles and SUSY partners. Table 2.1 lists the entire SM and SUSY particle spectrum.

2.3 Supersymmetric discovery channels

There are two different techniques one can use to search for evidence of new physics. One can either examine well known (and predicted!) spectra for anomalies, or one can search for previously unpredicted signals. The CDF collaboration is currently searching for several possible SUSY signals. Analyses searching for evidence of $\tilde{q}$ and $\tilde{g}$ production via multiple jets plus $\not{E}_T$[5] [21] and evidence of a light $\tilde{t}$ use the former technique. This analysis and a search for $\tilde{q}$ and $\tilde{g}$ production via dijets plus like-sign dileptons use the latter technique.

Before discussing the particular SUSY signature for which we search, it is instructive to examine the closest SM analogy: $W^{\pm}Z^0$ production. At the Tevatron (with center of mass energy $(\sqrt{s}) = 1800$ GeV) the production cross section for $p\bar{p} \to W^{\pm}Z^0$ is 2.5 pb. Thus, in 100 pb^{-1} of data, we can expect 250 events. The $W^{\pm}$ can decay to a quark and a different antiquark or to

[5] $\not{E}_T$ is missing transverse energy. Conservation of energy and momentum allows one to extract the energy and direction of unseen, non-interacting particles.

Table 2.1: SM (left side) and SUSY (right side) particle spectrum. The arrows indicate the mixing of weak eigenstates to form mass eigenstates. The braces ({}) indicate what is mixed in the weak sector. Adapted from Ref. [10].

Quarks				Squarks				
(spin-$\frac{1}{2}$)	$\binom{u}{d}_L$	u_R	d_R	(spin-0)	$\binom{\tilde{u}}{\tilde{d}}_L$	$\tilde{u}_R$	$\tilde{d}_R$	
	$\binom{c}{s}_L$	c_R	s_R		$\binom{\tilde{c}}{\tilde{s}}_L$	$\tilde{c}_R$	$\tilde{s}_R$	
	$\binom{t}{b}_L$	t_R	b_R		$\binom{\tilde{t}}{\tilde{b}}_L$	$\tilde{t}_R$	$\tilde{b}_R$	$\longrightarrow \tilde{t}_{1,2}, \tilde{b}_{1,2}$
Leptons				Sleptons				
(spin-$\frac{1}{2}$)	$\binom{e}{\nu_e}_L$	e_R		(spin-0)	$\binom{\tilde{e}}{\tilde{\nu}_e}_L$	$\tilde{e}_R$		
	$\binom{\mu}{\nu_\mu}_L$	μ_R			$\binom{\tilde{\mu}}{\tilde{\nu}_\mu}_L$	$\tilde{\mu}_R$		
	$\binom{\tau}{\nu_\tau}_L$	τ_R			$\binom{\tilde{\tau}}{\tilde{\nu}_\tau}_L$	$\tilde{\tau}_R$	$\longrightarrow$	$\tilde{\tau}_{1,2}$
Gauge bosons				Gauginos				
(spin-1)	g			(spin-$\frac{1}{2}$)	$\tilde{g}$			
	γ				$\tilde{\gamma}$		Neutralinos	
	Z				$\widetilde{Z}$		$\longrightarrow \widetilde{\chi}^0_{1,2,3,4}$	
	$W^\pm$				$\widetilde{W}^\pm$		$\{\tilde{\gamma}, \widetilde{Z}, \widetilde{H}^0_{1,2}\}$	
Higgs bosons				Higgsinos			Charginos	
(spin-0)	h, H, A			(spin-$\frac{1}{2}$)	$\widetilde{H}^0_{1,2}$		$\longrightarrow \widetilde{\chi}^\pm_{1,2}$	
	$H^\pm$				$\widetilde{H}^\pm$		$\{\widetilde{W}^\pm, \widetilde{H}^\pm\}$	

a charged lepton and the corresponding antineutrino. Similarly, the Z^0 can decay to a quark–antiquark pair or to a lepton-antilepton pair. The various combinations of these possible decays lead to final states with four quark jets; two quark jets, a charged lepton and a neutrino; two quark jets and a lepton–antilepton pair; or three charged leptons and a neutrino. As mentioned above, this SUSY analysis searches for events with few or no SM analogs (see below for a discussion of backgrounds). Thus, the closest SM analog to our expected events is the type with three charged leptons and a neutrino. The branching ratio (BR) to leptons (electron and muon) for the $W^\pm$ is 0.212 and 0.0673 for the Z^0 [5]. Thus, if one searched for the leptonic decays of $W^\pm Z^0$, one could expect to see 0.54 events in 113 pb^{-1} (allowing for a total detection efficiency of 15%). CDF has completed such a search [22] and sees 1 event[6].

As described above, the SUSY analogs to $W^\pm$ and Z^0 are $\widetilde{\chi}^\pm_1, \widetilde{\chi}^\pm_2$ and $\widetilde{\chi}^0_1, \widetilde{\chi}^0_2, \widetilde{\chi}^0_3, \widetilde{\chi}^0_4$, respectively. If we assume $\mathrm{M}_{\tilde{\chi}^\pm_1}$ and $\mathrm{M}_{\tilde{\chi}^0_2}$ to be on the order of $\mathrm{M}_{W^\pm}$ and M_{Z^0}, we can expect comparable

[6]This event is excluded from this analysis as we explicitly remove Z^0 events.

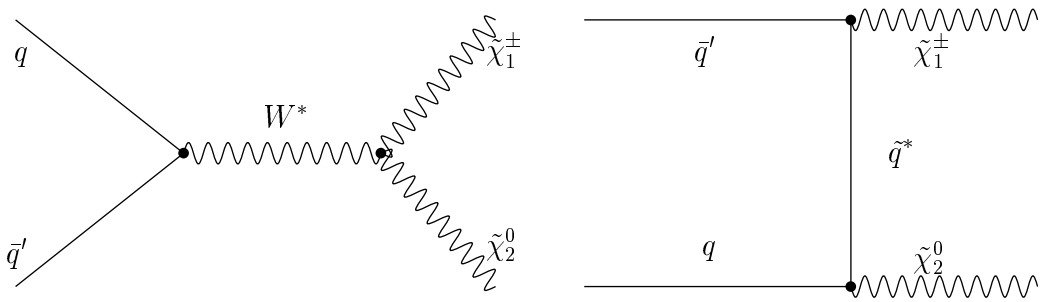

Figure 2.18: Associated $\tilde{\chi}_1^\pm\tilde{\chi}_2^0$ production through s-channel via virtual $W^\pm$ exchange (left) and t-channel via virtual $\tilde{q}$ exchange (right) at the Tevatron. For $\tilde{\chi}_1^\pm$ and $\tilde{\chi}_2^0$ masses near $W^\pm$ and Z^0 masses we can expect a measurable rate of production. Note that these two modes interfere destructively, so a large $\tilde{q}$ mass leads to a higher production cross section.

rates of $W^\pm Z^0$ production and $\tilde{\chi}_1^\pm\tilde{\chi}_2^0$ production.[7] We search for evidence of associated production of $\tilde{\chi}_1^\pm$ and $\tilde{\chi}_2^0$,[8] where we have s-channel and t-channel (Figure 2.18) production dominating. These two modes interfere destructively, so a large $\tilde{q}$ mass (which suppresses the t-channel) results in a higher production cross section at the Tevatron. As in the $W^\pm Z^0$ case, we have a variety of possible decay modes available which result in a variety of final states. The addition of SUSY particles increases the decay modes. We are still interested in final states with three charged leptons, so we require events such as those shown in Figures 2.19 and 2.20. Note that if the $\tilde{\ell}$ mass is less than the $\tilde{\chi}_1^\pm$ or $\tilde{\chi}_2^0$ masses, we get two body decays. Regardless of the intermediate stages, the final state always involves a lepton-antilepton pair, an additional lepton, a neutrino, and two $\tilde{\chi}_1^0$: three leptons and $\not{E}_T$. The directions of the escaping neutrino and two $\tilde{\chi}_1^0$ are completely uncorrelated so the amount of $\not{E}_T$ can vary from a small to a substantial amount. This is a very distinctive signature, with very little Standard Model background.

2.4 Background

Background events are those events which look like signal events but are instead from a different, undesired process. There are two different types of background to this analysis: those with three (or more) real leptons, and those with two real leptons and an additional object which appears to be a real lepton. Events with three real leptons include $W^\pm Z^0$, Z^0Z^0, $t\bar{t}$ and $b\bar{b}$. Events with two real leptons include $W^\pm W^\pm$, $c\bar{c}$ and Drell-Yan (γ and Z^0). Some of these events have very small production cross sections, such as the diboson events. Other events have very distinctive signatures,

[7] This is not an unreasonable assumption, as the limits on $M_{\tilde{\chi}_1^\pm}$ and $M_{\tilde{\chi}_2^0}$ when this analysis began were $\simeq 45-47$ GeV/c^2 [23]. Also, since the production cross section falls as the mass of the object increases, lighter $\tilde{\chi}_1^\pm\tilde{\chi}_2^0$ would have a higher production cross section than $W^\pm Z^0$ production.

[8] We do not search for $\tilde{\chi}_1^\pm\tilde{\chi}_1^0$ production since we assume $\tilde{\chi}_1^0$ to be the LSP and thus is invisible. The resulting signal from this production would be a single charged lepton plus missing energy, or a rather $W^\pm$-like signature.

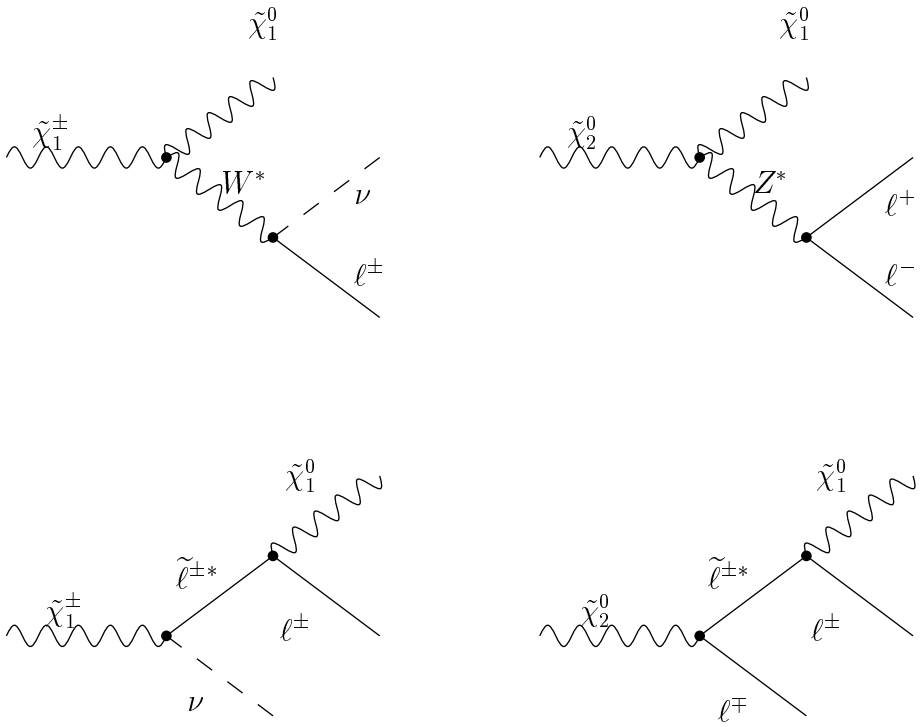

Figure 2.19: Three body decay modes for charginos (left) and neutralinos (right). These modes occur when the slepton mass is larger than the chargino and neutralino masses so the decays occur via virtual $W^\pm$s and Z^0s (top) or virtual sleptons (bottom). The final state is always three charged leptons (electrons or muons) plus two LSPs and a neutrino which result in measurable missing energy.

which allows us to remove these background events. Techniques for removing background are discussed in Chapter 4.

We do not search for events where the $\tilde{\chi}_1^\pm$ decays to quarks (and thus to jets) as that mode will have substantial background from Z^0 plus jets.

2.5 Naturalness

Having reduced the MSSM parameter space to the 6 free variables of SiMSSM, some guidance is still necessary to know where in SiMSSM space one should be searching for evidence of SUSY. Obviously, we should start by searching in the low mass ($\mathrm{M}_{\tilde{q}}$ and $\mathrm{M}_{\tilde{g}}$) region, but what values of μ, $\tan\beta$, $\mathrm{A_T}$ and $\mathrm{M_{H_A}}$ should we use? Some adjustment of the parameters can be done to produce signals that can be easily detected at current experiments. However, that results in 'searching under the lamp post' and is not always desirable. Also, we can continue to search for evidence of SUSY for all eternity. If no sparticles are found, when will we know that SUSY is not a viable theory?

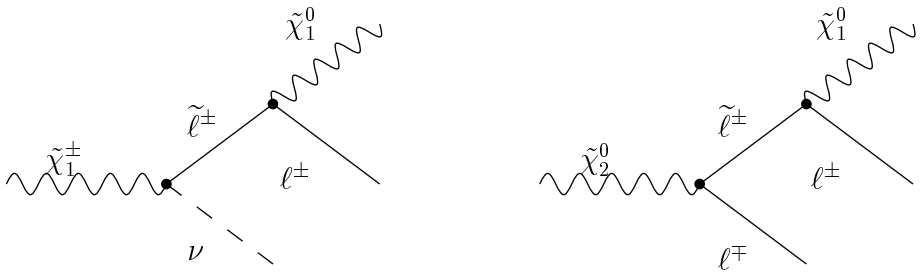

Figure 2.20: Two body decay modes for charginos (left) and neutralinos (right). These modes occur when the slepton mass is smaller than that of the chargino and neutralino so the predominant decay mode is via real sleptons. As above, the final state always includes three charged leptons and missing energy.

Naturalness attempts to provide some measure of the "desirability" of a particular point in the 6-dimensional SiMSSM space.

There are several different definitions of naturalness (γ). Some examine the mass splitting between the particles and the sparticles.[9] However, the definition of naturalness used for this analysis examines the sensitivity of the masses of the superpartners to fine-tuning of the input parameters ($\mathrm{M}_{\tilde{q}}$, $\mathrm{M}_{\tilde{g}}$, μ, $\tan\beta$, $\mathrm{A_T}$ and $\mathrm{M_{H_A}}$) [24]. To determine the naturalness for a particular point in SiMSSM space, one must first generate Monte Carlo for many different points in a wide region of parameter space. Then one looks for large local variations in any of the physical output parameters. Regions with large local variations of an output parameter *compared to the entire range of the output parameter* have a higher value of naturalness than regions with small local variations. Regions with γ on the order of 1 are considered natural. Regions with large γ are un-natural (how large depends on the observer).

Figure 2.21 shows the naturalness as a function of mass for the $\tilde{\chi}_1^\pm$. An important question is how large the 'local' region should be. In Figure 2.21 the naturalness is calculated for two different ranges of integration $a/\delta a < 4$ and $a/\delta a < 8$ where δa is the width of the range of integration ($\delta a = a_+ - a_-$) and a is one of the input parameters. Figure 2.22 shows the naturalness for a variety of SUSY particles as a function of their masses.

It is important to realize that naturalness is only a guide to SiMSSM space. Nature is wherever nature is, regardless of the naturalness of that point.

[9] If the mass splitting becomes too large, the anomalies discussed in Section 2.1.3 no longer cancel and SUSY loses much of its appeal.

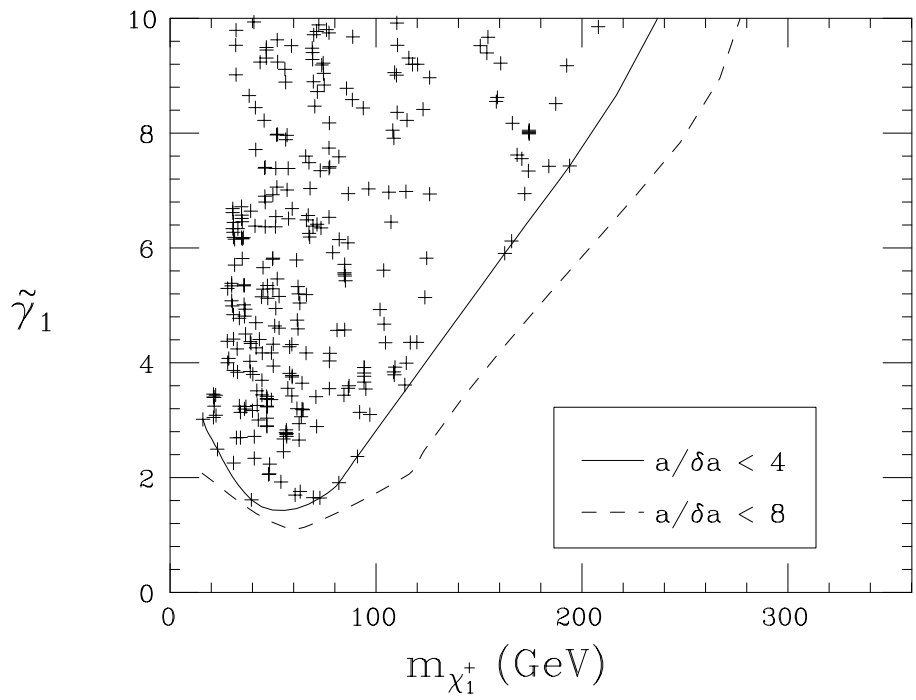

Figure 2.21: Each + represents the naturalness γ for a different point in SiMSSM space as a function of $M_{\tilde{\chi}_1^\pm}$. The lines are the lowest value of the naturalness for a particular $M_{\tilde{\chi}_1^\pm}$; see the text for the definition of a and δa. Note that there is a clear minimum for the naturalness of $M_{\tilde{\chi}_1^\pm}$ at $M_{\tilde{\chi}_1^\pm} \sim 60$ GeV/c^2. Adapted from Ref. [25].

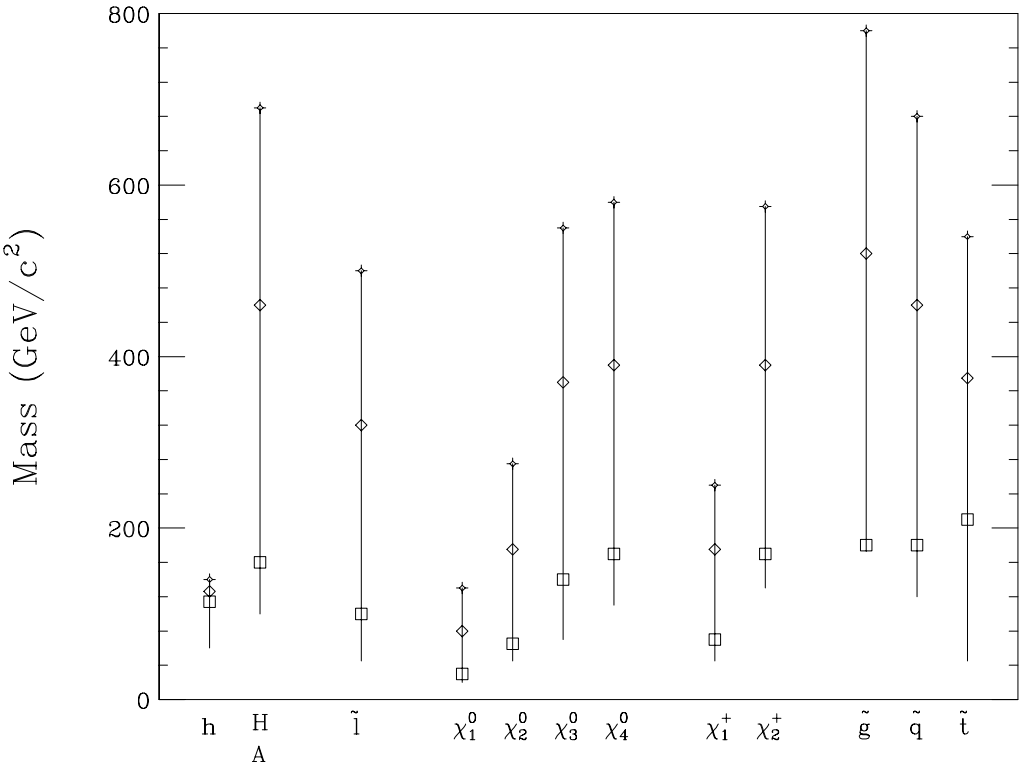

Figure 2.22: The naturalness for a variety of different sparticles. The bottom of each line is the current world limit, the box (□) represents a naturalness of 1, the diamond (◇) a naturalness of 5 and the top of the line (+) a naturalness of 10. Note that experiment is only now starting to approach natural values for a few sparticles. Adapted from Ref. [25].

Chapter 3

Apparatus

The Tevatron at the Fermi National Accelerator Laboratory and the Collider Detector at Fermilab (CDF) are extremely complex devices and are described in detail elsewhere [26, 27, 28]. However, I will briefly explain the methods for producing colliding beams at the Tevatron and the subsystems of CDF that are germane to this analysis.

3.1 The Tevatron

The center of mass energy ($\sqrt{s}$) of the proton-antiproton ($p\bar{p}$) beams at CDF is 1.8 TeV, the highest in the world. At room temperature, the average proton energy is $\simeq \frac{1}{40}$ eV, significantly less than the needed energy. Thus, the protons must be accelerated to roughly $0.99944c$, and the anti-protons ($\bar{p}$s) must be created and then accelerated.

The proton beam starts as hydrogen gas in an ordinary gas cylinder. This gas is ionized by adding an additional electron to form H^-.[1] The first acceleration occurs in the Cockcroft-Walton, which is essentially a giant capacitor. Roughly 1.4×10^{14} H^- ions exit the Cockcroft-Walton per bunch, each with energy 750 keV. The remainder of the acceleration is done with radio-frequency (RF) cavities. An overview of the entire accelerator complex is shown in Figure 3.1. The H^- ions leaving the Cockcroft-Walton are injected into a linear accelerator, the Linac. The Linac is a 150 m long series of nine radio-frequency (RF) cavities[2] that increase in length in the direction of increased

[1] H^+ are not used since the accelerated object must be injected into the Booster. If the object being accelerated by the LINAC has the same charge as the sign of particles in the Booster, it would be impossible to add more particles: particles in the Booster rotate counter-clockwise and the injection process rotates particles clockwise.

[2] The RF cavities produce an electric field that rapidly changes direction. During the phase when the electric field would tend to retard the motion of the H^-, the ions coast along in drift tubes that shield them from the field.

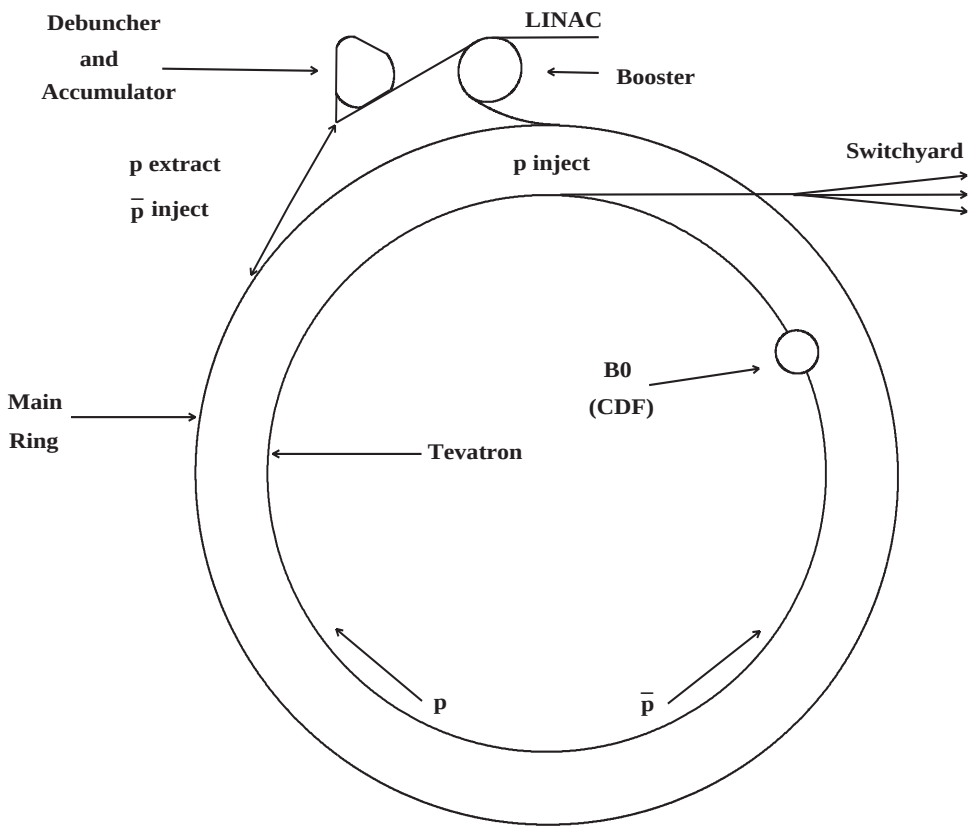

Figure 3.1: Overview of the accelerator complex at Fermilab. H^- ions are injected into the LINAC from the Cockcroft-Walton, travel to the Booster, then to the Main Ring, and finally to the Tevatron. Some protons are extracted from the Main Ring and are used to make anti-protons. The anti-protons are re-injected into the Main Ring and then into the Tevatron. The final center of mass energy is $\sqrt{s} = 1.8$ TeV. Note that the Tevatron and Main Ring have the same radius (1 km) and in fact occupy the same tunnel.

acceleration. This is to provide constant acceleration along the entire length of the Linac. At the exit of the Linac the H^- ions have a kinetic energy of 400 MeV.

Once the H^- ions leave the Linac, they pass through a thin carbon foil to strip off the two electrons. The bare proton is then accelerated in the Booster, a rapid cycling synchrotron[3]: a 500 m radius ring of conventional magnets (used to focus and steer the beam) and an RF cavity (to accelerate the beam). After traveling around the Booster 20,000 times, protons leave the Booster

[3]In a synchrotron a single RF cavity does all the acceleration. The rate of the change of the electric field can be precisely controlled (hence *rapid cycling*) to provide continuous acceleration. A constant field would only provide acceleration once. During the phase when the electric field in the Booster would retard the protons they are in another portion of the ring.

with kinetic energy of 8 GeV in bunches of 10^{10} particles and are injected into the Main Ring. Similar to the Booster, the Main Ring is a 1 km radius ring of 3.5 kGauss conventional dipole magnets (used for steering the beam) and quadrupole magnets (used for focusing the beam) and a single RF cavity for acceleration. The protons leave the Main Ring with kinetic energy of 150 GeV and are injected into the Tevatron. Like the two previous rings, the Tevatron is a rapid cycling synchrotron. Unlike them, however, the magnets in the Tevatron are super-conducting. This fact allows the magnetic field strength (4 Tesla) in the Tevatron to be quite high and allows the Tevatron to accelerate the protons to 900 GeV.

Antiprotons do not occur naturally and must be manufactured. To do this, some of the protons from the Main Ring are removed and sent to the Antiproton Source. These protons are focused on a tungsten target. Collisions with the target produce, among other particles, $\bar{p}$s. For every million protons sent into the Antiproton Source, about 20 $\bar{p}$s are produced. Using a magnetic field, the $\bar{p}$s are selected and send to the Debuncher and then the Accumulator where they are stored until enough have been produced. The $\bar{p}$s are then sent back into the Main Ring and the Tevatron and are accelerated to 900 GeV. Since the $\bar{p}$s have charge opposite to the proton, the same ring (with the same magnetic field) can be used to circulate the $\bar{p}$s in the direction opposite to that of the protons.

When the Tevatron is operating in collider mode, six bunches of protons collide with six bunches of antiprotons in the center of CDF. Each bunch of protons contains about 2×10^{11} p and travels clockwise along the ring (looking down from above). Each bunch of antiprotons contains about 6×10^{10} $\bar{p}$ and travels counter-clockwise. Special magnets called low beta quadrupoles focus the beam spot to about 60 μm across to increase the probability of a collision. These crossings occur every 3.5 μseconds to produce an instantaneous luminosity ($\mathcal{L}$) on the order of $10^{31}\text{cm}^{-2}\text{s}^{-1}$, where $\mathcal{L}$ is defined to be the interaction cross section (σ) times the number of particles (N). The longitudinal interaction region of the beam is about 30 cm. The data taking periods for this analysis went from August 1992 until May 1993 ("Run IA": 19.1 pb^{-1}) and from August 1994 until December 1995 ("Run IB": 87.7 pb^{-1}) for a total integrated luminosity of 107 pb^{-1}.

3.2 The Collider Detector at Fermilab

The Collider Detector at Fermilab (CDF) is a solenoidal detector with forward-backward and azimuthal symmetry. It has tracking chambers inside a superconducting solenoidal magnet, with electromagnetic (EM) and hadronic (HAD) calorimeters directly outside to measure the energy of electrons, photons and jets. Furthest from the beam line are muon chambers to identify muons. Figure 3.2 shows a 3-dimensional perspective overview of the detector, and Figure 3.3 is a 2-dimensional view of one quarter of the detector. The detector is symmetric about the interaction region.

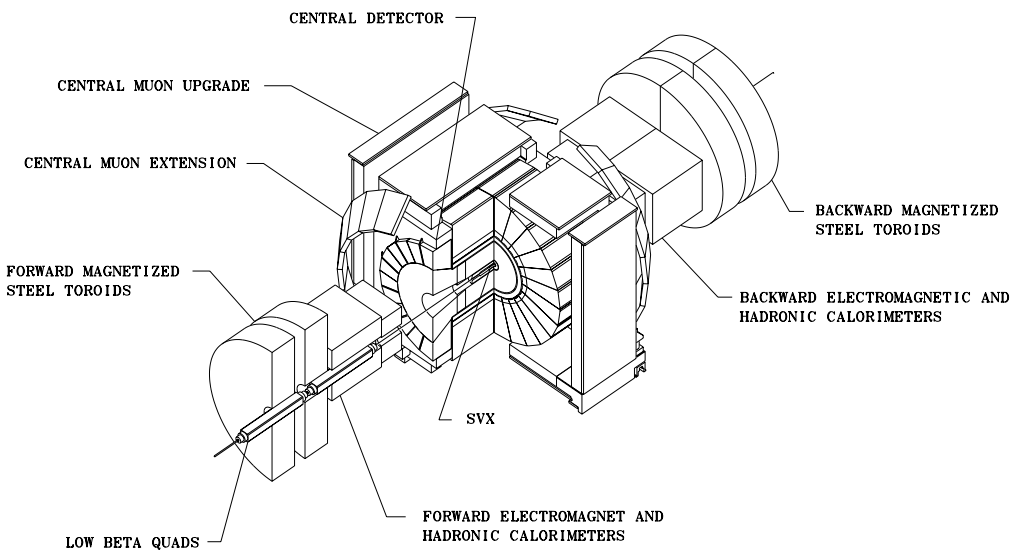

Figure 3.2: A perspective view of CDF. The entire detector is approximately 27 m long, 10 m high, and weighs 5000 tons.

CDF uses a right-handed coordinate system where the z-axis is along the proton direction, the y-axis is up and the x-axis is radially outward from the center of the ring. We assume the nominal interaction point to be at the center of the detector (0,0,0) and define θ to be the polar angle along the positive z-axis. However we more commonly use the pseudo-rapidity $\eta \equiv -\ln\tan(\theta/2)$. This has the advantage that for particles with large momentum compared to their masses (such as at the Tevatron) the shape of the pseudo-rapidity distribution, $dN/d\eta$ is constant.

Because of forward scattered particles (the remnants of the p and $\bar{p}$), we cannot measure the total momentum of an event. However we can measure the momentum of all interacting particles transverse to the beamline. Thus we generally deal with transverse momentum (P_T) and transverse energy (E_T). They are defined as follows:

$$\begin{aligned} E_T &= E \times \sin\theta \\ P_T &= P \times \sin\theta \end{aligned} \tag{3.1}$$

For particles with momenta large compared to their masses (such as electrons and muons at the Tevatron), the E_T and P_T are nearly identical. However, E_T refers to energy measured in a calorimeter and P_T refers to momentum measured in the Central Tracking Chamber (CTC).

This analysis is concerned with the identification of electrons and muons. Thus, the EM calorimeter and the muon chambers are most important to this search and will be described in some detail. The tracking chambers are important in determining the momentum of muons. Also, since a cut on the missing transverse energy ($\not{E}_T$) is very important to reject background, I will

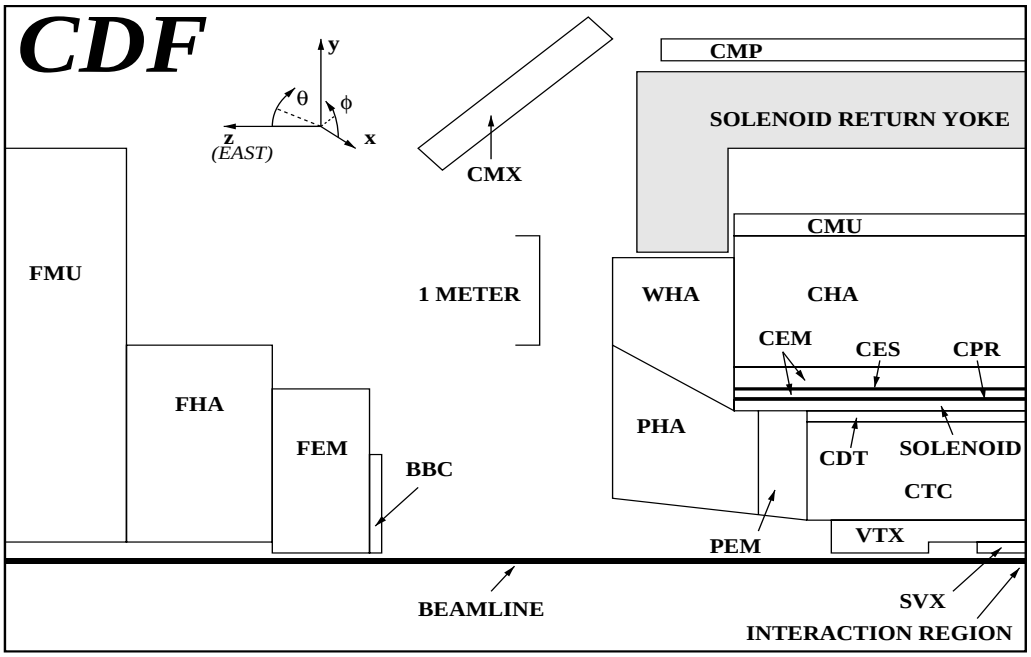

Figure 3.3: A one quarter view of CDF. For this analysis, the most important detectors are the central (CEM) and plug (PEM) electromagnetic calorimeters, the central muon chambers (CMU, CMP, CMX), and the central tracking chamber (CTC). For total energy measurement (necessary to determine the missing energy), the hadron calorimeters (CHA, WHA, PHA, FHA) and the forward electromagnetic (FEM) calorimeters are also important. The BBCs are used to measure the luminosity. The hadron TDCs (not shown) are situated in electronic crates on the faces of the Endplug.The detector is symmetric about the interaction region.

briefly describe the HAD calorimeters. Cosmic rays are rejected using the hadron Time-to-Digital-Converters (HTDC) so I will describe them. This analysis requires an accurate measurement of the luminosity so I will describe the technique used to determine the total integrated luminosity.

The proton and anti-proton beams cross inside the detector every 3.5 μseconds, with an average of 1.3 interactions per crossing [29] (at the Run IB average instantaneous luminosity of 8 $\times 10^{30}\text{cm}^{-2}\text{s}^{-1}$) for an average interaction rate of 370 kHz. It is impossible for us to record data to tape at that rate, so we use a three level trigger system to reduce the data rate to one that can be recorded. I will briefly describe that system.

3.2.1 Calorimeters

The calorimeters at CDF all use a projective tower geometry with constant η towers that points back to the nominal interaction region. As seen in Figure 3.3, the calorimeters consist of several subsystems. For this analysis, we are concerned with the central (CEM) and plug (PEM) electromagnetic calorimeters, which cover the η regions $0 \leq |\eta| \leq 1.1$ and $1.1 \leq |\eta| \leq 2.4$, respectively. We

Table 3.1: The properties of the various CDF calorimeter systems. Energy resolutions for the hadronic calorimeters are for pions and the EM calorimeters are for electrons and photons. (The symbol $\oplus$ means that the constant term is added in quadrature to the resolution.) λ_0 signifies interaction lengths and X_0 radiation lengths. Adapted from [30].

System	η Coverage	Energy Resolution	Thickness
CEM	$\lvert\eta\rvert < 1.1$	$13.7\%/\sqrt{E_T} \oplus 2\%$	18 X_0
PEM	$1.1 < \lvert\eta\rvert < 2.4$	$22\%/\sqrt{E_T} \oplus 2\%$	18-21 X_0
CHA	$\lvert\eta\rvert < 0.9$	$50\%/\sqrt{E_T} \oplus 3\%$	4.5 λ_0
WHA	$0.7 < \lvert\eta\rvert < 1.3$	$75\%/\sqrt{E_T} \oplus 4\%$	4.5 λ_0
PHA	$1.3 < \lvert\eta\rvert < 2.4$	$106\%/\sqrt{E_T} \oplus 4\%$	5.7 λ_0

also have the central (CHA), wall (WHA) and plug (PHA) hadronic calorimeters, covering the η regions $0 \leq |\eta| \leq 0.9$, $0.7 \leq |\eta| \leq 1.3$ and $1.3 \leq |\eta| \leq 2.4$. Figure 3.4 shows the $\eta - \phi$ segmentation of the calorimeters, and Table 3.1 summarizes the various detectors.

Central EM Calorimeter

The Central ElectroMagnetic calorimeter (CEM) is divided into 24 wedges, where each wedge covers 15° in ϕ and 0.1 in η. The CEM is a sampling calorimeter, as each wedge has 31 layers of 3.2 mm thick lead absorber alternating with 5 mm thick layers of plastic scintillator. Plastic light guides take the light from the scintillator to two phototubes per EM tower. The CEM is about 18 radiation lengths[4] thick, and for read-out purposes is segmented into 480 towers, each $(\Delta\eta = 0.1) \times (\Delta\phi = 15°)$. Near $\eta = 0$ the towers are roughly 18cm square.

Six radiation lengths into the CEM is the CES, a set of proportional strip and wire chambers. This location is approximately at the point where the electromagnetic shower deposits the maximum energy. The CES provides both z and $r - \phi$ information about the shower and has resolution of ± 2 mm in each view. The CPR (central pre-radiator) is another set of proportional chambers between the CEM and the CTC that samples early development of the EM showers caused by the material of the solenoid coil.

Plug EM Calorimeter

The plug calorimeter is a multi-wire gas (argon-ethane) proportional system, segmented into 72 5° ϕ wedges. There are 34 tube arrays interleaved with 2.7 mm thick steel absorber. The PEM is about 19 radiation lengths thick and is segmented into towers of $(\Delta\eta = 0.1) \times (\Delta\phi = 5°)$.

[4] A radiation length is the mean distance over which a high energy electron loses all but $1/e$ of its energy [5].

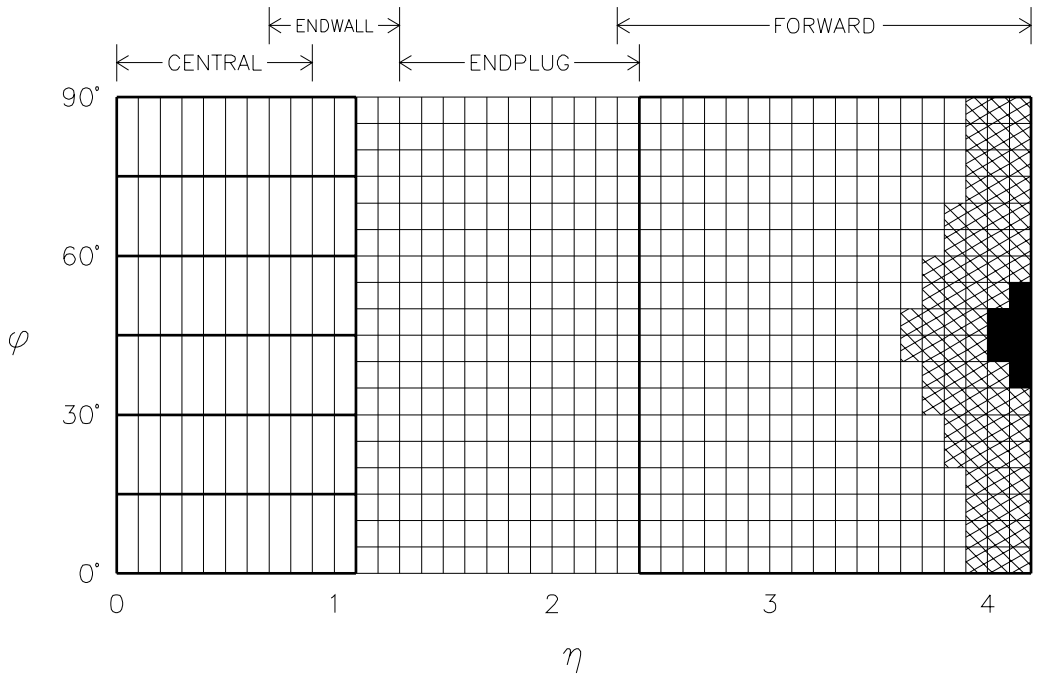

Figure 3.4: The $\eta - \phi$ segmentation of the calorimeters in the CDF detector. The central region is $|\eta| < 1.1$ where the calorimeters are segmented $(\Delta\eta = 0.1) \times (\Delta\phi = 15°)$. The Endplug region is $1.1 < |\eta| < 2.4$ and is segmented $(\Delta\eta = 0.1) \times (\Delta\phi = 5°)$. The Forward region is $2.4 < |\eta| < 4.4$ and is also segmented $(\Delta\eta = 0.1) \times (\Delta\phi = 5°)$. The hatched area in the Forward region is where there is only electromagnetic coverage, and the black area has no coverage at all (due to the presence of Tevatron steering magnets).

Just as in the CEM, the PEM has a detector placed at shower maximum. In the PEM it is a proportional system with finer granularity than the rest of the detector.

Hadronic Calorimeters

The hadronic calorimeters for each system are essentially the same in operation as the EM calorimeters in front of them. However, they use iron as the absorber instead of the lead used in the EM calorimeters.

The CHA has 32 layers of 2.5 cm thick steel absorber alternating with layers of 1 cm thick plastic scintillator and is about 4.5 interaction lengths[5] thick. Towers in the region $0.7 < |\eta| < 0.9$ are shared between WHA and CHA; a particle in this region will first pass through the CHA, then the WHA. Particles in the region $0.9 < |\eta| < 1.3$ are only measured by the WHA.

[5] Of N neutrals passing through one interaction length, all but N/e will interact with a nucleus in the material [5].

The WHA has 15 layers of 5.1 cm thick steel absorber alternating with plastic scintillator. The steel absorber layers are twice as thick in the WHA, compared to the CHA, because particles of the same E_T going into these calorimeters will have $\sqrt{2}$ times more energy in the WHA. The WHA is about 4.5 interactions lengths thick. For the remainder of this dissertation CHA refers to both the CHA and the WHA.

The PHA has 20 layers of 5.1 cm thick steel alternating with gas proportional tubes. The PHA is about 5.7 interaction lengths thick.

3.2.2 Central Muon Chambers

The CMU is directly outside the CHA, using the calorimeters as a hadron absorber (approximately 5 interaction lengths). It consists of 4 layers of drift chambers and covers the region $|\eta| < 0.6$. A muon must have $P_T >$ 1.4 GeV/c to reach the CMU. Outside the CMU is an additional 0.6 m of steel (approximately 8 interaction lengths) and then 4 more layers of drift chambers known as the CMP (Central Muon uPgrade). Approximately 84% of the detector is covered by the CMU, 63% by the CMP and 53% by both. The CMP, behind additional absorber, is very useful in reducing fake muons which are actually punch-though from energetic jets.

The CMX (Central Muon eXtension) covers the region $0.6 < |\eta| < 1.0$ and is a set of four free-standing conical arches. Each arch contains drift chambers for muon detection sandwiched between scintillators for triggering. Approximately 71% of the solid angle between $0.6 < |\eta| < 1.0$ is covered by the CMX. It is behind approximately 5 interaction lengths. The CMX has a 30° gap at the top of the detector (for the Main Ring and the solenoid refrigerator) and a 90° gap at the bottom where it intersects the floor.

Figure 3.5 shows the muon detector coverage for the central region.

3.2.3 Central Tracking Chamber

The Central Tracking Chamber (CTC) is a 3.2 meter long drift chamber with radius 31 cm $< r <$ 1325 cm, inside a 1.4 Tesla magnetic field (uniform to within $\approx$ 1%). There are 84 sampling wire layers, grouped into 5 axial and 4 stereo superlayers inside an argon-ethane-ethanol gas mixture (49.6/49.6/0.8%). Each axial superlayer contains 12 radially separated layers of sense wires, parallel to the z axis and provides $r - \phi$ information. Each stereo superlayer is rotated by $\sim 3°$ and contains 6 sense wires/layer. The direction of rotation alternates each layer and provides $r - \phi$ and z information. The axial and stereo information is combined to form 3d tracks.

The gas in the CTC is ionized as charged particles pass through it. The ionized electrons then drift to sense wires (the electric field is $\sim$ 1350 V/cm). The maximum drift time is 800 ns, shorter than the beam crossing time of 3.5 μs. The individual wire resolution is about 200 μm and

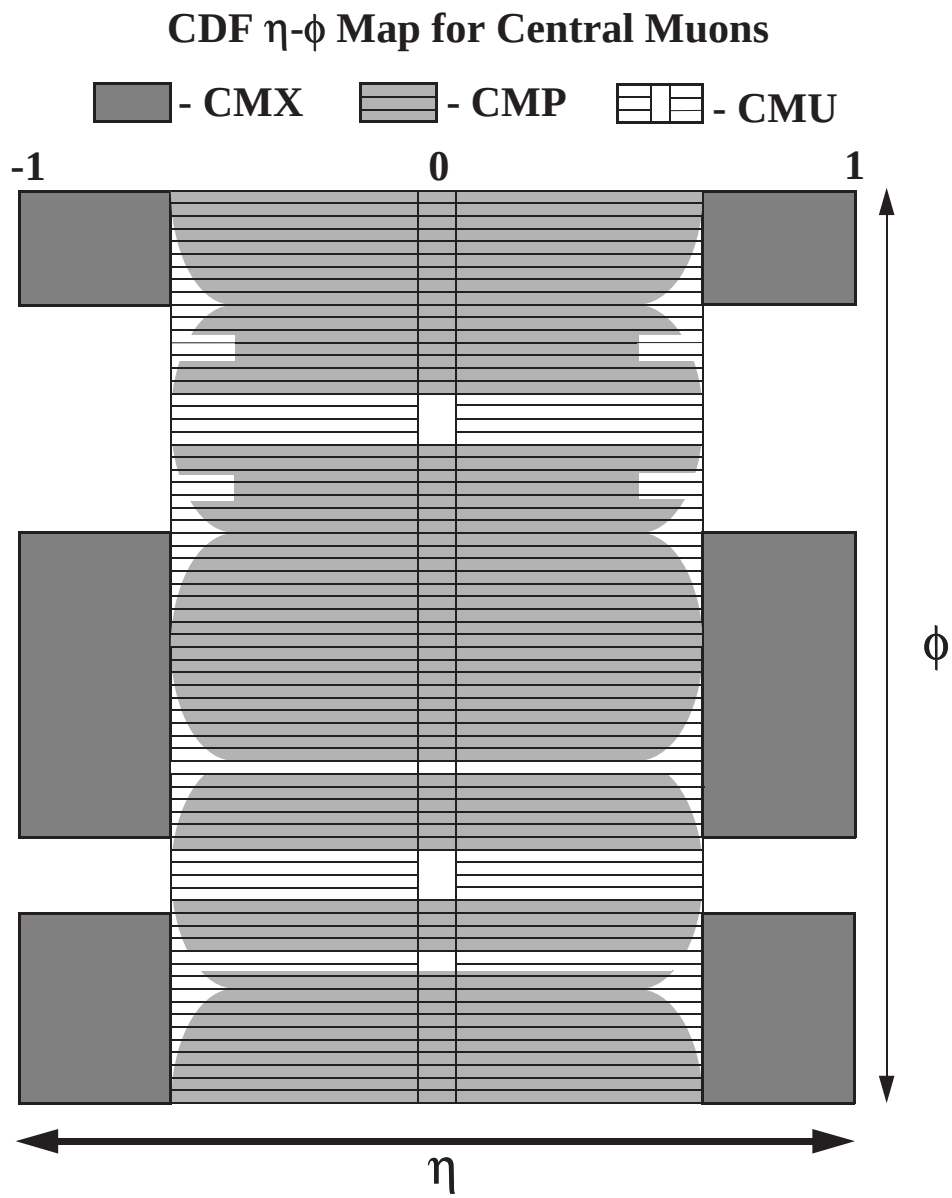

Figure 3.5: The $\eta - \phi$ muon coverage for the central region of the CDF detector. The ϕ gaps in the CMX coverage are where the CMX intersects the floor (large gap) and Tevatron components (small gap).

the two track resolution is about 5 mm. The momentum resolution is improved by factor of two by requiring that the track original in the $r-\phi$ plane of the interaction region. The beam constrained momentum resolution of the CTC is $\delta P_T/P_T = 0.002 \times P_T$ for isolated tracks where P_T is in GeV/c.

3.2.4 Vertex Detector

The VTX is a vertex time projection chamber that provides $r-\phi$ information in the region $|\eta| < 3.25$. Exact knowledge of the event vertex is important for lepton track reconstruction and for measurements of the transverse energy (E_T) and missing transverse energy ($\not{E}_T$). It surrounds the SVX detector and has an outer radius of 22 cm. The VTX is a gas chamber containing 50/50 argon/ethane bubbled through isopropyl alcohol at -7 C°. Each of the 28 modules is divided in z into two drift regions about 5 cm long, and 8 octants in ϕ. The five modules on each end have 24 sense wires in each drift region and the 18 central modules have 16 sense wires (to allow space for the SVX). All sense wires are strung azimuthally. Charged particles drift along the beam toward the center of each module to the sense wires, thus providing z information with 2 mm resolution. Each module is tilted 15° relative to its neighbors to provide rudimentary ϕ information for particles passing through two or more modules.

3.2.5 Additional Detector Components

Two other detector components are for this analysis, the Hadron TDCs and the Beam Beam Counters.

Hadron TDCs

The Hadron TDCs [31] are a set of RABBIT cards[6] that measure the time elapsed between the firing of a discriminator in the hadron calorimeter and a common stop signal. The discriminator is part of the amplifier for the signal from the phototubes used to record the light pulses from the CHA scintillator. These TDCs are installed for each central and endwall calorimeter wedge. The TDCs have a resolution of 0.5 ns and a range of 700 ns.

Luminosity Measurements: Beam Beam Counters

Luminosity at CDF is measured using beam-beam counters. These are two planes of scintillation counters covering the angular range of 0.32° to 4.47° in both the forward and backward directions ($3.24 < |\eta| < 5.88$). Hits in both counters that coincide (to within the detector resolution of about

[6] A RABBIT card is a Redundant Analog-Based Backplane InsTrumentation: a system of custom crates with custom backplanes and custom cards used as the front-end readout for CDF calorimetry.

200 ps) with the particle bunches crossing through the detector serve as both a minimum-bias trigger and the primary luminosity monitor. The rate of coincidences in these counters divided by the effective cross section of the counters gives the instantaneous luminosity. The integrated luminosity is calculated similarly using the total number of coincidences in these counters. The instantaneous luminosity of a $p\bar{p}$ collider is given by

$$\mathcal{L} = \frac{N_p N_{\bar{p}} N_B f}{4\pi\sigma^2}$$

where N_p and $N_{\bar{p}}$ are the numbers of protons and anti-protons in each bunch. N_B is the number of bunches, f ($\sim$ 50 kHz) is the revolution frequency of each bunch and $\sigma(\sim 5 \times 10^{-5})$ cm^2 is the transverse cross-sectional area of each bunch. Typical and highest instantaneous luminosities for Run IA were 0.54×10^{31} cm^{-2}s^{-1} and 0.92×10^{31} cm^{-2}s^{-1}, respectively. Similarly, for Run IB they were 1.6×10^{31} cm^{-2}s^{-1} and 2.8×10^{31} cm^{-2}s^{-1}, respectively.

3.2.6 Trigger

The pre-amplifiers on each detector component provide two outputs. The first is sent to the trigger logic to determine if the event should be saved, and the second is used to store the data until the trigger decision is made.

The Level 1 trigger is a dedicated electronics trigger that examines several subsystems (individually) to determine if the event should be saved. Depending on the exact trigger, a minimum of energy in any of the central calorimeters, a track in the tracking chamber, or hits in the muon chambers will cause the event to be passed to the next trigger level. At average Run IB instantaneous luminosities, the average Level 1 trigger rate was slightly over 1 kHz.

The Level 2 trigger, like the first trigger level, is a hardware trigger. However, it begins to combine detector subsystems. For example, a trigger might require that a track in the tracking chamber point to a set of hits in a muon chamber, or to an energy cluster in an electromagnetic calorimeter. The typical Level 2 trigger output rate was around 12 Hz, for a reduction in data of about two orders of magnitude. The Level 2 trigger also has the ability to prescale the data. At high luminosities, all the data that passes the Level 2 triggers cannot be accepted (the rate is too high). There are some rare events (such as top) that are always desirable to record. To accept as many rare events as possible while still accepting other data at a reasonable rate we prescale the Level 2 triggers. Thus, we can set a trigger to accept one of every N events that would normally pass that trigger. There are two type of prescales: static and dynamic. A static prescale is fixed during the entire course of a single data taking run (typically 8-12 hours). A dynamic prescale can be changed during the course of a run, depending on the instantaneous luminosity. Thus, a trigger can have a large prescale when the instantaneous luminosity is high and a small prescale when the

instantaneous luminosity is low. The effect of the prescales can either be treated as a decrease in the amount of total luminosity or a decrease in the efficiency of a trigger. We chose the latter.

The Level 3 trigger is a software trigger that reconstructs and examines the entire event. It was run on a series of Silicon Graphics multi-CPU Power Servers with combined processing power of approximately one billion instructions per second. As most of the data selection is done with the Level 2 triggers, the Level 3 triggers serve to remove junk events and group the events into data sets for analyses. After passing the Level 3 triggers, the data was stored on disk and then spooled to tape. The output rate is thus limited to about 5-7 Hz, partially by technology and partially by economics. This analysis used the Exotic Dilepton trigger COMBINED_EXOB_DIL, which requires two leptons (electron or muon) and has no level 2 trigger pre-requisite.

3.2.7 QFL: The CDF Detector Simulation package

QFL is a software package that simulates the CDF detector. We use it both to estimate the expected number of background events and to find the acceptance for signal events.

QFL, in general, does an excellent job of reproducing the results from test beam studies. However, it does not model the HTDCs at all, and tends to be over-efficient in the identification of leptons. Thus, we compare data from each detector subsystem to data generated using ISAJET V7.20 (our Monte Carlo generator of choice) and simulated using QFL V3.48 and apply an overall correction factor. The detector-by-detector correction factors are shown in Table 3.2. We take the combination of correction factors that will give us the largest correction (and thus the most conservative limit). For this particular analysis, this is an event with a central electron that passes the tight lepton ID cuts and two muons in the CMX that pass the loose cuts. The overall correction factor is thus 0.864 ± 0.017 ($\pm 2\%$). This is applied both to the background calculation and to the signal calculation.

Table 3.2: Summary of efficiencies for lepton IDs. The ratio IB/MC is used to calculate the needed correction factor for the Monte Carlo (since the Monte Carlo is over efficient in identifying leptons) and the uncertainty in that factor. TCE (TCM) and LCE (LCM) refer to Tight and Loose Central Electron (Muon) respectively. Adapted from Ref. [32].

	Eff. (MC)	Eff. (IA)	Eff. (IB)	IB/MC
TCE	0.867 ± 0.004	0.825 ± 0.014	0.819 ± 0.008 (0.92%)	0.945 ± 0.010 (1.04%)
LCE	0.890 ± 0.003	0.850 ± 0.013	0.852 ± 0.007 (0.79%)	0.957 ± 0.008 (0.88%)
PEM	0.924 ± 0.004	0.890 ± 0.012	0.920 ± 0.007 (0.76%)	0.996 ± 0.009 (0.88%)
TCM	0.978 ± 0.003	0.903 ± 0.025	0.929 ± 0.007 (0.75%)	0.950 ± 0.008 (0.81%)
LCM	0.978 ± 0.003	0.903 ± 0.025	0.937 ± 0.006 (0.64%)	0.958 ± 0.007 (0.71%)
CMX	0.972 ± 0.005	0.940 ± 0.029	0.929 ± 0.010 (1.08%)	0.956 ± 0.011 (1.19%)
CMI	0.977 ± 0.004	0.925 ± 0.042	0.942 ± 0.011 (1.17%)	0.964 ± 0.012 (1.24%)

Chapter 4

Data Analysis

The data analysis for this dissertation can be broken down into two main sections: the identification of events with three good leptons and the rejection of background events. The event selection is done in several steps, with more rigorous identification requirements applied at each step. The background is rejected by a series of cuts, each designed to remove one or more specific type of event.

4.1 Bank Creation

CDF stores events in a series of data structure called banks. For example, an ELES bank is an electron candidate, a PHOB bank is a photon candidate, and a CMUO bank is a central muon candidate.

Before we can begin to determine if an object is an electron or a jet or a muon, it must have been identified by the off-line reconstruction software as having met certain criterion. For this analysis, the most important object banks are the ELES, CMUO and CMIO banks. The object banks contain kinematic information about the object (such as P_T, η or ϕ) as well as detector information (such as the energy deposited in the EM or Hadronic calorimeters, or the VTX occupancy). We also use information from the TRKS (tracking information), VTVZ (event vertex information) banks and METS (missing energy information). I will describe each in turn.

4.1.1 ELES banks

The energy of an electron candidate is reconstructed from the sum of the energies measured in a cluster of towers in the CEM. For each tower, the geometric mean of the charge from the two

phototubes, one on each side in azimuth, is used as the measure of the tower energy[1] to construct clusters of energy. Seed towers are chosen for an event as the towers with the largest transverse energy. The two towers on either side in the z direction ("shoulder towers") are included in the cluster, unless this would require crossing the boundary at $\eta = 0$[2], in which case the cluster consists of just two towers. The energy of the electron is taken as the sum of the electromagnetic energies in the cluster of seed and shoulder towers. Individual clusters continue to be identified until no towers above the seed tower threshold of 5 GeV remain. There is one ELES bank per cluster.

4.1.2 CMUO banks

A muon is reconstructed using the drift chambers in the CMU, CMP and CMX. The location of the muon in the chamber is determined using the drift chamber time-to-distance relationship in the ϕ direction and the charge division in the z direction. To be considered a muon, there must be at least three separate layers with hits that are aligned within the detector resolution (250 μm in r and 1.2 mm in z) in both the $r - \phi$ and $r - z$ planes. These segments are merged to form a three dimensional stub. This stub is then matched with a track extrapolated from the CTC. The extrapolation accounts for multiple scattering and the effects of the magnetic field. There is one CMUO bank per muon candidate.

4.1.3 CMIO banks

As seen in Section 3.2.2, only 53% of the central region of the detector is covered by both the CMU and the CMP, and some of the detector is covered by neither. Thus, muons can travel through the detector and not pass through a muon chamber. To increase the chances of detecting all muons, we have the Central Minimum Ionizing Object (CMIO) bank. To be considered a CMIO, a track must pass through a region of the detector where the track identification is good and extrapolate to an energy deposit in the calorimeters. CMIOs can be in the region $|\eta| < 1.2$, although they are generally only used to $|\eta| < 1.0$. CMIOs do not cause triggers. There is one CMIO bank per candidate.

4.1.4 TRKS banks

The TRKS bank contains a reconstructed track linked across several detectors (SVX, VTX and CTC). It contains information about the track and the quality of the track fit. There is one TRKS bank per track, which can be linked to CMUO, CMIO or ELES banks.

[1] The geometric mean is used to reduce the dependence of the energy measurement on local shower position due to light attenuation in the scintillator.

[2] There is a crack at $\eta = 0$ where the two halves of the detector meet.

4.1.5 VTVZ banks

The VTVZ bank contains VTX and CTC information on primary vertices, especially the z vertex for the event. It may or may not include information about the beam position. There may be several vertices per bank, but only one bank per event. For each vertex, the VTVX bank lists the x, y, and z position as well as a quality index. The quality index is a function of the number of tracks pointing at the vertex and the accuracy of the measurement of the vertex. We accept vertices with a quality index of 5 or greater.

4.1.6 METS banks

CDF calorimetery does not cover the full 4π solid angle; in addition to not being hermitic there must be room for the beam pipe and steering magnets for the Tevatron. Because of this, we cannot measure the total energy of an event, as some particles can escape down the beam pipe. Such a particle would have momentum transverse to the beam less than 3.5% of its momentum along the beam direction, but substantial momentum along the direction of the beam. Thus, we cannot measure the total momentum of an event. However, the transverse momentum carried by such particles is small. Thus, the sum of the momentum transverse to the beam direction of the particles in an event must be zero (within detector resolution), and the vector sum of the transverse energy of the interacting particles must also be zero. The missing transverse energy ($\not\!\!E_T$) is defined to be the negative of the vector sum of transverse energy for all towers over threshold with $|\eta| < 3.6$:

$$\vec{\not\!\!E_T} = -\sum_i \vec{E_T^i},$$

where E_T^i is the energy in the ith tower. Since the different calorimeter subsystems use different technologies (and thus have different sensitivities), we require different thresholds in each detector: 100 MeV in the CEM, CHA and WHA, 300 MeV in the PEM, 500 MeV in the PHA and FEM and 800 MeV in the FHA. Muons are not stopped by the calorimeter and so their energy is not included in this sum. To correct for muons, we vectorially subtract their momentum from the $\not\!\!E_T$. The METS bank contains the missing transverse energy information, which we use for the $\not\!\!E_T$ cut. There is one METS bank per event.

4.2 Event selection

To select the three lepton[3] events for this analysis, I first require events with two leptons passing the Level 3 Exotic Dilepton trigger (COMBINED_EXOB_DIL) which produce the XDLB_5P PAD

[3]Recall that for this analysis *lepton* refers to electrons or muons.

tapes. Next, I require these events to have a third lepton. The data set, some 17,000 events, is now small enough to fit on disk. I apply tighter cuts, further reducing the data set. The remaining 247 events are the good trilepton candidate events.

4.2.1 Dilepton Selection (Skimming)

As CDF collects data, the data passes though the Level 3 trigger. During Run 1, the Level 3 trigger served mainly as a method to create data sets with certain requirements. One of those sets was the Exotic Dilepton data set XDLB_5P, a series of 56 data tapes. To be included in this data set, an event is required to have one central lepton ($|\eta| < 1$) with $P_T > 8$ GeV/c and a second lepton anywhere in the central or plug (for electrons only) regions of the detector with $P_T > 3$ GeV/c. We search this data set for events that met the following criteria (determined from test beam data where known particles of known energies were sent through the various detector subcomponents):

- At least one lepton, either electron or muon, in the CEM or CMU/P that met the tight requirements listed in Table 4.1 (electron) or Table 4.2 (muon).
- At least one additional electron or muon in the CEM, PEM, CMU/P or CMX (or a CMIO) that met the loose requirements in Table 4.1 (electron) or Table 4.2 (muon).

The requirements are fully explained below. After this selection, we are left with 407,742 events.

Electron identification cuts

These cuts are used to identify electrons in either the CEM or the PEM. Some cuts are applied to electrons in either detector and some are applied only to either the CEM or the PEM. The differences are mainly due to a lack of complete tracking for PEM electrons. The cut values (expect for the E_T, P_T and Isolation cuts) are determined from test beam results.

P_T is the transverse momentum of the electron measured by the CTC. We require the tight electron have $P_T \geq 6.0$ GeV/c and the loose electron have $P_T \geq 2.8$ GeV/c. This cut is applied only to CEM electrons as electrons entering the PEM will not travel through the entire CTC and an accurate momentum measurement cannot be made.

E_T is the transverse energy deposited in the EM calorimeter, clustered as described in Section 4.1.1. We require at least 8 GeV $E_T$for the tight electron (which must be in the CEM), and 4.0 GeV for the loose lepton.

E/p is the ratio of the electron's energy to its momentum and must be less than 2.0. Requiring an electron to have momentum roughly the same as its energy (and thus be associated with

Table 4.1: Skimming selection criteria for CEM and PEM electrons. A dash indicates that cut was not applicable for that type object.

Lepton class	Tight	Loose	
Cut variables	CEM	CEM	PEM
p_T (GeV/c)	≥ 6.0	≥ 2.8	—
E_T (GeV)	≥ 8.0	≥ 4.0	≥ 4.0
E/p	≤ 2.0	≤ 2.0	—
HAD/EM	≤ 0.05	$\leq 0.055 + 0.045 \times \frac{E}{100}$	≤ 0.1
L_{SHR}	≤ 0.2	≤ 0.2	—
$\|\Delta x\|$ (cm)	≤ 3.0	≤ 3.0	—
$\|\Delta z\|$ (cm)	≤ 5.0	≤ 5.0	—
χ^2_{strip}	≤ 10.0	≤ 15.0	—
$\chi^2_{3\times 3}$	—	—	≤ 3.0
VTX occupancy	—	—	≥ 0.5

Table 4.2: Skimming selection criteria for CMU/P, CMX and CMIO muons. A dash indicates that cut was not applicable for that type object. d_0 raw is the non-beam constrained impact parameter.

Lepton class	Tight	Loose	
Cut variables	CMU/P	CMU/P or CMX	CMI
p_T (GeV/c)	≥ 7.5	≥ 2.8	≥ 10
EM (GeV)	≤ 2.0	≤ 2.0	≤ 2.0
Had (GeV)	≤ 6.0	≤ 6.0	≤ 6.0
d_0 raw (cm)	≤ 0.5	≤ 0.8	≤ 0.8
CMU Matching	$\|\Delta x\| \leq 2$ cm or $\chi^2_{CTC} \leq 9$	$\|\Delta x\| \leq 2$ cm or $\chi^2_{CTC} \leq 9$	—
CMP Matching	$\|\Delta x\| \leq 5$ cm or $\chi^2_{CTC} \leq 9$	$\|\Delta x\| \leq 5$ cm or $\chi^2_{CTC} \leq 9$	—
CMX Matching	—	$\|\Delta x\| \leq 5$ cm or $\chi^2_{CTC} \leq 9$	—

a charged track) reduces the number of photons from π^0 decays. E/P should peak at roughly 1.1 and provides a measure of the material in the CTC. It is not applied to PEM electrons.

Had/EM is the ratio of the energy deposited in the hadronic calorimeter to the energy deposited in the EM calorimeter. Almost all of the energy will be deposited in the EM calorimeter so we require Had/Em ≤ 0.05 for a tight electron, $\leq 0.055 + 0.045 \times \frac{E}{100}$ for a loose CEM and ≤ 0.1 for a loose PEM. The sliding cut is used mainly for historical reasons[4] but is looser than the constant cut.

L_{SHR} is the transverse profile of the electromagnetic shower. It allows a comparison of the lateral sharing of energy in the calorimeter towers of an electron cluster to electron shower shapes from test beam data. The variable L_{SHR} is defined to be

$$L_{SHR} \equiv 0.14 \sum_i \frac{E_i^{\text{adj}} - E_i^{\text{prob}}}{\sqrt{0.14^2 E + (\Delta E_i^{\text{prob}})^2}}$$

where E_i^{adj} is the measured energy (in GeV) in a tower adjacent to the seed tower, E_i^{prob} is the expected energy (in GeV) in the adjacent tower, $0.14\sqrt{E}$ (in GeV) is the error on the energy measurement, and ΔE_i^{prob} the error on the energy estimate. E_i^{prob} is calculated using a parameterization from test beam data. It is not applied to PEM electrons.

$|\Delta x|$ **and** $|\Delta z|$ are matching cuts. An alignment corrected CTC track is extrapolated to the CES and compared to the shower position from the CES. $|\Delta x|$ is the matching in the $r - \phi$ plane and is required to be less than 3.0 cm. $|\Delta z|$ is the matching in the z direction and is required to be less than 5 cm. This cut is not applied to PEM candidates.

χ^2_{strip} is the comparison the CES pulse height to test beam data for each of the 11 strips (per CEM chamber) in z. We only cut in z as bremsstrahlung tends to broaden the distribution in $r - \phi$. It is not applied to PEM candidates.

$\chi^2_{3\times 3}$ is a fit of the lateral sharing of energy in the three towers in η by the three towers in ϕ around the electron cluster's center to the shape expected from test beam data [33]. It is applied only to PEM electrons (in lieu of the L_{SHR} cut).

VTX occupancy is used to remove photons from the PEM candidates. It is the ratio of layers in the VTX where the electron deposits charge to the number of layers where the electron

[4]The sliding Had/EM cut was originally designed for Z' searches, where the electrons were expected to be quite energetic. In our search the E_T of the electron ranges from 5 Gev to 100 GeV. The constant term dominates for low energy electrons.

Table 4.3: Number of CEM and PEM electrons left after each lepton identification cut. See Table 4.1 and the text for an explanation of each cut. A dash indicates that cut is not applied. If an electron passed the tight cuts, it is not counted in the loose column.

Lepton class	Tight	Loose	
Cut variables	CEM	CEM	PEM
Before Cuts	366,550	356,850	53,257
p_T	274,670	314,850	—
E_T	241,900	314,790	53,222
E/p	235,810	298,520	—
HAD/EM	230,020	290,250	51,572
L_{SHR}	226,540	277,800	—
$\|\Delta x\|$	225,850	275,500	—
$\|\Delta z\|$	225,410	274,360	—
χ^2_{strip}	222,820	273,660	—
$\chi^2_{3\times3}$	—	—	38,724
VTX occupancy	—	—	36,815

should deposit charge based on the electron's trajectory. We require the occupancy to be $\geq$ 0.5 to ensure the presence of a charged track. This cut is only applied to PEM candidates.

Figures 4.1-4.5 show distributions for each of the cut variables before and after the third lepton requirement and indicate the cut values for both the skimming and analysis passes. For these plots we sort the electron by P_T. The electrons with the highest P_T per event are plotted separately (as they must pass more stringent cuts than the lower P_T electrons). Table 4.3 lists the number of electron candidates left after each cut for CEM (tight and loose) and PEM electrons. Since we have only required the presence of two leptons, we should have many Z^0, J/ψ and Υ events in our sample. Figure 4.6 shows the two-body mass for events with an opposite-sign electron pair.

Muon Identification Cuts

These cuts are used to identify muons in the CMU, CMP, CMX or CMIO. Some of the cuts are not applied to the CMIOs, as they correspond to muons with no hits in the muon chambers. As with the electron ID cuts, the values for the cuts are determined using test beam data.

P_T is the momentum of the muon as measured by the CTC. We require a tight muon (CMU or CMP) to have $P_T \geq 7.5$, a loose CMU, CMP or CMX muon to have $P_T \geq 2.8$ and loose CMIO muon to have $P_T \geq 10$ GeV/c[5].

[5]The CMIO cut is 10 GeV/c since that bank is created only for tracks with P_T above 10 GeV/c.

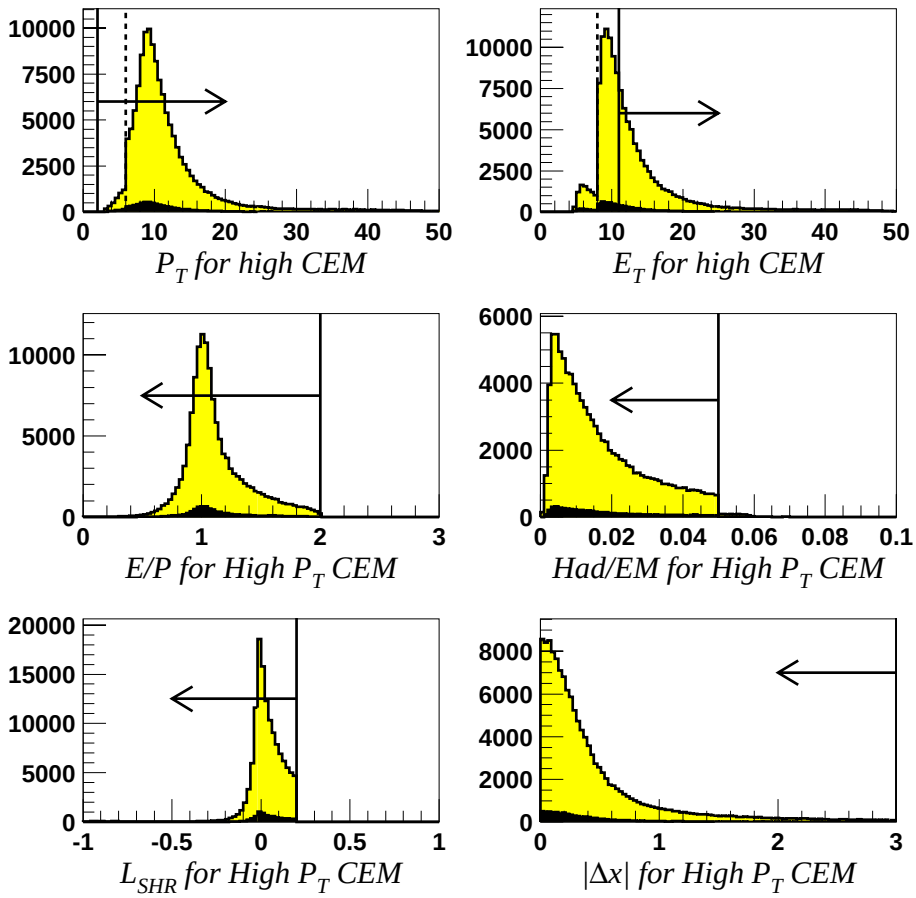

Figure 4.1: Distributions for CEM electrons which pass the tight ID cuts. The light histogram is the distribution after the skimming cuts have been applied to two leptons (one tight and one loose), and the dark histograms is after the third lepton requirement has been imposed. The dashed lines indicate the skimming cut value and the solid line indicates the analysis cut value. In histograms with only one line either the cut value was the same for the skim and analysis or the cut was not applied during the skim. The arrows indicate the accepted values. The events to the left of the P_T and E_T cuts are events where a muon passed the tight cuts and an electron passed the loose cuts. The P_T cut is loosened since the more appropriate cut for electrons is an E_T cut. For this and the following plots P_T is measured in GeV/c, E_T/sp and Isolation are measured in GeV, and Δx and Δz are measured in cm.

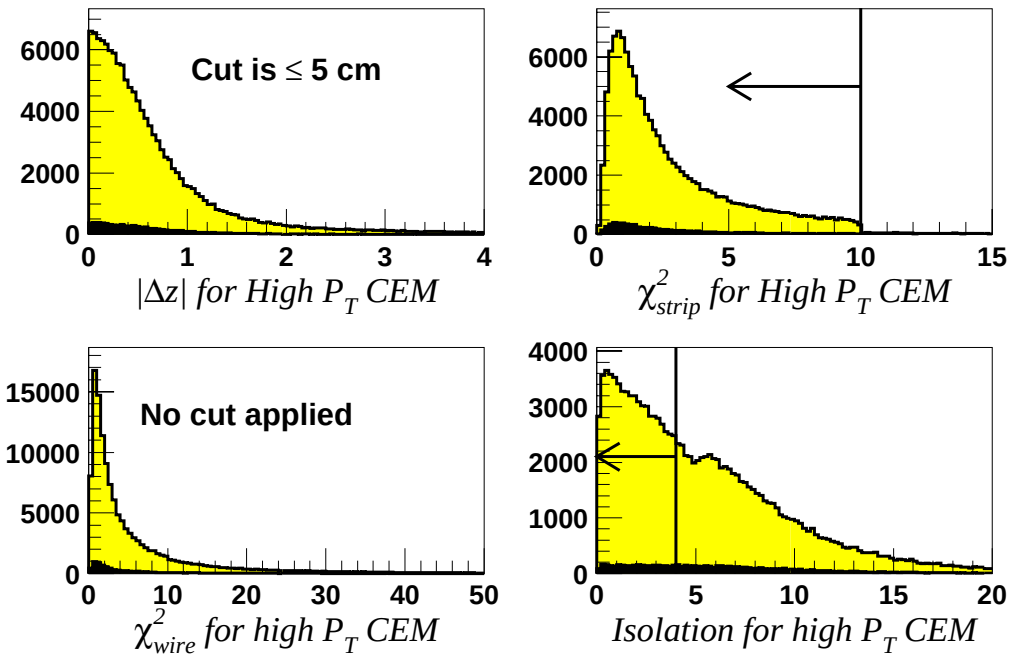

Figure 4.2: Distributions for high P_T CEM electrons which pass the tight ID cuts. The light histogram is the distribution after the skimming cuts have been applied to two leptons (one tight and one loose), and the dark histograms is after the third lepton requirement has been imposed. The dashed lines indicate the skimming cut value and the solid line indicates the analysis cut value. In histograms with only one line either the cut value was the same for the skim and analysis or the cut was not applied during the skim. The arrows indicate the accepted values. The χ^2_{wire} is shown only for informational purposes. Isolation is defined below.

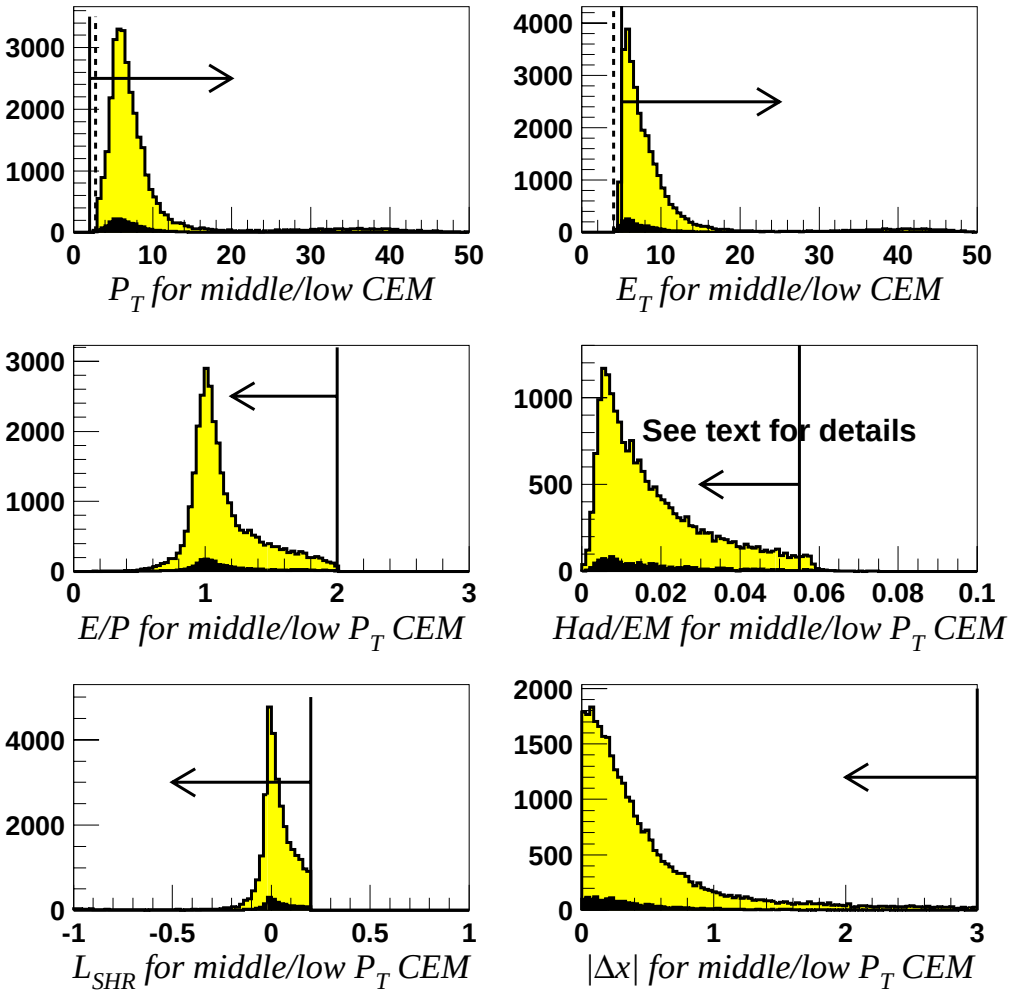

Figure 4.3: Distributions for CEM electrons which pass the loose ID cuts. Electrons which pass the tight ID cuts are not included in this plot. The light histogram is the distribution after the skimming cuts have been applied to two leptons (one tight and one loose), and the dark histograms is after the third lepton requirement has been imposed. The dashed lines indicate the skimming cut value and the solid line indicates the analysis cut value. In histograms with only one line either the cut value was the same for the skim and analysis or the cut was not applied during the skim. The arrows indicate the accepted values. The Had/EM cut is a sliding cut; see the text for details.

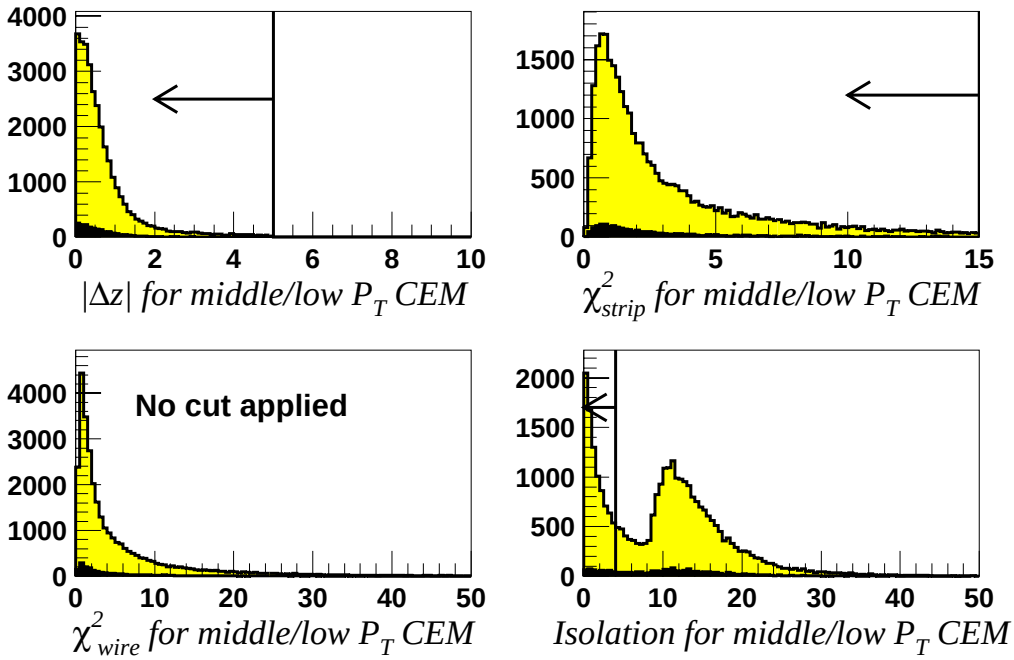

Figure 4.4: Distributions for CEM electrons which pass the loose ID cuts. Electrons which pass the tight ID cuts are not included in this plot. The light histogram is the distribution after the skimming cuts have been applied to two leptons (one tight and one loose), and the dark histograms is after the third lepton requirement has been imposed. The dashed lines indicate the skimming cut value and the solid line indicates the analysis cut value. In histograms with only one line either the cut value was the same for the skim and analysis or the cut was not applied during the skim. The arrows indicate the accepted values. The χ^2_{wire} is shown only for informational purposes. Isolation is defined below.

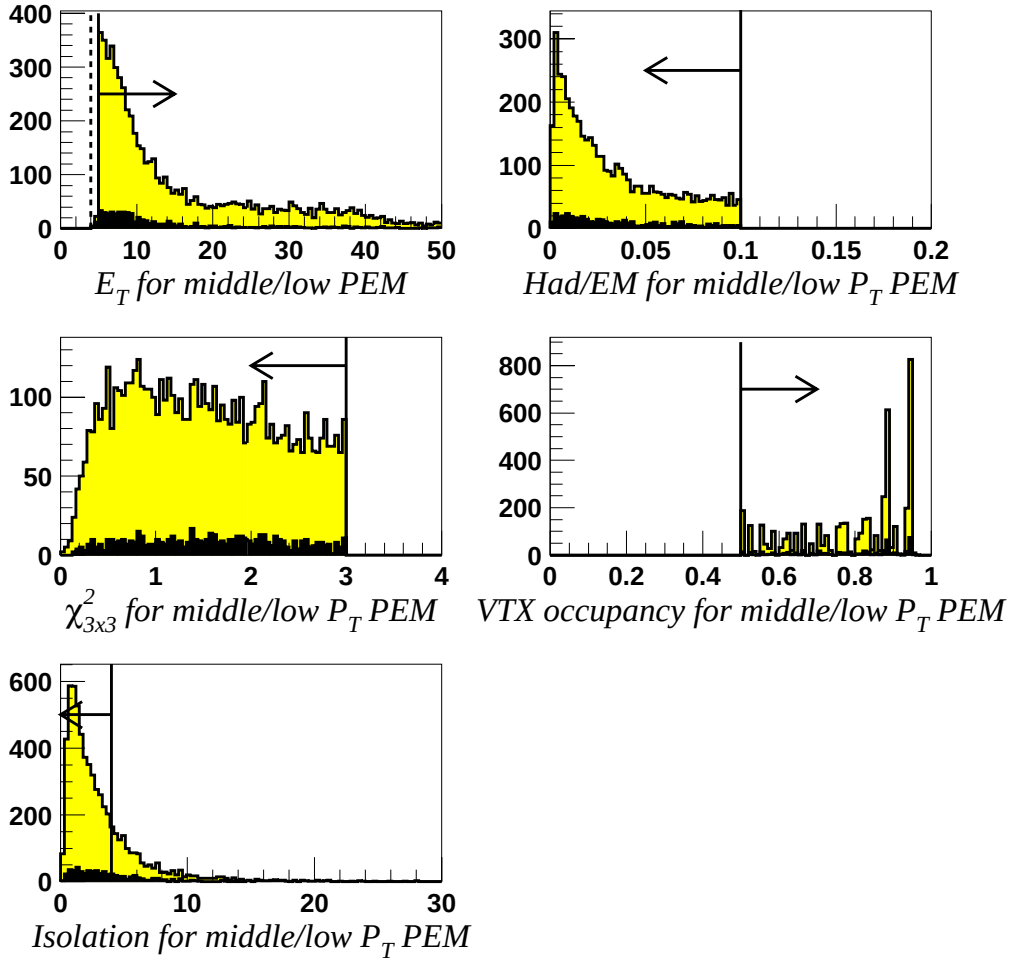

Figure 4.5: Distributions for PEM electrons which pass the loose ID cuts. The light histogram is the distribution after the skimming cuts have been applied to two leptons (one tight and one loose), and the dark histograms is after the third lepton requirement has been imposed. The dashed lines indicate the skimming cut value and the solid line indicates the analysis cut value. In histograms with only one line either the cut value was the same for the skim and analysis or the cut was not applied during the skim. The arrows indicate the accepted values. Isolation is defined below.

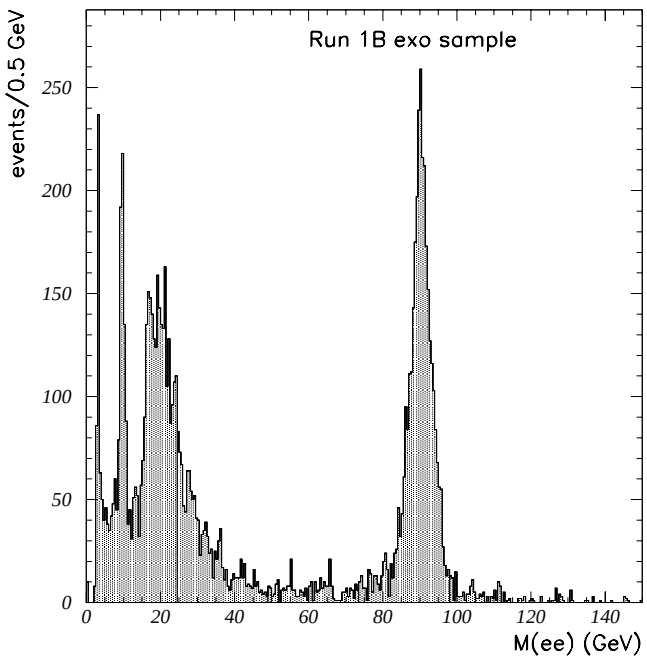

Figure 4.6: The two body mass for opposite sign electron pairs after loose identification cuts are applied. Peaks at the J/ψ, Υ and Z^0 masses can clearly be seen. The peak at 20 GeV/c^2 is Drell-Yan; it is due to trigger turn-on effects.

EM is the energy deposited in the EM calorimeter. A muon should not deposit substantial amounts of energy in any calorimeter, as the calorimeters do not contain enough material to stop a muon with momentum above 1.4 GeV/c. We require the energy in the EM calorimeter to be less than 2.0 GeV for all muon candidates.

Had is the energy deposited in the hadronic calorimeters. The hadronic calorimeters contain more absorber material than do the EM calorimeters so a muon has a higher probability of depositing some energy. Therefore, we relax this cut to 6.0 Gev for all muon candidates.

d_0 **raw** is the impact parameter and requires the muon to originate from near the nominal interaction region. This cut is on the uncorrected impact parameter and requires the muon to have $d_0 \leq 0.5$ cm (tight CMU or CMP) or ≤ 0.8 cm (loose CMU, CMP, CMX or CMIO). This cut helps to reduce the number of cosmic rays in the sample.

Matching requires good alignment between the extrapolation of the CTC track and the muon stub. We require that either the $r-\phi$ distance between the extrapolation ($|\Delta x|$) be less than a certain value OR the χ^2_x of a fit from the CTC track to the muon stub be less than 9.0. The

Table 4.4: Number of CMU/P, CMX and CMIO muons left after each lepton identification cut. See Table 4.2 and the text for an explanation of each cut. A dash indicates that cut was not applied. Muons which pass the tight ID cuts are not counted as passing the loose cuts.

Lepton class	Tight	Loose		
Cut variables	CMU/P	CMU/P	CMX	CMIO
Before cuts	449,240	445,260	88,947	212,430
p_T	223,220	417,810	71,262	212,430
EM	214,260	396,170	63,372	57,150
HAD	212,340	392,230	62,722	51,760
d_0 raw	210,170	391,990	62,647	51,150
Matching	209,460	385,720	59,880	—

value of the $|\Delta x|$ cut depends on the detector: 2.0 cm for CMU muons and 5.0 cm for CMP or CMX muons. This cut is not applied to CMIO muons as they do not correspond to muons stubs.

Figures 4.7-4.13 show distributions for each of the cut variables before and after the third lepton requirement and indicate the cut values for both the skimming and analysis passes. Table 4.4 lists the number of muon candidates left after each cut for CMU/P (tight and loose) and CMX and CMIO muons. As with the electrons, we should have substantial numbers of Z^0, J/ψ and Υ events in our sample. Figure 4.14 shows the two-body mass for events with an opposite-sign muon pair, and Figure 4.15 shows the detail in the J/ψ mass region.

4.2.2 Trilepton Selection (Skimming)

We next require events have a third lepton. This electron (muon) was required to meet the loose criteria in Table 4.1 (4.2). After this selection we are left with 17,087 events. This size sample fits quite nicely on disk and can be examined with analysis code in about an hour.

4.2.3 Trilepton Selection (Analysis)

To further improve the quality of our leptons, we impose the tighter identification cuts listed in Tables 4.5 and 4.6 for electrons and muons. These cuts are identical to the cuts applied during the loose selection. However, some of the values are changed, and a few cuts are added. I describe them below. We use two sets of cuts so we can change the analysis cuts and re-analyze the data without having to re-examine the entire data set. After these cuts are applied, we are left with 247 events.

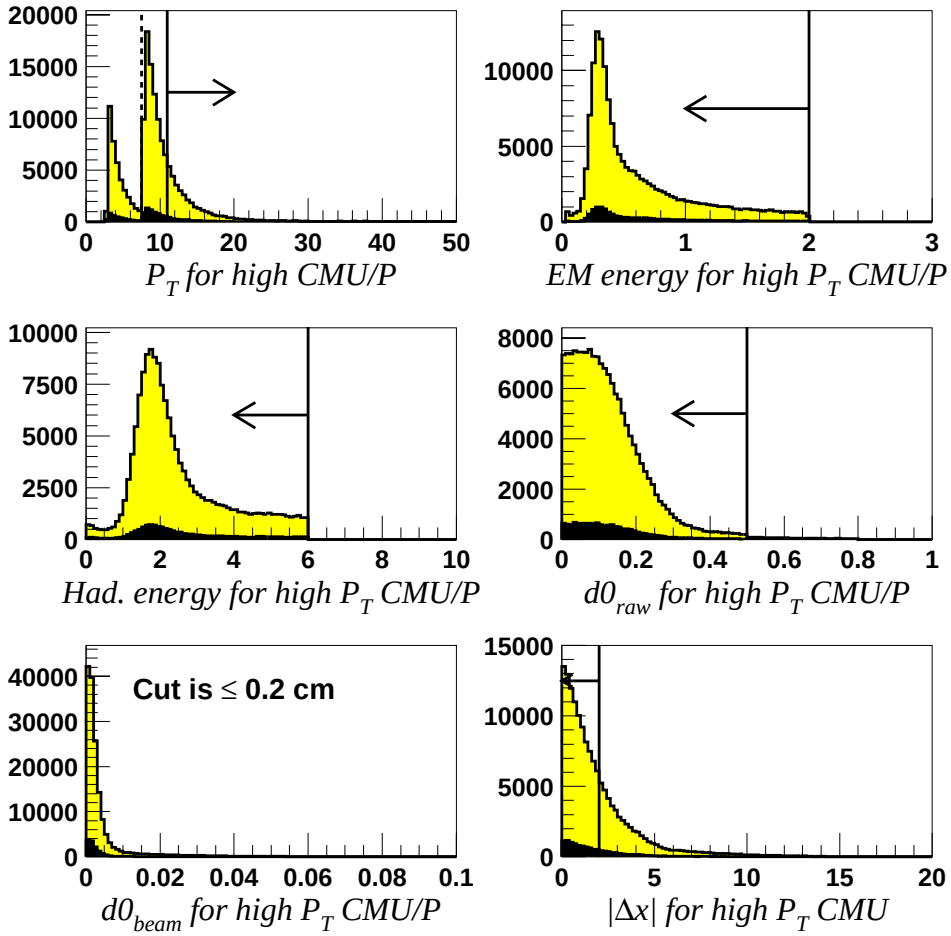

Figure 4.7: Distributions for CMU/P muons which pass the tight ID cuts. The light histogram is the distribution after the skimming cuts have been applied to two leptons (one tight and one loose), and the dark histograms is after the third lepton requirement has been imposed. The dashed lines indicate the skimming cut value and the solid line indicates the analysis cut value. In histograms with only one line either the cut value was the same for the skim and analysis or the cut was not applied during the skim. The arrows indicate the accepted values. Recall the $|\Delta x|$ cut is ORed with the CTC χ^2 cut. The small peak in the P_T distribution is from events where an electron passed the tight ID cuts and a muon passed the loose ID cuts. The peaks in the EM and Had energy plots are the Landau curves for single muons passing through these detectors.

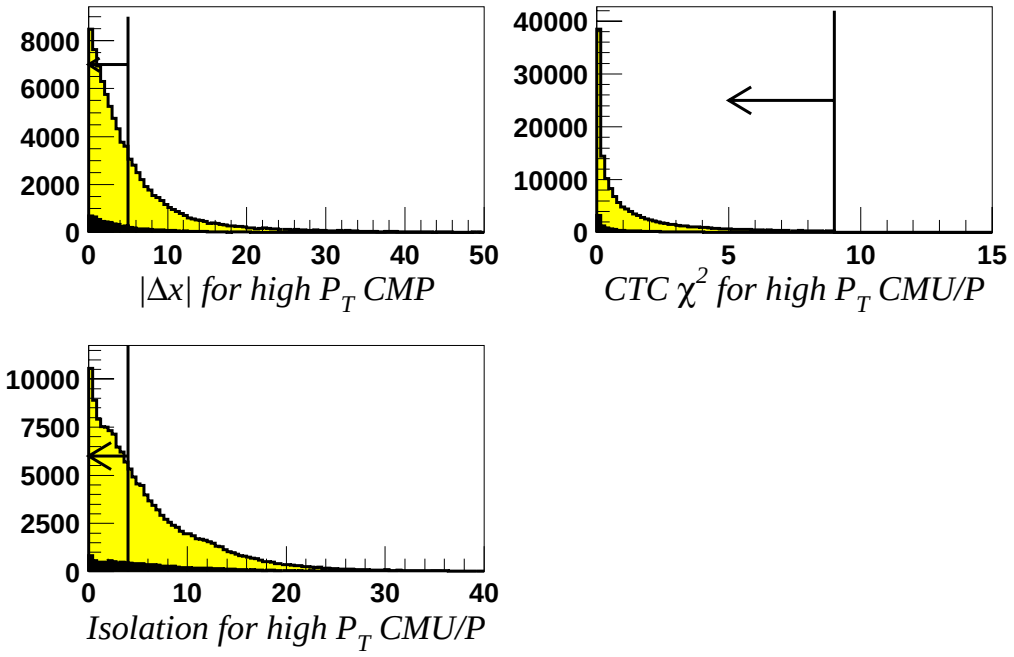

Figure 4.8: Distributions for CMU/P muons which pass the tight ID cuts. The light histogram is the distribution after the skimming cuts have been applied to two leptons (one tight and one loose), and the dark histograms is after the third lepton requirement has been imposed. The dashed lines indicate the skimming cut value and the solid line indicates the analysis cut value. In histograms with only one line either the cut value was the same for the skim and analysis or the cut was not applied during the skim. The arrows indicate the accepted values. Recall the $|\Delta x|$ cut is ORed with the CTC χ^2 cut.

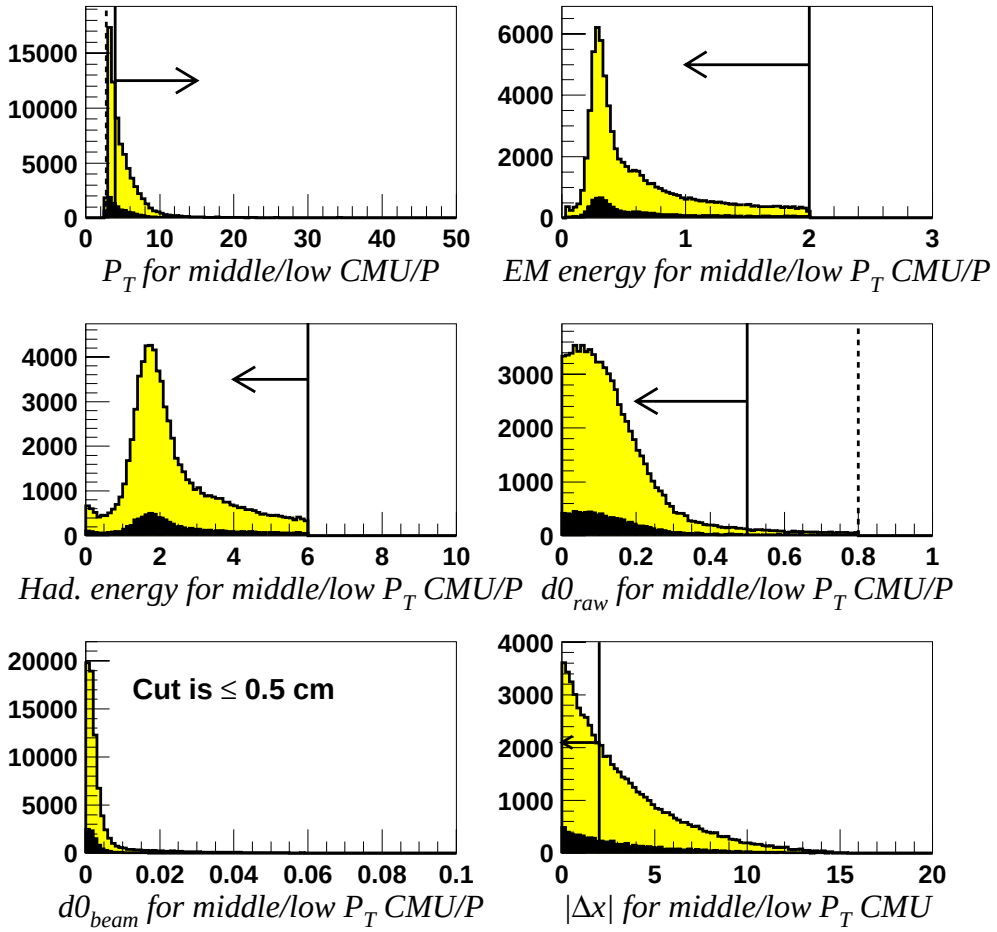

Figure 4.9: Distributions for CMU/P muons which pass the loose ID cuts. Muons which pass the tight ID cuts are not plotted here. The light histogram is the distribution after the skimming cuts have been applied to two leptons (one tight and one loose), and the dark histograms is after the third lepton requirement has been imposed. The dashed lines indicate the skimming cut value and the solid line indicates the analysis cut value. In histograms with only one line either the cut value was the same for the skim and analysis or the cut was not applied during the skim. The arrows indicate the accepted values. Recall the $|\Delta x|$ cut is ORed with the CTC χ^2 cut. The peaks in the EM and Had energy plots are the Landau curves for single muons passing through these detectors.

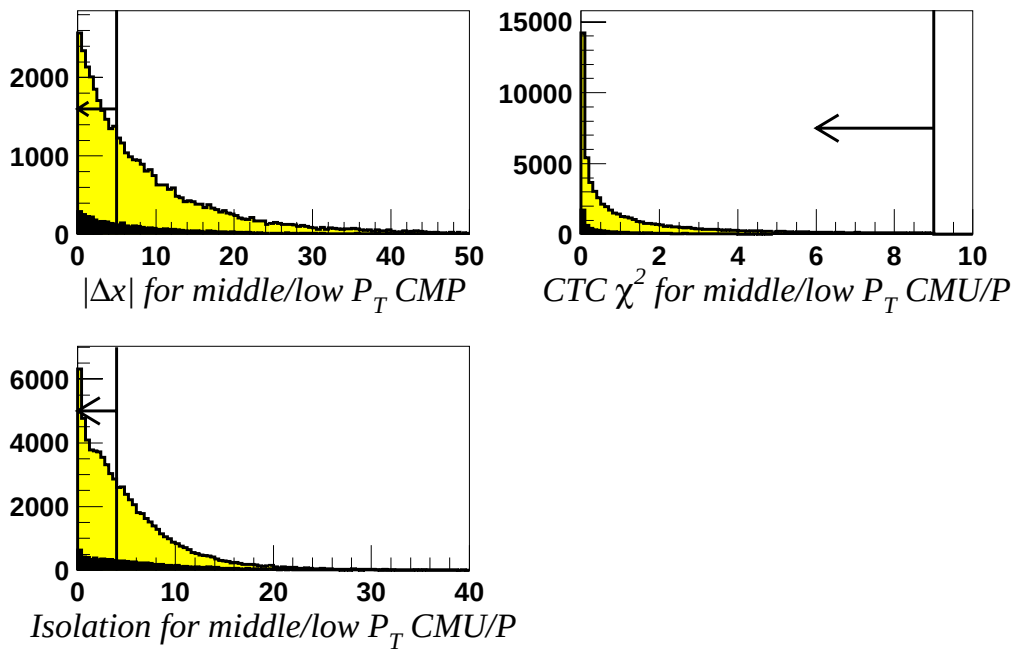

Figure 4.10: Distributions for CMU/P muons which pass the loose ID cuts. Muons which pass the tight ID cuts are not plotted here. The light histogram is the distribution after the skimming cuts have been applied to two leptons (one tight and one loose), and the dark histograms is after the third lepton requirement has been imposed. The dashed lines indicate the skimming cut value and the solid line indicates the analysis cut value. In histograms with only one line either the cut value was the same for the skim and analysis or the cut was not applied during the skim. The arrows indicate the accepted values. Recall the $|\Delta x|$ cut is ORed with the CTC χ^2 cut.

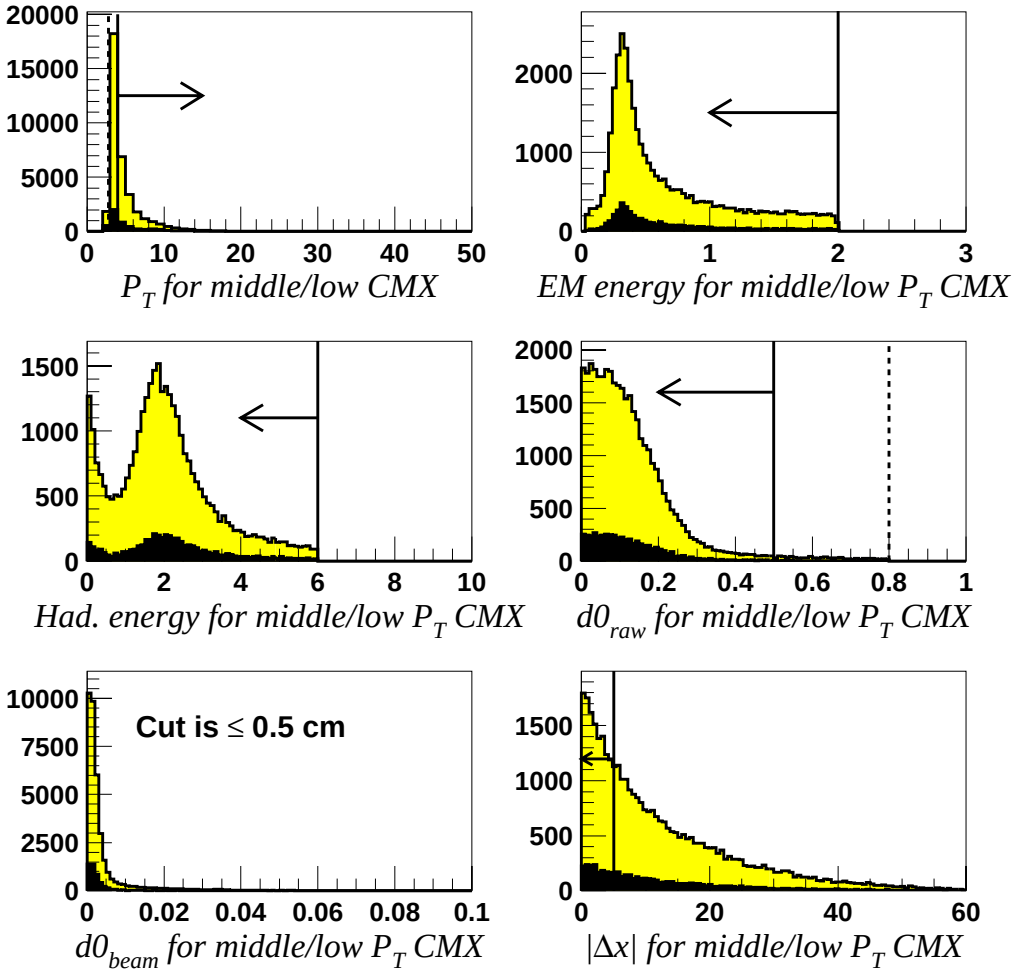

Figure 4.11: Distributions for CMX muons which pass the loose ID cuts. The light histogram is the distribution after the skimming cuts have been applied to two leptons (one tight and one loose), and the dark histograms is after the third lepton requirement has been imposed. The dashed lines indicate the skimming cut value and the solid line indicates the analysis cut value. In histograms with only one line either the cut value was the same for the skim and analysis or the cut was not applied during the skim. The arrows indicate the accepted values. Recall the $|\Delta x|$ cut is ORed with the CTC χ^2 cut. The peaks in the EM and Had energy plots are the Landau curves for single muons passing through these detectors.

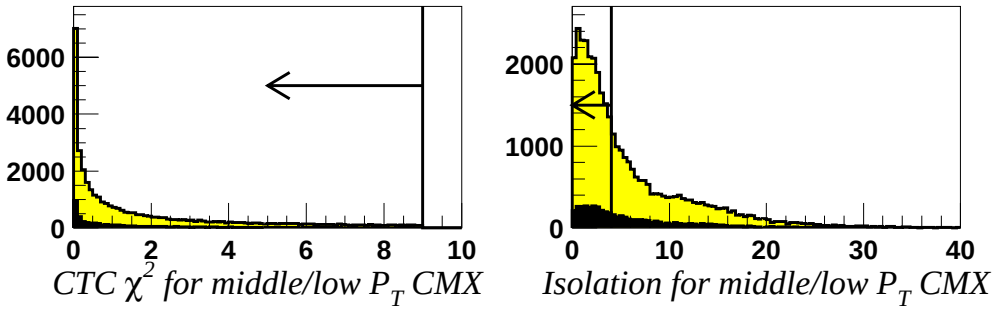

Figure 4.12: Distributions for CMX muons which pass the loose ID cuts. The light histogram is the distribution after the skimming cuts have been applied to two leptons, and the dark histograms is after the third lepton requirement has been imposed. The dashed lines indicate the skimming cut value and the solid line indicates the analysis cut value. In histograms with only one line either the cut value was the same for the skim and analysis or the cut was not applied during the skim. The arrows indicate the accepted values. Recall the $|\Delta x|$ cut is ORed with the CTC χ^2 cut.

Table 4.5: Analysis lepton selection cuts for CEM and PEM electrons.

Lepton class	Tight	Loose	
Cut variables	CEM	CEM	PEM
p_T (GeV/c)	≥ 2	≥ 2	—
E_T (GeV)	≥ 11	≥ 5	≥ 5
E/p	≤ 2	≤ 2	—
HAD/EM	≤ 0.05	$\leq 0.055 + 0.045 \times \frac{E}{100}$	≤ 0.1
L_{SHR}	≤ 0.2	≤ 0.2	—
$\|\Delta x\|$ (cm)	≤ 3	≤ 3	—
$\|\Delta z\|$ (cm)	≤ 5	≤ 5	—
χ^2_{strip}	≤ 10	≤ 15	—
$\chi^2_{3\times3}$	—	—	≤ 3
VTX occupancy	—	—	≥ 0.5
ISO (GeV)	≤ 4	≤ 4	≤ 4
Conversion removal	Yes	Yes	Yes
Fiducial area	Yes	Yes	Yes

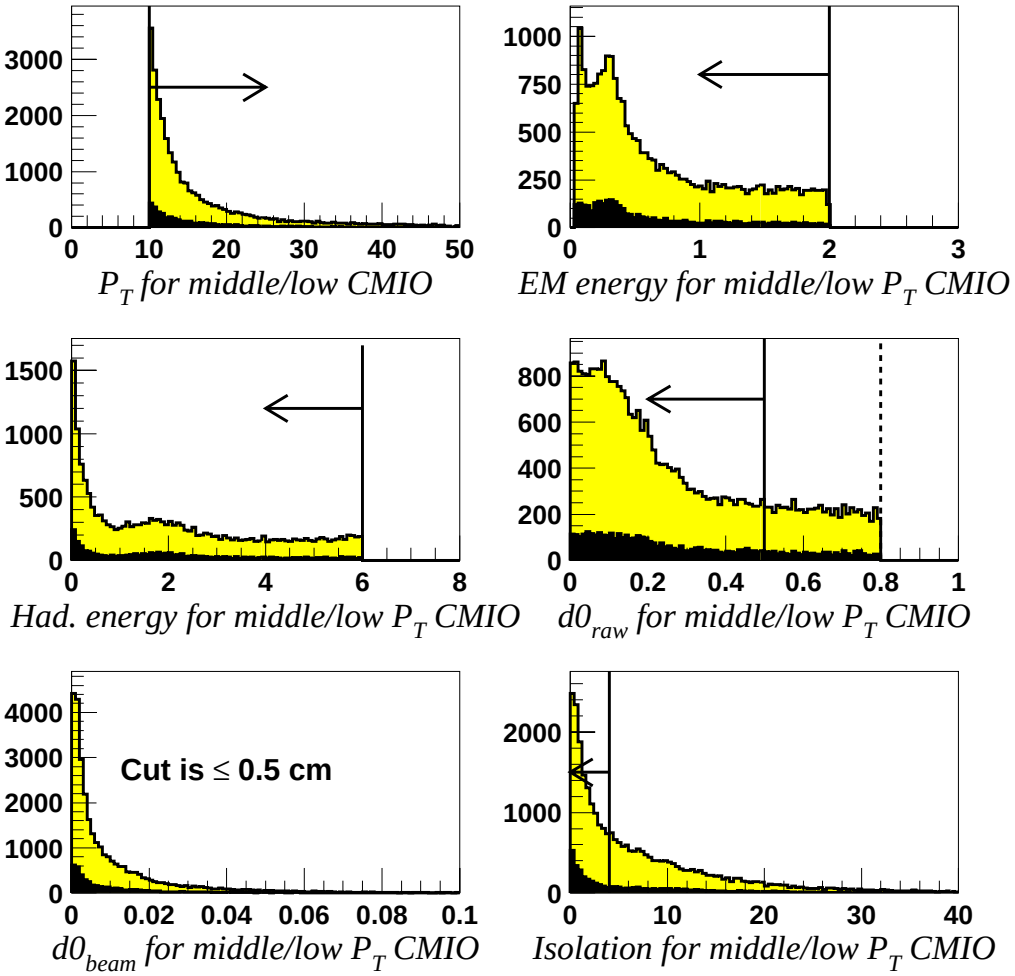

Figure 4.13: Distributions for CMIO muons which pass the loose ID cuts. The light histogram is the distribution after the skimming cuts have been applied to two leptons, and the dark histograms is after the third lepton requirement has been imposed. The dashed lines indicate the skimming cut value and the solid line indicates the analysis cut value. In histograms with only one line either the cut value was the same for the skim and analysis or the cut was not applied during the skim. The arrows indicate the accepted values.

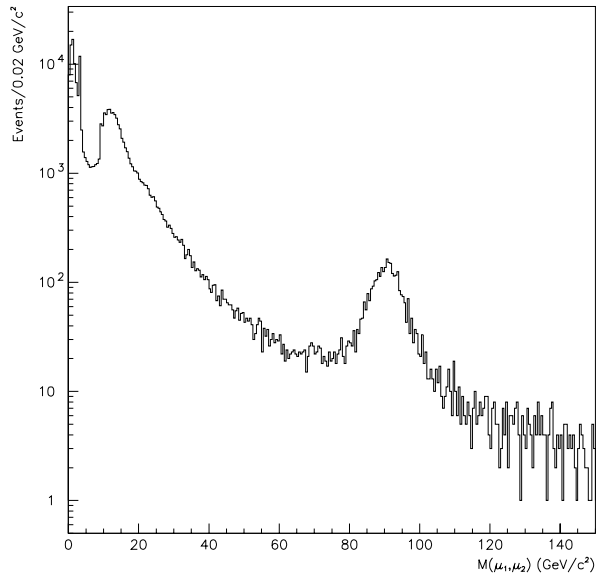

Figure 4.14: The two body mass for opposite sign muon pairs after loose identification cuts are applied. Peaks at the J/ψ, Υ and Z^0 masses can clearly be seen. The peak at 20 GeV/c^2 is Drell-Yan; it is due to trigger turn-on effects.

Electron Identification Cuts

Four electron identification cuts are added and two are changed:

P_T is relaxed to 2 GeV/c for all CEM electrons. We relax this cut since a cut on E_T is more appropriate for electrons (a more accurate measurement) and the E_T cut is increased.

E_T is increased to 11 GeV (from 8 GeV) for the tight electron and 5 GeV (from 4 GeV) for the loose electron. This cut is increased to remove background events with minimal effect on signal acceptance.

Conversion removal is the removal of electrons that are from photon conversion. We use the CDF standard routine CONVERT to see if there are two opposite-sign tracks pointing to the electron cluster. If there are, this is likely a photon that converted in the material of the solenoid.

Fiducial area requires the electron is in a region of the CEM or PEM known to function well. We use the CDF standard routine FIDELE.

ISO is the isolation of the electron. It requires the energy in a cone of $\Delta R \equiv \sqrt{\Delta\phi^2 + \Delta\eta^2} = 0.4$ minus the electron energy be less than 4 GeV. We use 4 GeV as that value is nearly 100% efficient for real electrons from electroweak type decays.

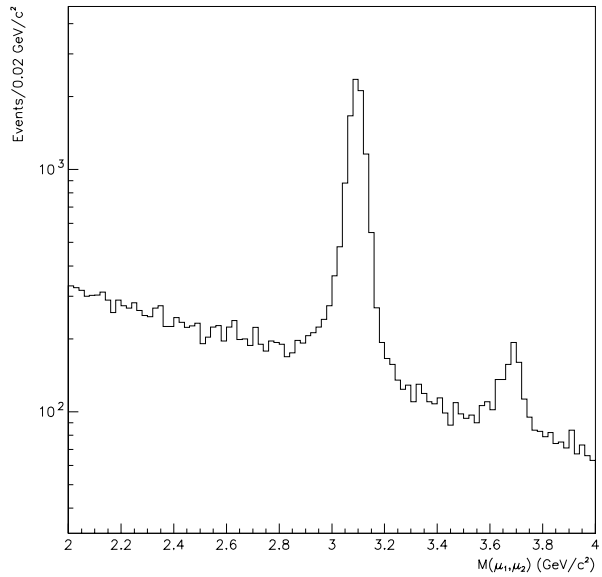

Figure 4.15: Two body mass for opposite sign muon pairs in the skimmed dilepton sample in the J/ψ region. Both J/ψ and ψ' can clearly be seen.

Table 4.7 lists the number of electrons after each cut when the analysis cuts are applied to CEM (tight), CEM (loose) and PEM electrons.

Muon Identification Cuts

Two muon identification cuts are added and three are changed:

P_T is increased to 11 GeV/c (from 7.5 GeV) for a tight CMU/P muon and 4 GeV/c (from 2.8 P_T) for a loose CMU/P or CMX muon. The CMIO cut remains unchanged at 10 GeV/c. This cut is increased to remove background events with minimal effect on signal acceptance.

d_0 **raw** is tightened to 0.5 cm (from 0.8 cm) for loose CMU/P, CMX or CMIO muons. It is unchanged for tight CMU/P muons. This cut and the following one serve to remove cosmic rays.

d_0 **beam** is the beam constrained impact parameter. It uses the beam position (in z) to determine the impact parameter of the muon and thus can be much tighter cut. We require a tight CMU/P muon have d_0 beam ≤ 0.2 cm and a loose CMU/P, CMX or CMIO muon have d_0 beam ≤ 0.5 cm.

ISO is the isolation of the muon. It requires the energy in a cone of $\Delta R \equiv \sqrt{\Delta\phi^2 + \Delta\eta^2} = 0.4$

Table 4.6: Analysis lepton selection cuts for CMU/P, CMX and CMIO muons.

Lepton class	Tight	Loose	
Cut variables	CMU/P	CMU/P or CMX	CMI
p_T (GeV/c)	≥ 11	≥ 4	≥ 10
EM (GeV)	≤ 2	≤ 2	≤ 2
Had (GeV)	≤ 6	≤ 6	≤ 6
d_0 raw (cm)	≤ 0.5	≤ 0.5	≤ 0.5
d_0 beam (cm)	≤ 0.2	≤ 0.5	≤ 0.5
CMU Matching	$\lvert\Delta x\rvert \leq 2$ cm or $\chi^2_{CTC} \leq 9$	$\lvert\Delta x\rvert \leq 2$ cm or $\chi^2_{CTC} \leq 9$	—
CMP Matching	$\lvert\Delta x\rvert \leq 5$ cm or $\chi^2_{CTC} \leq 9$	$\lvert\Delta x\rvert \leq 5$ cm or $\chi^2_{CTC} \leq 9$	—
CMX Matching	—	$\lvert\Delta x\rvert \leq 5$ cm or $\chi^2_{CTC} \leq 9$	—
ISO (GeV)	≤ 4	≤ 4	≤ 4
EM+Had (GeV)	≥ 0.1	≥ 0.1	≥ 0.1
Fiducial area	Not used	Not used	Yes

Table 4.7: Number of CEM and PEM electrons left in trilepton events after each analysis lepton identification cut. See Table 4.5 and the text for an explanation of each cut. A dash indicates that cut was not applied. Note that a) electrons which pass the tight cuts are not counted in the loose column and b) events can have more than one tight electron.

Lepton class	Tight	Loose	
Cut variables	CEM	CEM	PEM
Before Cuts	47	27	6
p_T	40	20	—
E_T	25	20	6
E/p	21	14	—
HAD/EM	21	14	6
L_{SHR}	20	13	—
$\lvert\Delta x\rvert$	20	13	—
$\lvert\Delta z\rvert$	20	13	—
χ^2_{strip}	20	13	—
$\chi^2_{3\times3}$	—	—	3
VTX occupancy	—	—	0
ISO	20	13	0
Conversion removal	20	13	0
Fiducial area	20	13	0

minus the muon energy to be less than 4 GeV. We use 4 GeV as that value is nearly 100% efficient for real muons from electroweak type decays.

EM + Had requires the muon deposit at least 100 MeV in the calorimeters.

Fiducial area requires that a CMIO muon does not point at a muon chamber, since if it did it would have made a muon stub. We use the CDF standard routine CMUSWM.

Table 4.8 lists the number of muons after each cut when the analysis cuts are applied to CMU/P (tight), CMU/P (loose), CMX and CMIO muons.

4.3 Bad Run Removal

Some of the remaining 247 events are from data later identified as bad. Reasons for bad data include having portions of the detector turned off or bad beam conditions. We use the CDF standard routine BADRUN to determine if the data was good. This routine examines a data base and returns a code [34] on a run by run basis. We accepted data where all the muon chambers were functioning correctly. After removing bad runs we are left with 232 events.

4.4 Cosmic Ray Removal

Cosmic rays are constantly passing through the earth and through the CDF detector. They appear as muons and thus are a substantial background to this analysis. We use two different techniques to remove cosmic rays from our sample: a CDF standard routine and a custom routine that examines the opening angle between the muon and the difference in the time when each particle passed through the hadron calorimeter.

4.4.1 CMCOS

The routine CMCOS is an on-line cosmic ray filter [35]. A cosmic ray will generally manifest itself as two tracks that are exactly back to back in η and ϕ. Since the cosmic ray travels through the detector (rather than originating at the center and traveling outward), the difference in the timing signals for the two legs will be separated by the time (t_0) required to traverse the detector. Muons can be marked as cosmic rays for three reason:

1. The muon impact parameter was larger than 0.5 cm or there was no primary vertex within 5 cm in z.

2. There were two tracks ($P_T > 10$ GeV/c) that were within 2° of being back-to-back in ϕ and

had $|\eta| < 1.2$ and a muon impact parameter greater than 0.5 cm, or one of the tracks failed track quality cuts and had a muon impact parameter less than 0.5 cm.

3. There were two tracks ($P_T > 10$ GeV/c) that were within 2° of being back-to-back in ϕ and had $|\eta| < 1.2$ and a muon impact parameter less than 0.5 cm but had a large t_0 difference for the two muons.

We required all muons in an event pass all three of these tests. Figure 4.16 shows the status of the CMCOS filter bit for the candidate events. This removed 115 events, bringing the number of good three leptons events to 117.

4.4.2 Angle plus timing

The track reconstruction software uses timing information to correctly create tracks from hits in the CTC. Thus, a track originating at the outside of the detector will not have correct timing information (since the code is optimized for tracks that start at the interaction region). Occasionally, the track reconstruction software will create two track where only one exists. One of the tracks will be correlated with hits in a muon chamber and will be labeled a CMUO. The other track will be labeled a CMIO. However, these two tracks are from the same object. There is an additional CMUO directly opposite so these events are identified as three lepton events. Figure 4.17 is an example of such an event. Since we search for events with three leptons, we can find the opening angle between all three possible pairs of leptons. Events of the type in question will appear to have two pairs with an opening angle very close to π. Also, the t_0 recorded by the HTDCs for the muons on the opposite sides of the detector will be the time required to travel across the chamber. Figure 4.18 shows the highest dilepton opening angle versus the middle dilepton opening angle for sample Monte Carlo point 12 (see Table 5.2 and Figure 4.19 and Figure 4.20 show the angles for $Z^0 \rightarrow \mu\mu$ plus a third muon (data) and the trilepton data set. As can be seen, neither the Monte Carlo nor the Z^0 samples show any events in the extreme upper right corner; the trilepton data has many events there. Thus, to remove these cosmic rays, we remove events with both the highest and middle opening angles greater than 3 radians.

To further ensure that we are not removing any signal, we also impose a HTDC cut. We remove events where the difference in time for the two opposite muons be at least 12 ns. Figure 4.21 shows the difference in timing for the two most opposite muons for events that do and do not have the necessary kinematics. As can be seen, events with two large opening angles all have large ΔHTDC. Figure 4.22 shows the timing for Z^0 events. Of events with two back-to-back tracks, 92% have ΔHTDC > 12 ns, and 96% of events with two sets of back-to-back tracks have ΔHTDC $>$ 12 ns. Events with two sets of back-to-back tracks are almost always cosmic rays.

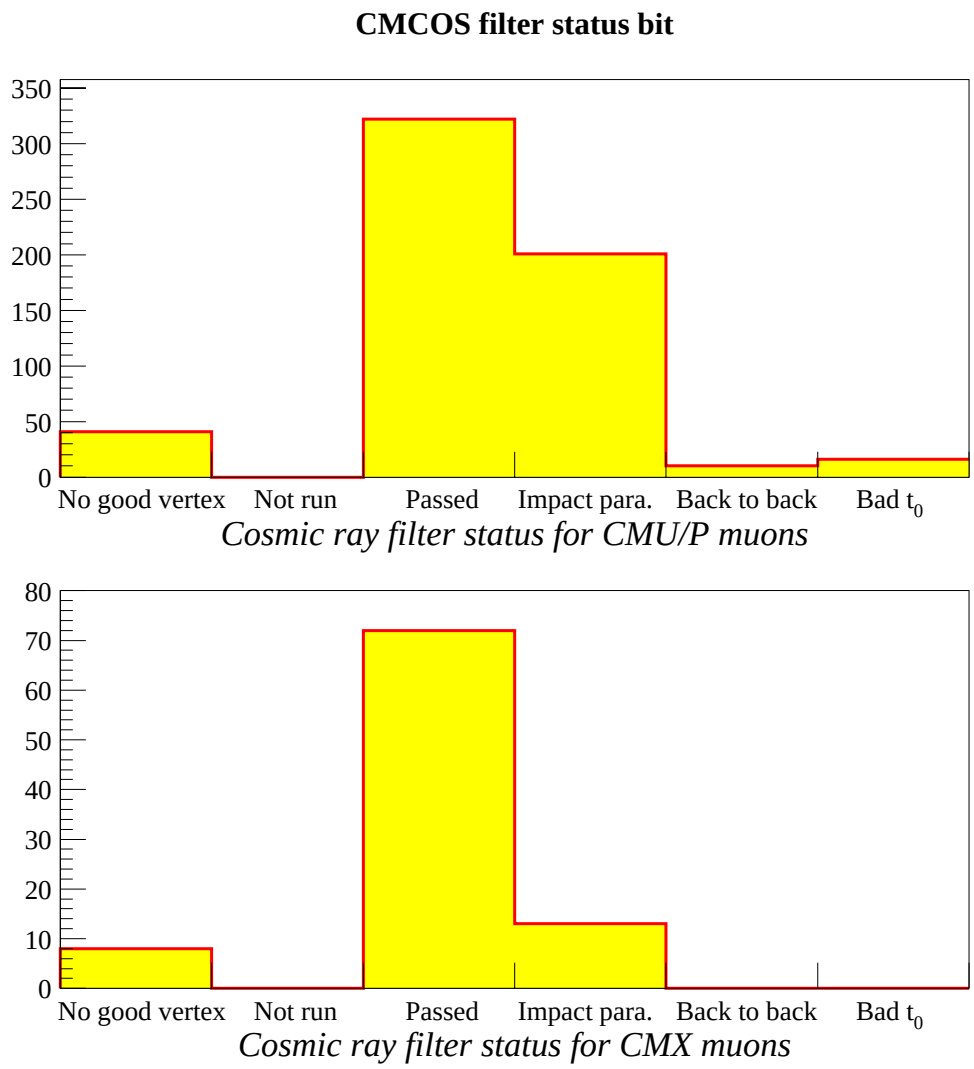

Figure 4.16: Cosmic ray filter status bit for candidate CMU/P and CMX muons. Good muons are required have a filter bit of 'pass'. See the text for details of the bits. Recall that each event can have up to three muons, and if any of the muons are marked as cosmics, the event is rejected.

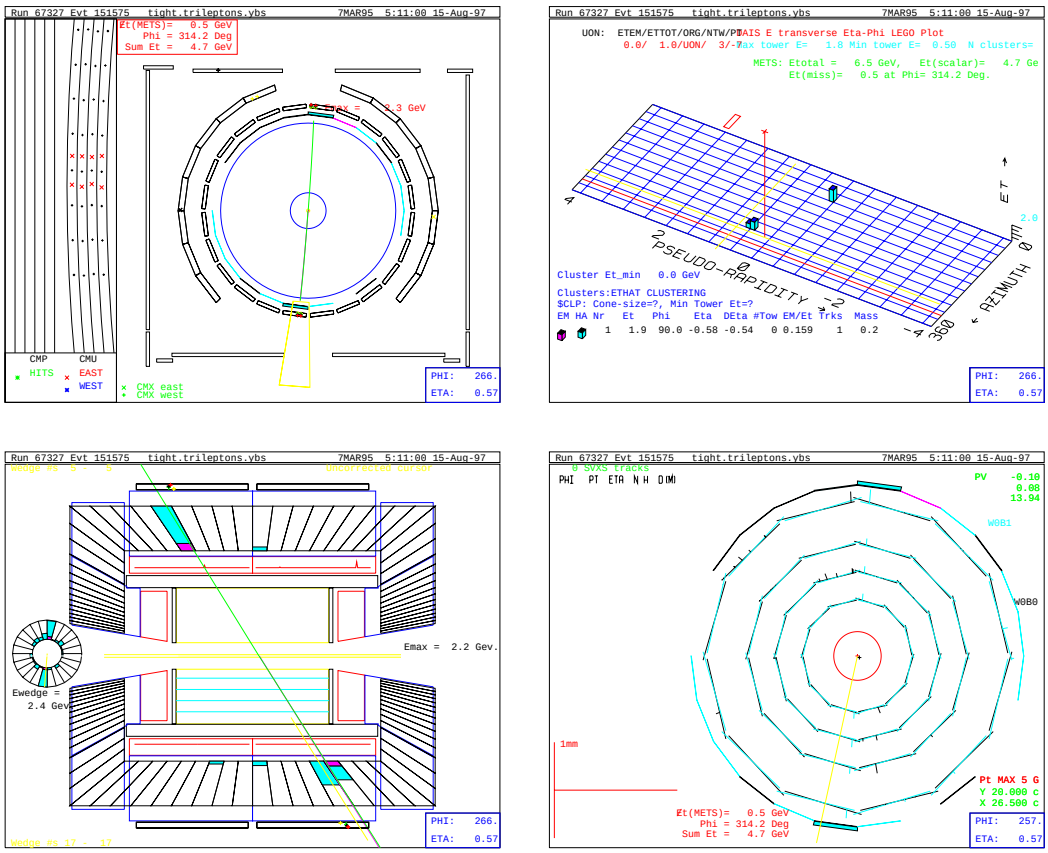

Figure 4.17: CDF event display for a cosmic ray of the type described in Section 4.4.2. The upper left display is the CTC and muon chambers. These tracks are very back to back in ϕ. The left section are the hits in the muon chambers (there appear to be two sets due to the left-right ambiguity of the chamber). The upper right display is a LEGO plot of the calorimeters. The maximum tower energy is 2 GeV. The lower left display is a side-view slice of the entire detector. Again, these tracks are very back to back in η. The lower right display is the SVX. There is clearly no evidence of a second track near the line at 270° (0° is 3 o'clock), where we should see the CMIO.

Table 4.8: Number of CMU/P, CMX and CMIO muons left in trilepton events after each analysis lepton identification cut. See Table 4.6 and the text for an explanation of each cut. A dash indicates that cut was not applied. Note that a) muons passing the tight cuts are not counted in the loose column and b) an event can have more than one muon passing the tight cuts.

Lepton class	Tight	Loose		
Cut variables	CMU/P	CMU/P	CMX	CMI
Before Cuts	627	247	103	227
p_T	488	227	96	227
EM	487	226	95	208
HAD	487	226	94	208
d_0 raw	479	218	94	200
d_0 beam	388	218	94	199
Matching	387	216	94	—
ISO	387	216	94	198
EM+HAD	387	216	94	198
Fiducial area	—	—	—	198

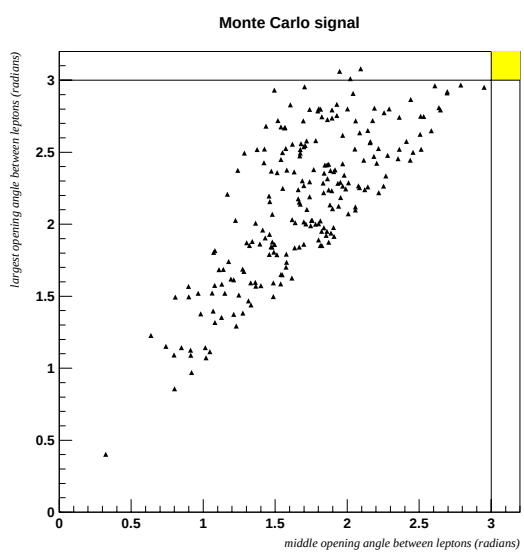

Figure 4.18: Maximum and middle opening angles for the three possible lepton pair combinations for a sample Monte Carlo point. As can be seen, there are no events in the extreme upper right corner.

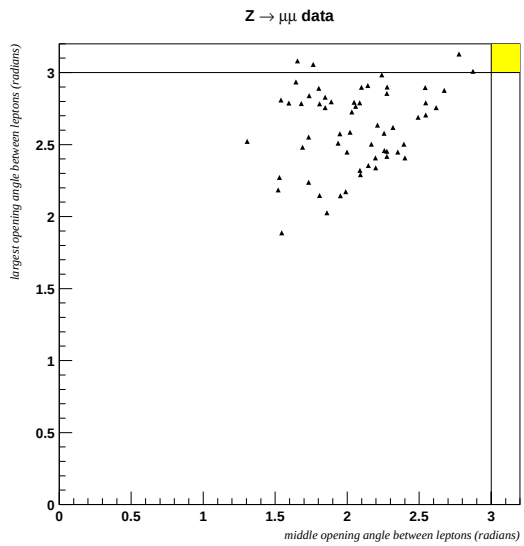

Figure 4.19: Maximum and middle opening angles for the three possible lepton pair combinations for $Z^0 \rightarrow \mu\mu$ events with a third μ (data). As can be seen, there are no events in the extreme upper right corner.

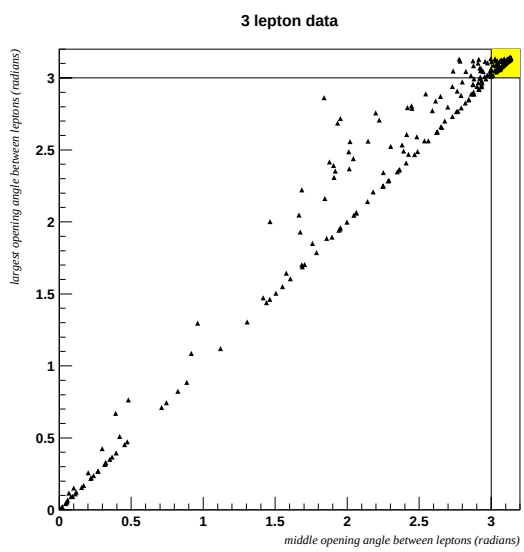

Figure 4.20: Maximum and middle opening angles for the three possible lepton pair combinations for the trilepton data set. As can be seen, there are many events in the extreme upper right corner.

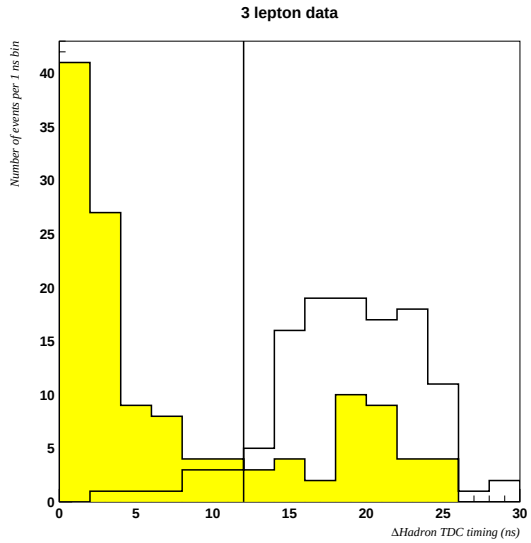

Figure 4.21: The difference in time for muon pairs. The open histogram is for events with two muons back-to-back to a third, and the hatched histogram is for all other three muon events. The two histograms clearly peak in different places. The peak at 20 ns for the 'normal' events is from cosmic rays where the third muon is a real muon not associated with the cosmic ray. Those events are flagged with CMCOS and thus are marked as cosmics. The cosmic rays all have large differences in timing, as expected for events that pass through the detector.

QFL does not properly simulate the HTDCs so this cut cannot be modeled. However, our signal events should be similar to the Z^0 events. Thus, we believe this cut is 100% efficient for signal. 47 events are removed with this cut, leaving us with 70 good trilepton events.

4.5 Vertex Requirements

The primary vertex for an event is the point where the p and $\bar{p}$ interacted. We impose two different vertex requirements:

- We require all three leptons have $z_{vertex} < 60$ cm to ensure high quality tracks in the CTC.
- We require all three leptons are associated with tracks that are within 10 cm of the same VTVZ z-vertex. We impose this cut to remove events with leptons that do not originate from the primary vertex. This is not applied to PEM electrons as they may not be associated with a good track.

After we apply these cuts we are left with 59 trilepton events.

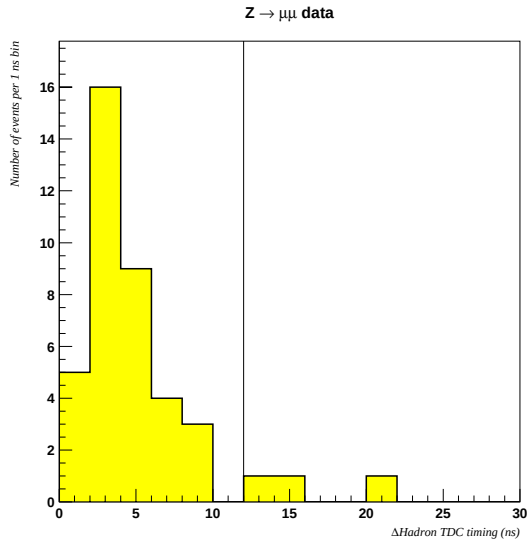

Figure 4.22: The difference in timing for $Z^0 \rightarrow \mu\mu$ events (from data) with a third muon in the event. These events have small differences in timing for the two muons, as is expected for events that originate in the center of the detector.

4.6 Background Removal

As discussed in Section 2.4, there are several SM processes which can also yield a final state with three leptons. However, by examining the kinematics of our signal events and the background events, we can devise a series of cuts that removes the background but preserves our signal.

Recall Figures 2.19 and 2.20, the Feynman diagrams for two- and three-body decays of the $\tilde{\chi}_1^{\pm}$ and $\tilde{\chi}_2^0$. All possible decays which yield three leptons do not contain jets. Thus, there should be little additional energy around each lepton: they should be well isolated. The leptons will not be particularly back-to-back in either the three- or the two-body decays. Since these are massive objects, the leptons should also not be particularly close together in the detector and they should all originate from the same vertex. The neutralino will always decay to two opposite sign, same flavor leptons (plus an LSP).

There are two main type of events that can be accepted by the analysis so far: events with three real leptons, and events with two real leptons plus an object that is mistakenly identified as a real lepton. This fake lepton can be, for example, a real lepton from the underlying event, a decay in flight, or a hadronic track misidentified as a lepton.

To calculate the number of expected background events, we use ISAJET v7.06 and ISAJET v7.20 [36] to generate the events and QFL v3.48 for the simulation. We use the structure functions CTEQ-2l, MRSD0' and GRV-lo so we can calculate the uncertainty in the structure functions. We

model the trigger as described in Section 5.1.1.

4.6.1 Real trilepton events

Processes that can make three real leptons include $b\bar{b}$, $t\bar{t}$ and diboson (Z^0Z^0 and $W^{\pm}Z^0$) production. We generate $b\bar{b}$ events with initial- and final-state gluon radiation as well as direct three lepton production, with P_T ranging from 10 to 500 GeV/c; $t\bar{t}$ events with a P_T range of 0.1 to 500 GeV/c; and Z^0Z^0 and $W^{\pm}Z^0$ events with a P_T range of 0.1 to 500 GeV/c.

$b\bar{b}$ Production

A typical b decay is $b \to W^*c \to W^*(W^*d)$. Either W^* has a 22% chance of decaying to an e or μ. In 4.8% of the decays, both W^* will decay leptonically. If either of the W^* from the $\bar{b}$ also decays leptonically, we will have three real leptons in the event. This has a probability of 2%. Since bs are copiously produced at the Tevatron, $b\bar{b}$ can be a substantial background. However, a b quark is light compared to the center of mass energy at the Tevatron and thus generally has a large momentum. This means the leptons will be in the same direction as the rest of the b decay products. An isolation cut is an effective way to remove this background. Also, both leptons from the same b will in the same direction. Requiring the leptons be in different parts of the detector will also reduce this background. Figure 4.23 shows the isolation for $b\bar{b}$ and Figure 4.24 shows the lepton opening angle ($\Delta R \equiv \sqrt{\Delta\eta^2 + \Delta\phi^2}$). For comparison, we show the isolation for Z^0 data (which should be similar to our signal events) and the opening angle for Monte Carlo point 12. A final technique to remove $b\bar{b}$ is to require an opposite sign, same flavor pair of leptons, since the flavor of the leptons from the b and c decays are not correlated.

We require leptons to have an isolation of 2 GeV or less[6], and the opening angle between any two leptons must be greater than 0.4 radians.

$t\bar{t}$ Production

A top quark will always decay $t \to W^{\pm}b$ in the SM. If the $W^{\pm}$ decays leptonically, that lepton will be isolated. However, we can get at most two leptons from the $W^{\pm}$ decays (one from the t and one from the $\bar{t}$) so at least one of the leptons will come from a semi-leptonic decay of a b. Thus, we can apply the same isolation cut used to remove pure $b\bar{b}$ production. Also, the production cross section for $t\bar{t}$ is quite small so this background is negligible.

[6]This is a tightening of the 4 GeV isolation cut used in the lepton ID stage.

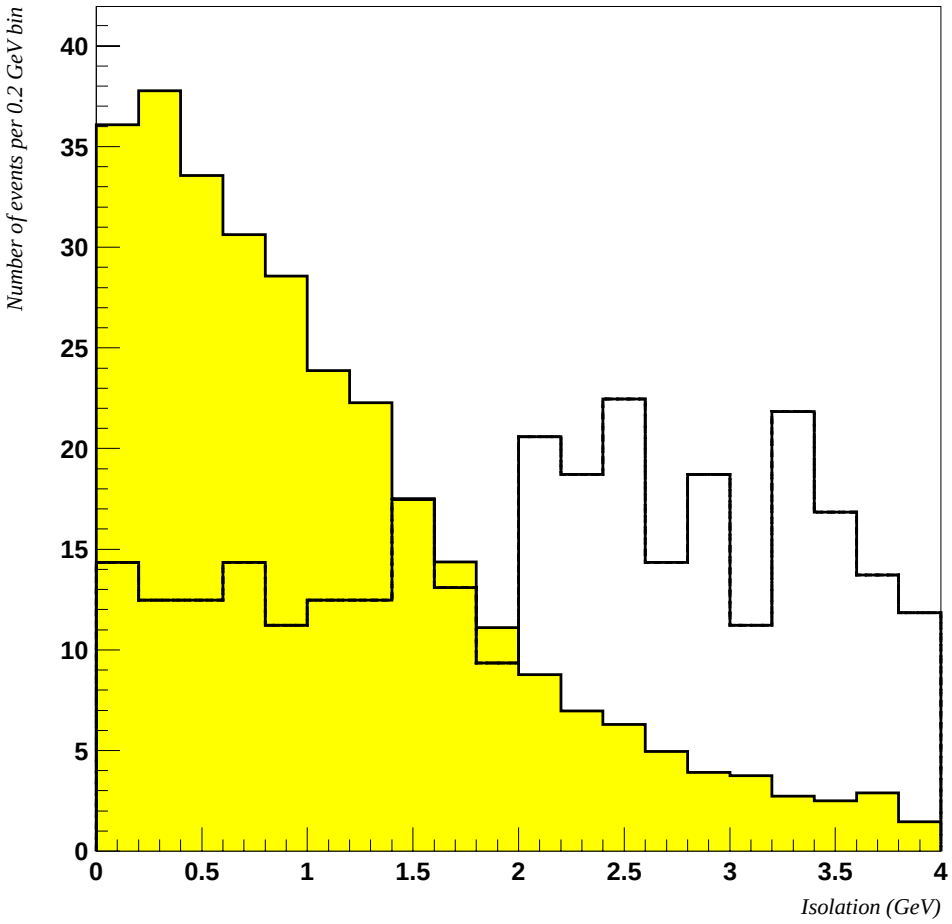

Figure 4.23: Isolation for leptons from b quark decays (open histogram) and Z^0 boson (filled histogram) production. These leptons are required to pass our analysis ID cuts. Leptons from Z^0 production are much more isolated than those from b quark decays. These histograms are not normalized; they are simply for shape comparison.

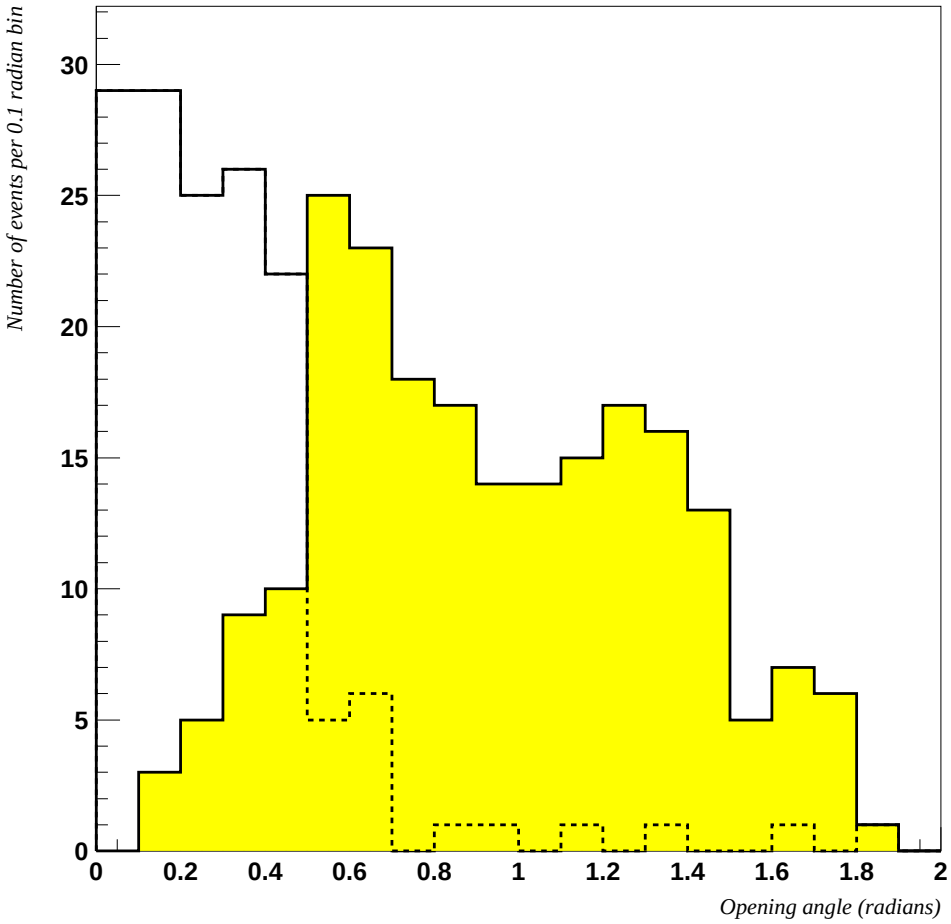

Figure 4.24: Smallest opening angle for lepton pairs from b quark decays (open histogram) and SUSY Monte Carlo signal (filled histogram). We examine all three possible lepton pair combinations and plot the smallest opening angle. Note that the leptons b quark decay are quite close together while those from our signal tend to be separated. These histograms are not normalized; they are simply for shape comparison.

Diboson Production: Z^0Z^0 and $W^{\pm}Z^0$

Both the production cross section for Z^0Z^0 ($\sigma = 1.0$ pb, BR = 0.45% to e or μ) and $W^{\pm}Z^0$ ($\sigma = 2.5$ pb, BR = 1.44% to e or μ) and the branching ratio to three lepton final states are small. However, the leptons from either Z^0Z^0 or $W^{\pm}Z^0$ are very similar to those from our signal events, so we must be able to remove this type of background. Both of these types of events contain a Z^0, so we can use a Z^0 mass window cut to remove them. Figure 4.25 shows all possible two body masses from Z^0Z^0, $W^{\pm}Z^0$ and signal MC point 12.

We remove an event if any of the three possible two-body masses are in the range 75 GeV/c$^2 \leq M_{\ell\ell} \leq$ 105 GeV/c^2.

4.6.2 Dilepton plus misidentified lepton events

Processes which produce two real leptons include $b\bar{b}$, $c\bar{c}$, Drell-Yan (γ and Z^0) and W^+W^- production. We generate Drell-Yan γ events with P_T ranging from 5 to 500 GeV/c; Drell-Yan Z^0 events with P_T ranging from 0.1 to 5 GeV/c and 5 to 500 GeV/c; and W^+W^- events with P_T ranging from 0.1 to 500 GeV/c.

Measurement of the misidentified lepton rate

To measure the rate of lepton misidentification, we use a clean $W^{\pm}$ sample [37]. We impose the same lepton ID cuts described above to find $W^{\pm}$ in 21 pb^{-1} of Run IB data. We further require the event to have

- a lepton with $P_T > 20$ GeV/c,
- $\not{E}_T > 20$ GeV and
- 40 GeV/c$^2 < M_T(P_T, \not{E}_T) <$ 100 GeV/c^2.

Any event passing these cuts we call a $W^{\pm}$. We find 16,596: 10,861 $W^{\pm} \to e\nu$ and 5,735 $W^{\pm} \to \mu\nu$. Any object in these events that is not the $W^{\pm}$ lepton and passes our lepton ID cuts is a fake lepton. We find 48 such objects, for a fake lepton rate of 0.289±0.042%. No event had more than one fake lepton so this is the probability that a $W^{\pm}$ event will contain a fake lepton. Since there are so few fakes we assume no P_T dependence on the rate of fake leptons and use 0.289±0.042% as the probability that any event will have a fake lepton.

To calculate the number of events due to (dilepton + fake) we only require two leptons pass our analysis code. We then use the probability of each event having a fake lepton times the number of two leptons events as the number of expected background due to (dilepton + fake).

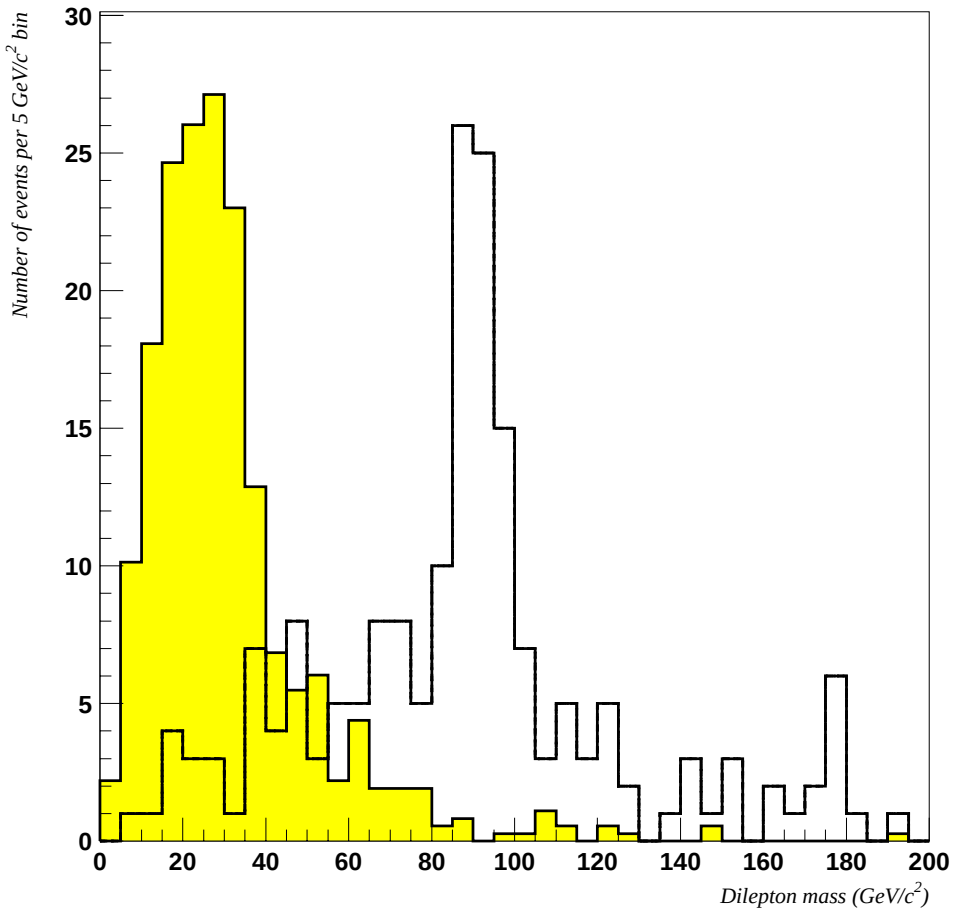

Figure 4.25: Two-body masses for diboson background events (open histogram) and SUSY signal point 012 (filled histogram). Since there are three possible combinations of two leptons, we plot all three masses. Any event which has a lepton pair with mass in the cut region is removed. Thus, practically all $W^{\pm}Z^0$ and Z^0Z^0 events are removed with this cut. Note that the signal events have a much lower mass peak, even though the $\tilde{\chi}_1^{\pm}$ mass is 67 GeV/c^2 for this point. These histograms are not normalized; they are simply for shape comparison.

As we find no events with two fake leptons we do not look at background from (single lepton + two fakes).

$b\bar{b}/c\bar{c}$ Production

This background is virtually identical to the three real lepton background due to $b\bar{b}$. Thus, we remove it with the isolation and ΔR cuts described above.

Drell-Yan (Z^0 and γ) Production

The Drell-Yan background can be split up into three categories: γ production, and low- and high-P_T Z^0 production. Events from γ production can be removed with an opening angle cut (see Figure 4.26). Low-P_T Z^0 will produce leptons that are extremely back-to-back, so they can also be removed with an opening angle cut (see Figure 4.26). Leptons from high-P_T Z^0 decays will not be back to back so we remove them with a Z^0 mass window cut (Figure 4.27).

To remove this type background we require the opening angle between the two highest P_T leptons be less than 2.96 radians (170°) and the event not have a dilepton mass pair in the range 75 GeV/c^2 $\leq M_{\ell\ell} \leq$ 105 GeV/c^2.

W^+W^- Production

Like the other diboson processes, W^+W^- production has a low production cross section (σ = 9.5 pb). For an event from W^+W^- production to be accepted, it must also have a fake lepton. Thus, the probability of such an event contaminating our sample is small. The kinematic tools we used to remove the backgrounds above cannot be used here: the leptons are uncorrelated, so we can use neither the maximum nor the minimum lepton opening angle; the leptons will not form a distinctive mass peak; and the leptons are from $W^\pm$ decay and so are well isolated. However, each $W^\pm$ can decay to either e or μ with equal probability. Since the leptonic decay of the $\tilde{\chi}_2^0$ will always have an opposite sign same flavor pair of leptons, we can reduce this background by 50% by requiring such a pair of leptons.

4.6.3 Missing Transverse Energy Measurement

After all the cuts above are applied, we may still have a few events remaining. Since our signal events should have substantial missing energy (from the two LSPs and the ν), we can further reduce the expected background by imposing a $\not{E}_T$ cut.

Figure 4.28 shows the $\not{E}_T$ contributions from each of the separate backgrounds and from a sample signal point. We require each event have $\not{E}_T >$ 15 GeV.

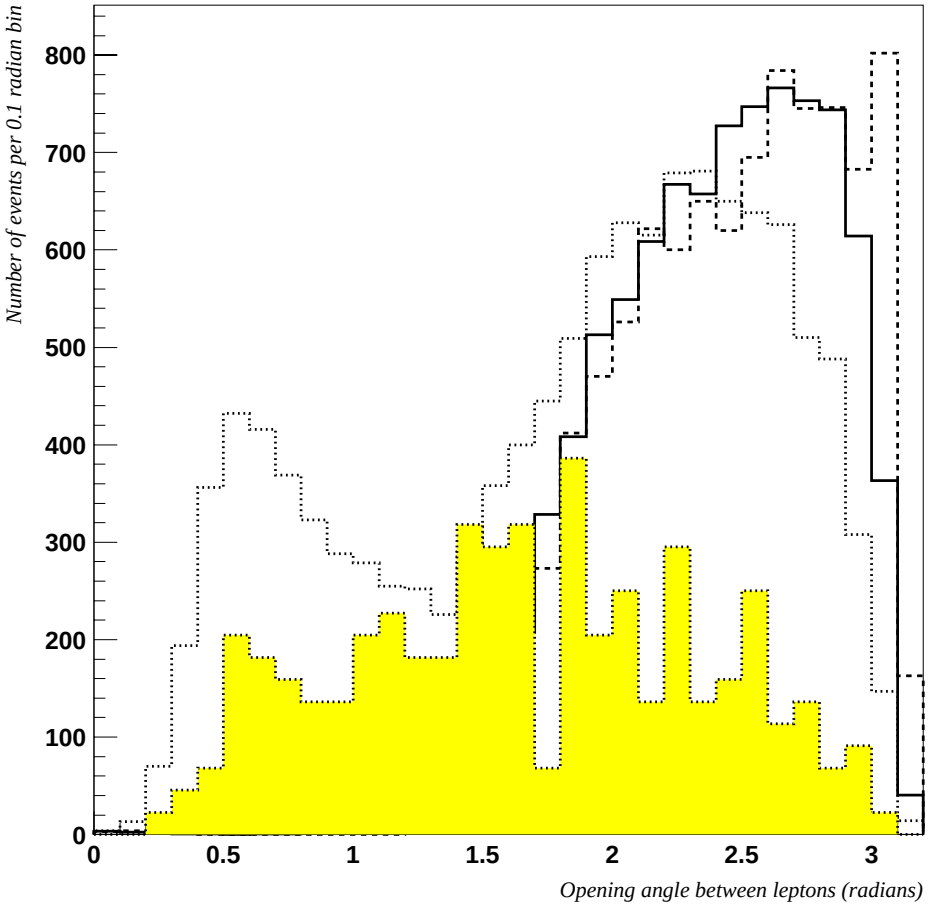

Figure 4.26: Opening angle for background due to Drell-Yan processes. The solid line is high-P_T Z^0, the dashed is low-P_T Z^0, the dotted is γ and the filled histogram is SUSY point 012. The Drell-Yan background is far more likely to have a large opening angle between the two highest P_T leptons that is the SUSY signal. These histograms are not normalized; they are simply for shape comparison.

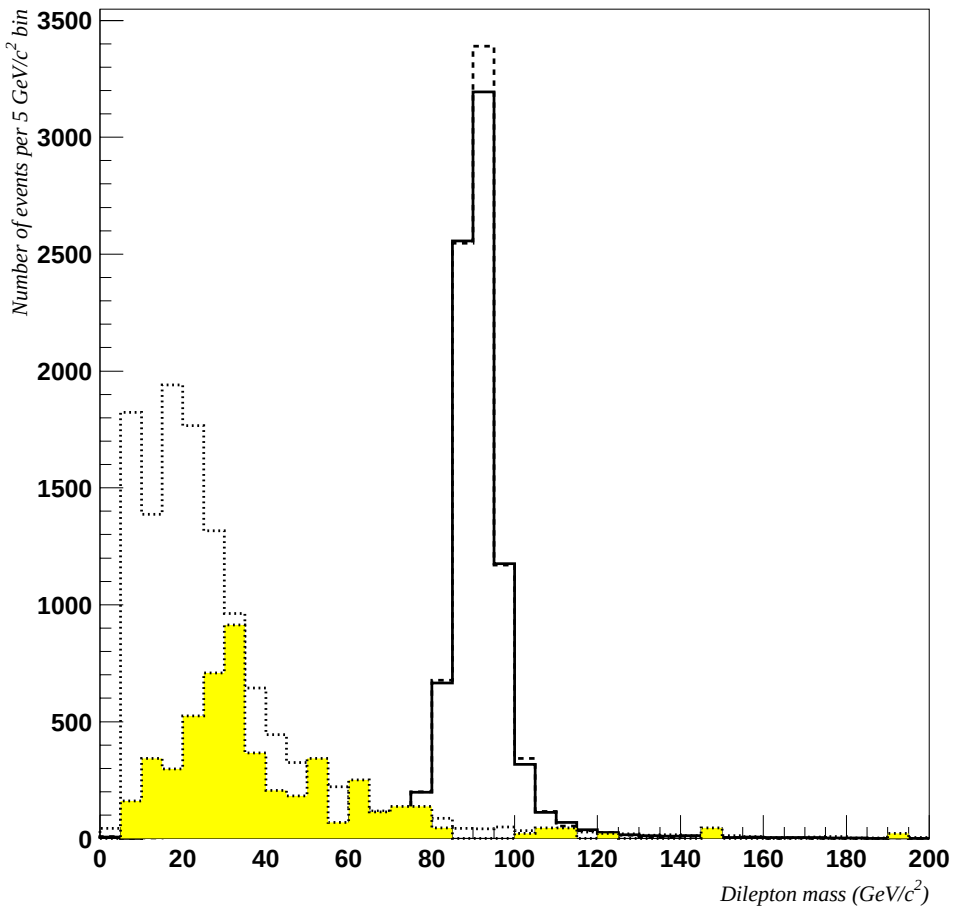

Figure 4.27: Dilepton mass for background due to Drell-Yan processes. The solid line is high-P_T Z^0, the dashed is low-P_T Z^0, the dotted is γ and the filled histogram is SUSY point 012. Both the Z^0 processes are removed with a Z^0 mass window cut. These histograms are not normalized; they are simply for shape comparison.

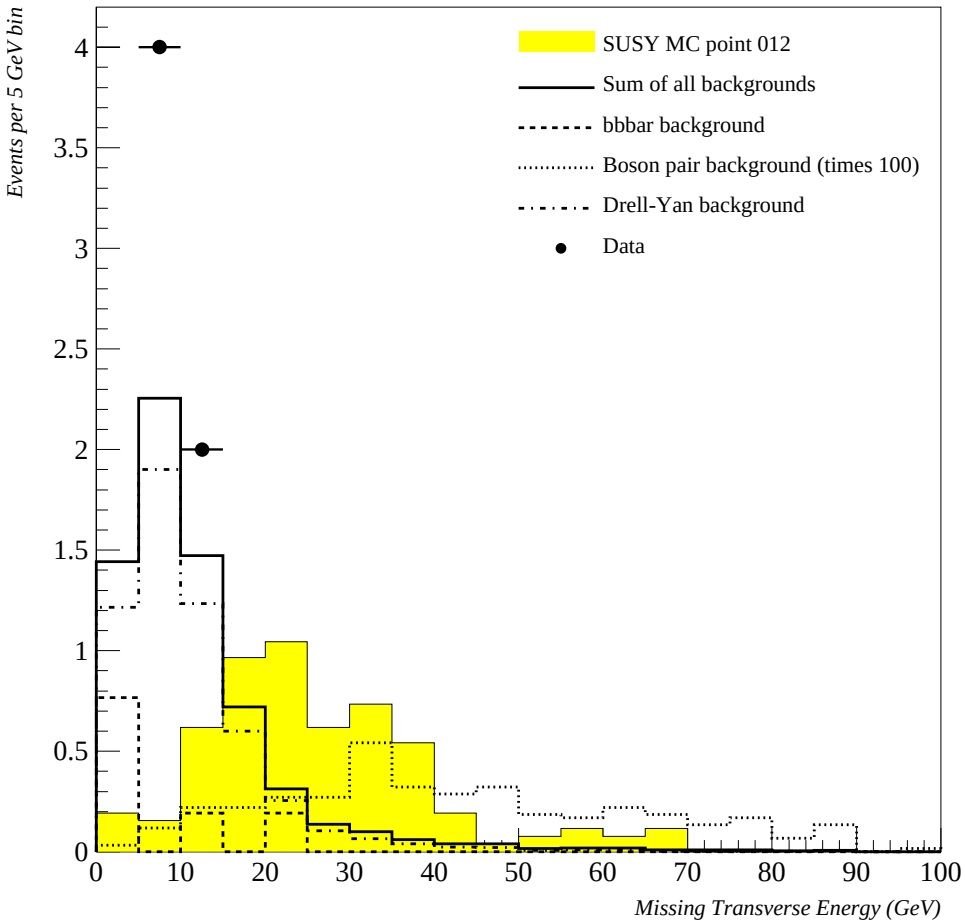

Figure 4.28: Missing transverse energy for each of the types of background and a sample signal point (012). The dashed line is $b\bar{b}$, the dot-dash line is Drell-Yan, the dotted line is boson pair production and the solid line is the sum. The filled histogram is MC signal point 012. Each histogram is normalized such that the area of the histogram is equal to the number of events expected after all cuts but before the $\not{E}_T$ cut. The boson pair histogram is multiplied by 100 so it is visible. The data are indicated by circles (•).

Table 4.9: Number of expected background events after each cut, for contributions from $b\bar{b}/c\bar{c}$, boson pair, Drell-Yan and $t\bar{t}$. All numbers are scaled by the Monte Carlo correction factor discussed in Chapter 3. The fake lepton rate (0.00289/event) is applied to all dilepton backgrounds. As can be seen, the isolation and ΔR cuts reduce the heavy flavor contribution, the Z^0 mass cut removes the boson pair and Drell-Yan contributions, and the $\Delta\phi_{\ell\ell}$ cut further reduces the Drell-Yan contribution. The $\not\!\!E_T$ cut reduces the total expected background to 0.99 events.

	Events remaining after each cut				
Cut	$b\bar{b}/c\bar{c}$	Boson pair	Drell-Yan	$t\bar{t}$	Sum
3 lepton requirement	14.83	0.58	20.46	0.05	35.92
good run requirement	14.83	0.58	20.46	0.05	35.92
cosmic removal	14.83	0.58	20.46	0.05	35.92
$\lvert z_{vertex}\rvert < 60$ cm	14.60	0.52	19.57	0.04	34.73
Vertex Requirements	14.22	0.52	19.57	0.04	34.35
$ISO < 2$	3.17	0.48	18.77	0.02	22.44
$\lvert Q_1+Q_2+Q_3\rvert < 3$	3.17	0.48	18.77	0.02	22.44
Require e^+e^- or $\mu^+\mu^-$	2.71	0.46	18.30	0.02	21.49
$\Delta R_{\ell\ell} > 0.4$	1.70	0.45	18.21	0.01	20.37
$\Delta\phi_{\ell_1\ell_2} < 170°$	1.70	0.38	7.86	0.00	9.94
Z^0 removal (75-105 GeV/c^2)	1.70	0.04	5.81	0.00	7.55
Υ removal (9-11 GeV/c^2)	1.70	0.04	5.49	0.00	7.23
J/ψ removal (2.9-3.1 GeV/c^2)	1.15	0.04	5.49	0.00	6.68
$\not\!\!E_T >$ 15 GeV	0.00	0.02	0.97	0.00	0.99

4.6.4 Estimate of Expected Background

We generate a large quantity of Monte Carlo background for each type of event: at least 60 pb^{-1} for $b\bar{b}/c\bar{c}$, 100-400 pb^{-1} for each of the Drell-Yan types, 5,000 pb^{-1} for $t\bar{t}$and 2,000-7,000 pb^{-1} for boson pair. We examine each type of background with our analysis code and apply the lepton ID cuts and additional cuts described above. Table 4.9 lists the number of events expected after each cut from each type of background. Table 4.10 compares the sum from background to the number of data events and a sample MC signal point. As can be seen, the data and the MC background agree quite well. After all cuts, we expect to see 0.99±0.2 events and see none.

After all cuts, no events remain in the data and the number of events before the final cuts are applied agree well with the expected background. We see no evidence for Supersymmetry.

Table 4.10: Number of expected background, data and signal Monte Carlo events left after each cut. Below the line the data and background predictions agree quite well. Above the line the cuts remove both predictable background and unpredictable background (such as cosmic rays and multiple interactions). This is especially true for the ΔR cut– we expect to remove 1 event and instead remove 14. Examination of these events shows they are clearly cosmic rays. After all cuts, we expect 0.99 events from background and see none. For the sample Monte Carlo signal point 012, we expect 4.47 events after all cuts.

Cut	Background	Data	Signal MC
3 lepton requirement	35.92	247	8.44
good run requirement	35.92	232	8.44
cosmic removal	35.92	70	8.44
$\lvert z_{vertex}\rvert < 60$ cm	34.73	66	8.01
Vertex Requirements	34.35	59	8.01
$ISO < 2$	22.44	23	6.89
$\lvert Q_1+Q_2+Q_3\rvert < 3$	22.44	23	6.89
Require e^+e^- or $\mu^+\mu^-$	21.49	23	6.89
$\Delta R_{\ell\ell} > 0.4$	20.37	9	6.81
$\Delta\phi_{\ell_1\ell_2} < 170°$	9.94	8	6.19
Z^0 removal (75-105 GeV/c^2)	7.55	7	5.95
Υ removal (9-11 GeV/c^2)	7.23	7	5.49
J/ψ removal (2.9-3.1 GeV/c^2)	6.68	6	5.49
$\not{E}_T >$ 15 GeV	0.99	0	4.47

Chapter 5

Limits on the SiMSSM parameter space

We see no evidence for Supersymmetry. However, it is instructive to examine a few models and set limits on the production of $\tilde{\chi}_1^{\pm}$ and $\tilde{\chi}_2^0$. We can then find the naturalness of SUSY with our limits, and can also compare our sensitivity to that of other experiments. I will describe the Monte Carlo simulation techniques, the limit setting method, and the limits on the SUGRA-inspired MSSM, the SU(5)×U(1) Supergravity model, and SUGRA.

5.1 Monte Carlo Simulation techniques

Simulating both background and SUSY signal events is a two stage process. First, we use a Monte Carlo program to generate the events. For this analysis, we use ISAJET v7.06 (for much of the background calculation) and ISAJET v7.20 (for all of the signal calculation) [36]. There are no substantial differences between the versions; v7.20 contains bug fixes which were corrected manually in v7.06. ISAJET is a general Monte Carlo program that can be used to generate events for any Standard Model process as well as many different SM extensions. We use it for all the background processes (see Section 4.6) and to generate a wide variety of points in SiMSSM space.

A generated event cannot be examined using the analysis code. The information is limited to the P_T, η and ϕ for each particle and the decay chains. We use QFL (see Section 3.2.7) to include detector effects (such as resolution and smearing). As mentioned in Section 3.2.7, QFL is over-efficient for lepton identification so we apply an overall correction factor of 0.864/event. After the events generated with ISAJET are simulated with QFL, they are identical in structure to data taken with the detector.

The simulated events are examined with the analysis program, with one addition. Data that is recorded must pass through the trigger system. QFL simulation does not include a simulation of

the trigger. We use a trigger simulation program written specifically for SUSY analyses, MC_WGT.

5.1.1 Trigger Simulation

There is no specific trigger path which events must follow to enter our data set. This has both advantages and disadvantages. Since this is a search for new physics, allowing all possible signal events into the data is the proper technique. However, this means events can follow any one of many trigger paths. For the dilepton data set on which this analysis is based, many different triggers contribute to the data set. To properly simulate a trigger, we must include several effects: the actual trigger efficiency and both static and dynamic prescales.

The trigger efficiency for each trigger is taken from a variety of CDF Notes [38]. This information is coded (in either 500 MeV or 1 GeV lepton E_T (P_T) bins) into the trigger simulation routine MC_WGT. Each event is passed to this routine. The E_T (P_T) and η for each lepton in the event is examined to see which possible Level 1, Level 2 and Level 3 triggers it could have passed. For many detector regions, there are several possible triggers which could be used. The trigger which returns the highest probability at each level is the probability that that lepton would pass that trigger level. The values for different detector regions and lepton species are ORed together[1] and this number is the probability that this event would pass that trigger level. The values returned from each trigger level are multiplied and the total is the probability that this particular event would have entered the data set.

To calculate the static and dynamic prescales, we use SIGMON [39]. SIGMON examines the online LUMMON[2] data files to find the actual luminosity recorded for each trigger on a run-by-run basis. This can be compared to the luminosity recorded for each run to determine the effective prescale of each trigger for each run. We divide the Run IB data into three bins according to the average instantaneous luminosity for each run ($\mathcal{L} < 1.7 \times 10^{30}$ s^{-1}cm^{-2}, $1.7 < \mathcal{L} < 4 \times 10^{30}$ s^{-1}cm^{-2} and $\mathcal{L} > 4 \times 10^{30}$ s^{-1}cm^{-2}) and find the effective prescale for each trigger in each $\mathcal{L}$ bin (Table 5.1[3]). We then calculate a weighted average of each of the prescale bins as a function of the percent of the total integrated luminosity from Run IB in each bin. The low instantaneous $\mathcal{L}$ bin has 43%

[1] If trigger a has efficiency ϵ_a and trigger b has efficiency ϵ_b the total efficiency is

$$\epsilon_{a+b} = \epsilon_a + \epsilon_b(1 - \epsilon_a).$$

[2] LUMMON is an online program that monitors the amount of data recorded by each trigger during a run. It also controls the dynamic prescales.

[3] The names of the triggers can easily be converted to a meaningful statement. For example, the trigger CEM_8_CFT_7_5_XCES requires at least 8 GeV in the CEM, a CFT track with P_T above 7.5 GeV/c and a good hit in the CES. Numbers written as words ('TWO') indicate the number of objects required in a particular detector. 5DEG indicates how close a muon stub must be to matching the extrapolation of a CTC track.

Table 5.1: The Level 2 triggers used in this analysis and the effective prescale as a function of instantaneous luminosity. For this analysis, low $\mathcal{L}$ means $\mathcal{L} < 1.7 \times 10^{30}$ s^{-1}cm^{-2} (43% of the data), middle is $1.7 < \mathcal{L} < 4 \times 10^{30}$ s^{-1}cm^{-2} (41% of the data) and high is $\mathcal{L} > 4 \times 10^{30}$ s^{-1}cm^{-2} (16% of the data).

Trigger	Low $\mathcal{L}$	Middle $\mathcal{L}$	High $\mathcal{L}$	Average
CEM_8_CFT_7_5_XCES	1.11	1.29	1.55	1.21
TWO_CMU_TWO_CFT_2_2	1.00	1.00	1.00	1.00
CMUP_CFT_12_5DEG	1.00	1.00	1.00	1.00
CEM_5_CFT_4_7_CMU_2_7	1.72	2.19	3.35	2.14
CMX_CMU_TWO_CFT_2_2	1.05	1.39	3.02	1.50
TWO_CMU_ONE_CFT_2_2_6TOW	1.11	1.26	1.56	1.24
CMNP_CFT_12_5DEG	1.35	7.58	31.27	8.69
CMUP_CFT_7_5_5DEG	1.18	2.52	6.16	2.53
CEM_16_CFT_12	1.00	1.00	1.00	1.00
CMX_CFT_12_5DEG	5.25	5.70	16.67	7.26

of the data, the middle instantaneous $\mathcal{L}$ bin 41%, and the high instantaneous $\mathcal{L}$ bin 16%. This final number is the effective prescale for the entire IB data set for each trigger. It is entered in the MC_WGT routine and applied to each event, depending on which trigger that event passes.

This technique for including the prescale effect as a part of the trigger efficiency simplifies several calculations. This also automatically applies the prescale to both background and signal Monte Carlo studies.

To minimize the statistical uncertainty in our Monte Carlo studies, we generate numbers of events corresponding to large $\int \mathcal{L}dt$. We maintain a database listing the $\int \mathcal{L}dt$ for each sample and use this normalize to the amount of data present in Run IB. This constant is also included as part of the trigger efficiency.

The final trigger efficiency returned for each event is a product of four numbers: a weighting factor for the $\int \mathcal{L}dt$, the Level 1 trigger efficiency, the Level 2 trigger efficiency (including the prescale) and the Level 3 trigger efficiency.

5.2 Limit setting method

We generate and analyze a statistically significant number of events for a particular point in SiMSSM space to determine if we should see evidence for $\tilde{\chi}_1^{\pm}\tilde{\chi}_2^0$ production at that point. We use the formula

$$\sigma_{\tilde{\chi}_1^\pm \tilde{\chi}_2^0} \cdot \mathrm{BR}(\tilde{\chi}_1^\pm \tilde{\chi}_2^0 \to 3\ell + X) \quad > \quad \frac{N_{exp}}{\epsilon^{tot} \cdot \int \mathcal{L} dt} \tag{5.1}$$

to compare the predicted production cross section ($\sigma_{\tilde{\chi}_1^\pm \tilde{\chi}_2^0}$) times branching ratio to trileptons ($\mathrm{BR}(\tilde{\chi}_1^\pm \tilde{\chi}_2^0 \to 3\ell + X)$) with the number of expected events (N_{exp}) divided by the total event acceptance (ϵ^{tot}) times the integrated luminosity.

5.2.1 N_{exp}: Systematic Uncertainty

The number of expected events is calculated by taking a Poisson distribution for having seen 0 events and convolving it with a Gaussian[4] whose width is determined by the total systematic uncertainty. The systematic uncertainty has several components:

- Uncertainty in the total integrated luminosity: 8% [40].
- Uncertainty in the trigger efficiency [41]. We determine the trigger efficiency for a particular trigger by studying electron or muon events which pass triggers other than the one we are examining. We then impose the trigger conditions and count the number of events passing. We find that the total trigger efficiencies for electrons and muons are [42, 43]

$$\begin{aligned} \epsilon_e^{trig} &= (87.3\ ^{+3.8}_{-4.9})\%, \\ \epsilon_\mu^{trig} &= (87.1 \pm 2.9)\%. \end{aligned}$$

  In a multi-lepton event analysis, we must take into account the possibility of events with multiple trigger-leptons: (a) one trigger lepton and (b) two trigger leptons. [Note that there were no three lepton triggers available in Run IB, so we do not have to worry about that case.]

  We obtain a conservative estimate of the trigger efficiency uncertainty by assuming all dilepton events are in case (a). The electron trigger has the largest uncertainty and so we use that value. This situation gives a trigger efficiency uncertainty of ±5.6%.

- Uncertainty in the trilepton finding efficiency:

[4]The number of expected events for having seen 0 using a Poisson distribution at a 95% Confidence Level is 3.0. A Poisson distribution can only take integer values. However, we can be more precise if we combine the information from the Poisson distribution with a Gaussian distribution. A Gaussian distribution is continuous. For more details see pg. 166 of Ref. [5].

- Uncertainty in the degradation of the Isolation cut: ±8% [44]. This is important as we combine Run IA and IB data sets to increase the integrated luminosity (see Section 5.2.3). Run IB had much higher instantaneous luminosity, which degraded the efficiency of the isolation cut.
- Uncertainty in the Monte Carlo correction factor from Section 3.2.7: ±2%. We calculate this by taking the combination of three leptons (one tight and two loose) that give us the largest correction factor using the information in Table 3.2. For this analysis that combination is a tight CEM electron and two loose CMX muons (0.864±0.017: 0.017/0.864 = 2%).
- Uncertainty in the trilepton finding efficiency: ±2%. This is calculated by taking the combination of lepton finding efficiencies from Table 3.2 that results in the largest uncertainty. For this analysis that combination is a tight CEM electron and two loose CMIO muons.

- Uncertainty in the structure functions: ±7%. We used CTEQ-3L for all of the signal Monte Carlo generation and compared the results from it and an average of CTEQ-3L, GRV-94lo and MRS-D0′. The largest deviation between the two is our systematic uncertainty.
- Uncertainty in the fit for the detection efficiency (see Section 5.2.2): ±13%.

The uncertainties combine in quadrature for a total systematic uncertainty of ±20%. This yields $N_{exp} = 3.2$ at a Confidence Level of 95%.

5.2.2 ϵ^{tot}: Detection Efficiency

The detection efficiency is a combination of geometric acceptance, trigger efficiency and kinematic acceptance. Naïvely, one would expect the detection efficiency to be mainly a function of the $\tilde{\chi}_1^{\pm}$, $\tilde{\chi}_1^0$ and $\tilde{\chi}_2^0$ masses: since $M_{\tilde{\chi}_1^{\pm}} \approx M_{\tilde{\chi}_2^0} \approx 2M_{\tilde{\chi}_1^0}$, higher $\tilde{\chi}_1^{\pm}$ and $\tilde{\chi}_2^0$ masses result in stiffer (more energetic), easier to detect leptons. Figure 5.1 shows the detection efficiency as a function of $M_{\tilde{\chi}_1^{\pm}}$ for $\mu = -200$ GeV/c^2, $\tan\beta = 2$ and $M_{\tilde{q}} = M_{\tilde{g}}$. The detection efficiency clearly rises as a function of $M_{\tilde{\chi}_1^{\pm}}$. Figure 5.2 shows the detection efficiency for a variety of points in SiMSSM space where we varied μ, $M_{\tilde{q}}/M_{\tilde{g}}$ and $\tan\beta$. We fit a straight line to these points to get a function for the detection efficiency as a function of $M_{\tilde{\chi}_1^{\pm}}$. Figure 5.3 is a comparison between the fit to all points and a variety of subsets.

We found that the detection efficiency was not completely model independent: changing $\tan\beta$ changes the acceptance. Figure 5.4 shows the fit for points where we constrained $\tan\beta$ to be 2. The quality of the fit clearly improves. Because of this, we use the fit for SiMSSM points where $\tan\beta = 2$ and the individual acceptances for other points.

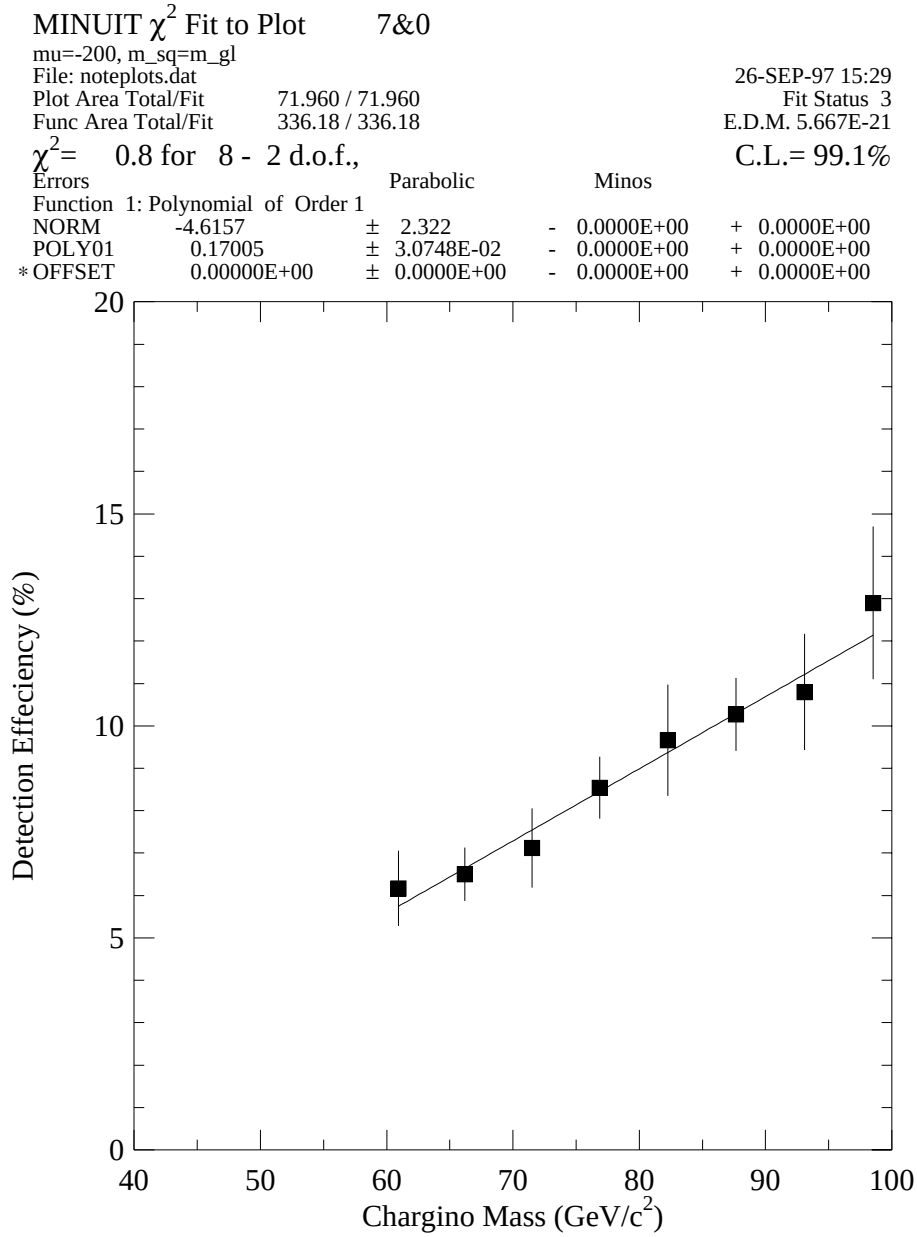

Figure 5.1: The detection efficiency as a function of $M_{\tilde{\chi}_1^\pm}$. For this plot we set $\mu = -200$ GeV/c^2, $\tan\beta = 2$ and $M_{\tilde{q}} = M_{\tilde{g}}$. The detection efficiency is clearly a function of the chargino mass.

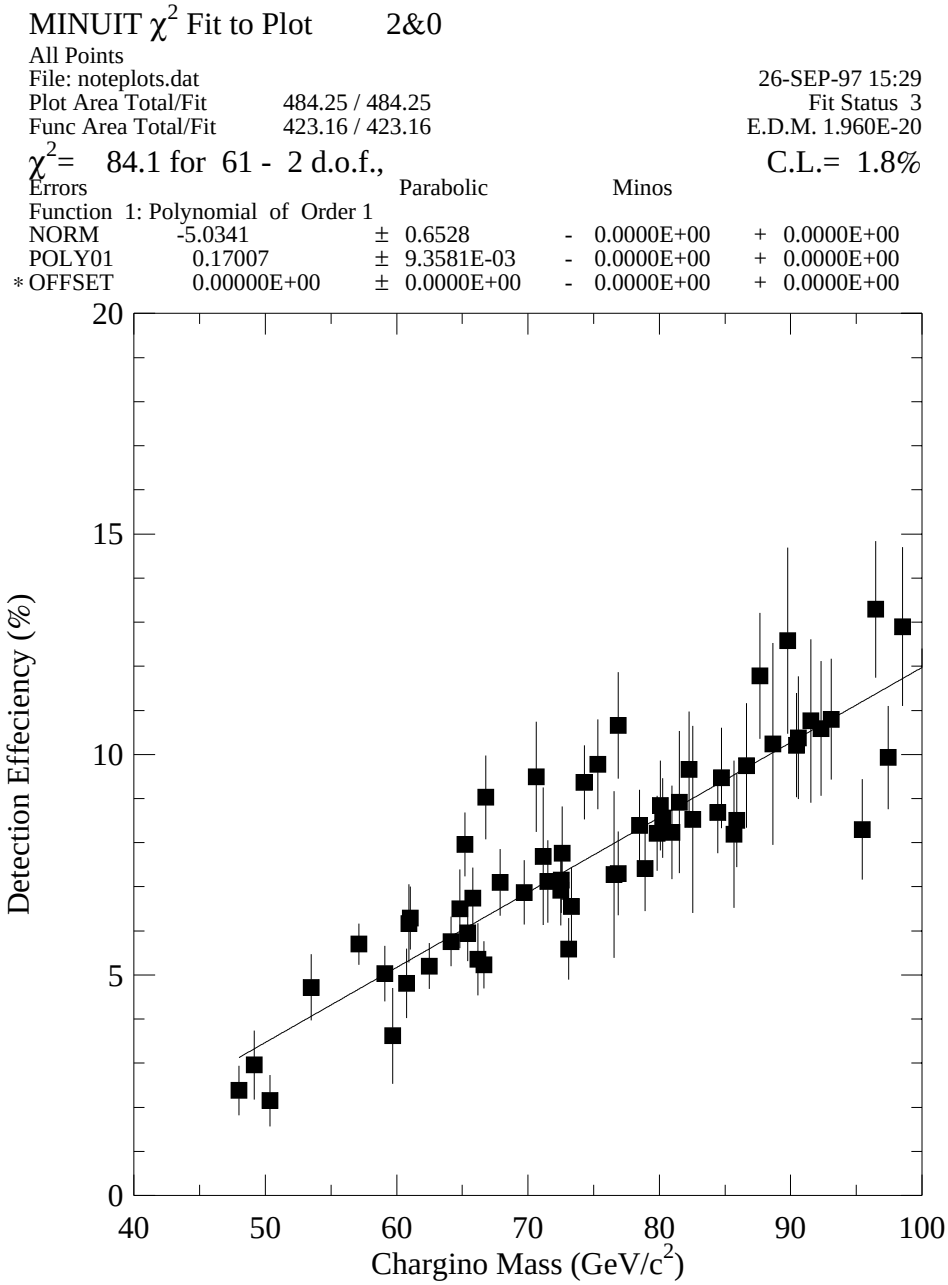

Figure 5.2: The detection efficiency as a function of $M_{\tilde{\chi}_1^\pm}$ for a variety of points in SiMSSM space.

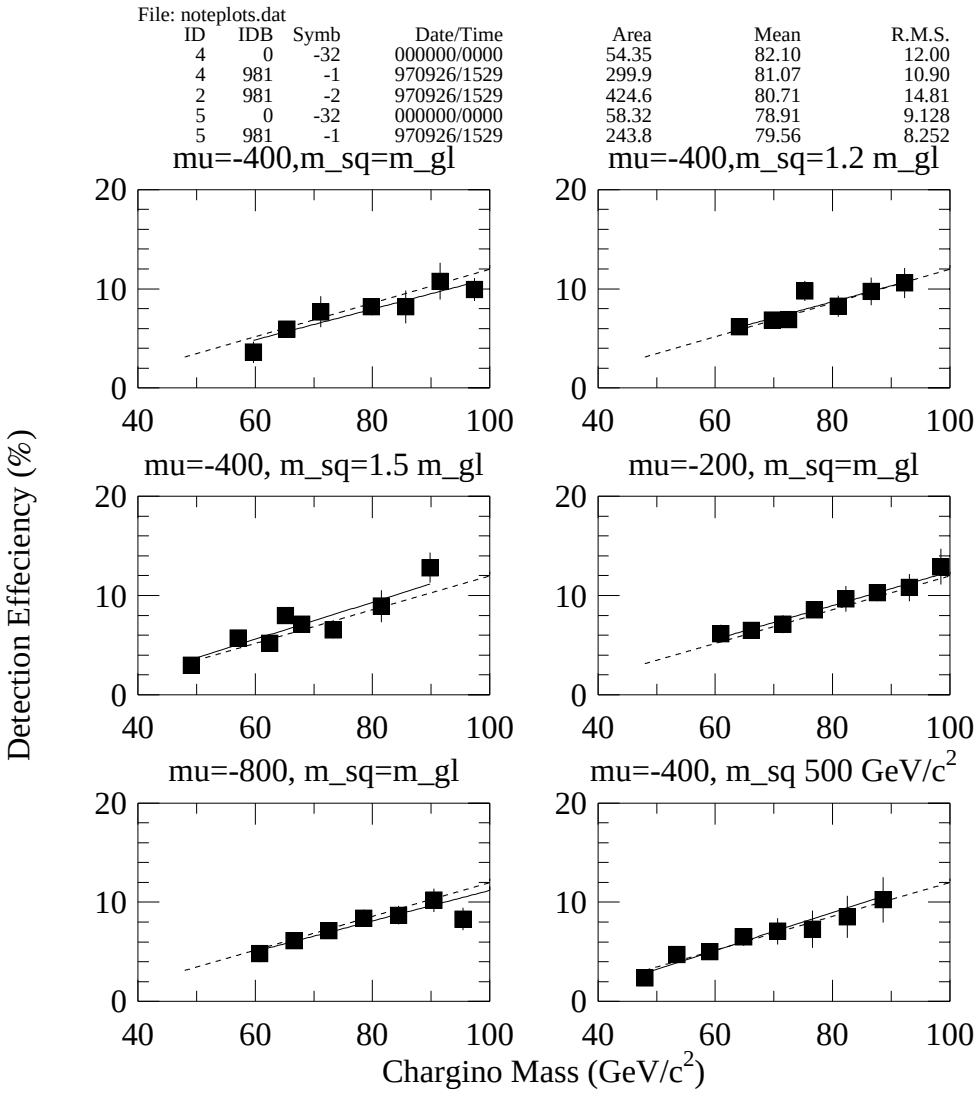

Figure 5.3: The detection efficiency as a function of $M_{\tilde{\chi}_1^\pm}$ comparing individual SiMSSM points to an overall fit. The fit agrees well with the individual points, so we use the overall fit for each of these points. In each plot the solid line is the fit to that particular set of points and the dashed line is a fit to all points with $\tan\beta = 2$.

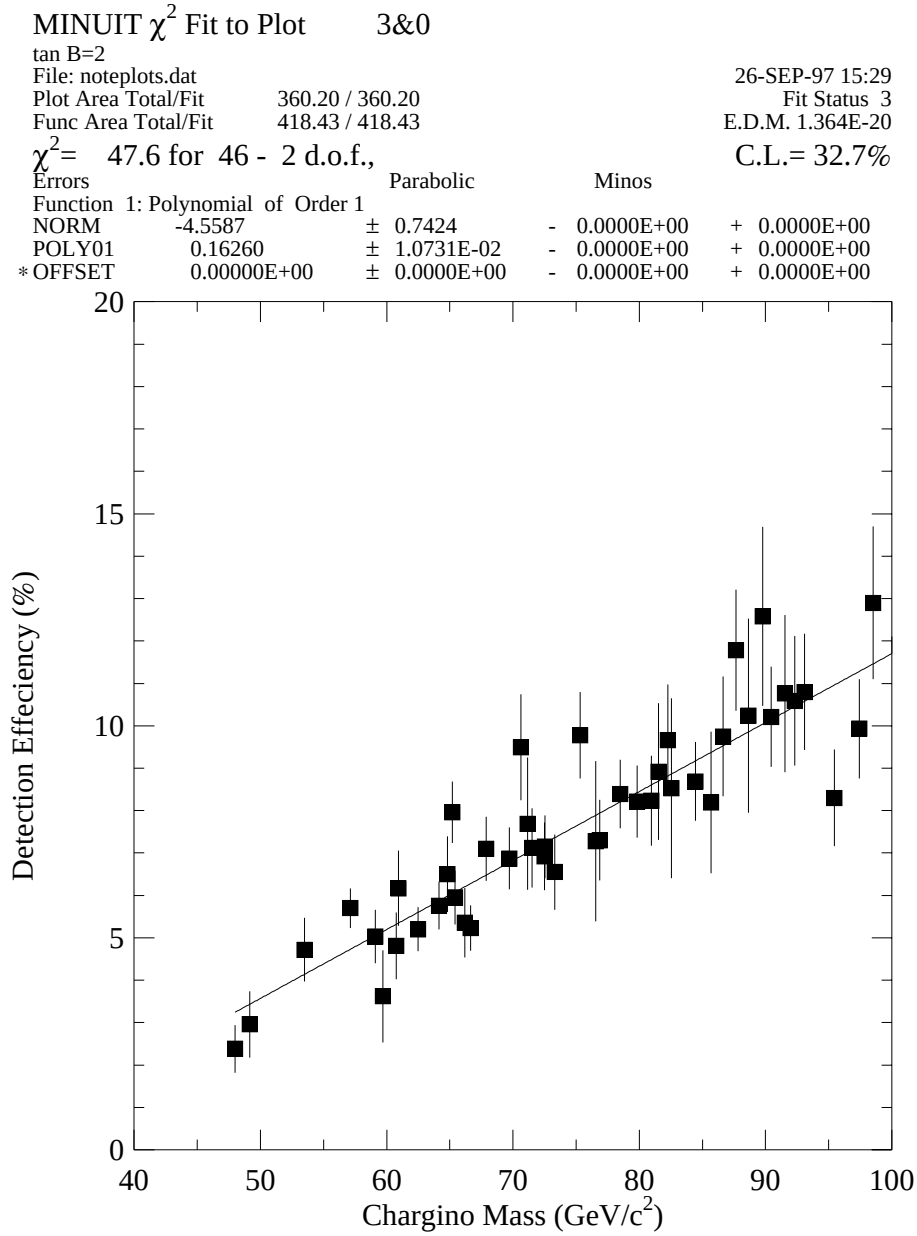

Figure 5.4: The detection efficiency as a function of $M_{\tilde{\chi}_1^\pm}$ for a variety of points in SiMSSM space, constraining $\tan\beta = 2$. The quality of the fit is better than when $\tan\beta$ is unconstrained.

It is appropriate to wonder why we want a functional form for the detection efficiency. To determine the detection efficiency, we must generate and simulate at least 20,000 events. This can take some time. If the detection efficiency is independent of the model parameters, than we need only calculate the cross section and branching ratio for a particular SiMSSM point. This is a much less time consuming process. For points where $\tan\beta = 2$, we use (see Figure 5.4)

$$\epsilon_{tot} = -4.56 + 0.16 M_{\tilde{\chi}_1^\pm}.$$

For all other points we use the ϵ_{tot} determined from Monte Carlo for that particular point. If we determine ϵ_{tot} for each SiMSSM point, the total systematic uncertainty drops from 20% to 15%. However, this only reduces N_{exp} from 3.2 to 3.1. The increased analysis speed is a great benefit, with only a small decrease in our limit.

5.2.3 $\int \mathcal{L}dt$: Integrated Luminosity

This analysis is primarily concerned with the Run IB data. However, a similar analysis was done using the Run IA data [45]. That analysis used identical cuts (but did not apply the $\not\!\!E_T$ cut) and had no events remaining. Thus, we can combine the 87.7 pb^{-1} Run IB data with the 19.1 pb^{-1} of Run IA data for a total of 107 pb^{-1}. We have no candidate events in the entire sample.

5.3 Limits on the SiMSSM

It is impractical for us to try to examine the entire SiMSSM parameter space, even after reducing to the six free parameters discussed in Chapter 2. We can further reduce the number of free parameters to four by noting that this analysis is insensitive to the top trilinear coupling (A_T) and the mass of the pseudoscalar Higgs boson (H_A). We set $A_T = \mu/\tan\beta$[5] and $M_{H_A} = 500$ GeV/c^2.[6] The remaining parameters are μ, $\tan\beta$, $\mathrm{M}_{\tilde{q}}$ and $\mathrm{M}_{\tilde{g}}$. Since the $\tilde{\ell}$ mass is mainly a function of $\Delta(M_{\tilde{q}}, M_{\tilde{g}})$ we replace $\mathrm{M}_{\tilde{q}}$ with $\mathrm{M}_{\tilde{q}}/\mathrm{M}_{\tilde{g}}$. However, we still need guidance to determine which regions of parameter space we should examine.

This analysis yields the strongest limits when the leptonic branching ratios of the $\tilde{\chi}_1^\pm$ and $\tilde{\chi}_2^0$ are maximized. This occurs for two reasons: small Higgsino content of the $\tilde{\chi}_1^\pm$ and $\tilde{\chi}_2^0$ (as Higgsino-like $\tilde{\chi}_1^\pm$ and $\tilde{\chi}_2^0$ prefer to decay to quarks), and small $\tilde{\ell}$ masses (as light, but still virtual, sleptons can enhance the leptonic branching ratio). A quick look at Figures 2.12 and 2.15 reveals gaugino-like $\tilde{\chi}_1^\pm$ and $\tilde{\chi}_2^0$ for $|\mu| \gtrsim 200$ GeV/c^2 or $1 \lesssim \tan\beta \lesssim 10$. The $\tilde{\chi}_1^\pm$ and $\tilde{\chi}_2^0$ masses increase

[5] We use $A_T = \mu/\tan\beta$ as it gives the smallest stop splitting. This is not relevant to this analysis (as we ignore all but the first generation of squarks) but is used for consistency with other CDF analyses.

[6] We use $M_{H_A} = 500$ GeV/c^2 to remove any possibility of decay to Higgs. Any value > 100 GeV/c^2 would be acceptable.

with $|\mu|$, resulting in small production cross sections. We thus only study $|\mu| < 1000$ GeV/c^2. As discussed in Section 2.3, large $\tilde{q}$ masses reduce the t-channel production mechanism, thus increasing the overall $\tilde{\chi}_1^{\pm}\tilde{\chi}_2^0$ production cross section. However, since the $\widetilde{\ell}$ masses are determined mainly by the difference in $\tilde{q}$ and $\tilde{g}$ masses (Equation 2.2), increasing the $\tilde{q}$ mass yields heavier $\widetilde{\ell}$. That in turn reduces the branching ratio to leptons. The reduction in branching ratio is a larger effect than the increase of production cross section. We thus want to keep the $\tilde{q}$ to $\tilde{g}$ mass ratio less than 2. Finally, if the squarks are too much lighter than the gluinos, the renormalization group equations (Equation 2.2) break down. These formulae are useful for $M_{\tilde{q}}/M_{\tilde{g}} > 0.90$. When the squarks are lighter than the gluinos, the sleptons are lighter than the $\tilde{\chi}_1^{\pm}$ and $\tilde{\chi}_2^0$. This results in two-body decays of the $\tilde{\chi}_1^{\pm}$ and $\tilde{\chi}_2^0$. However, for $0.90 < M_{\tilde{q}}/M_{\tilde{g}} \lesssim 0.95$ the lightest slepton is a sneutrino and invisible decays of the $\tilde{\chi}_1^{\pm}$ and $\tilde{\chi}_2^0$ dominate. $M_{\tilde{\chi}_1^{\pm}}$ and $M_{\tilde{\chi}_2^0}$ are mainly functions of $M_{\tilde{g}}$ so we set $M_{\tilde{g}}$ to values that yield 45 GeV/c$^2 \lesssim M_{\tilde{\chi}_1^{\pm}} \lesssim 100$ GeV/c^2.

To summarize, we search the SiMSSM parameter space in the regions

- -200 GeV/c$^2 \leq \mu \leq$ -1000 GeV/c^2,
- $1.1 \leq \tan\beta \leq 8$,
- $0.95 \leq M_{\tilde{q}}/M_{\tilde{g}} \leq 2$, and
- 150 GeV/c$^2 \leq M_{\tilde{g}} \leq 340$ GeV/c^2.

Our limits for the SiMSSM parameter space outside these regions are weaker and thus less interesting. For all points we examine we find $M_{\tilde{\chi}_1^{\pm}} \approx M_{\tilde{\chi}_2^0} \approx 2\ M_{\tilde{\chi}_1^0}$.

In Figures 5.5-5.16 we present the 95% Confidence Level (C.L.) upper limit curve and compare it to the predicted cross section times branching ratio for a variety of points in SiMSSM space. The 95% C.L. upper limit curve is a line indicating the minimum cross section times branching ratio we can detect as a function of $\tilde{\chi}_1^{\pm}$ mass[7]. Above the line enough events would be produced so we could detect them; below it we cannot. This line is the right hand side of Equation 5.1. The cross section times branching ratio lines are calculated using ISAJET 7.20 and are the production cross section for $p\bar{p} \rightarrow \tilde{\chi}_1^{\pm}\tilde{\chi}_2^0$ times the branching ratio $\tilde{\chi}_1^{\pm}\tilde{\chi}_2^0 \rightarrow 3\ell + X$, where ℓ is either e or μ. It is important to realize the branching ratio is the sum of all four possible e or μ combinations (eee, $ee\mu$, $e\mu\mu$, $\mu\mu\mu$). Figure 5.5 shows the 95% C.L. upper limit curve (solid line) in comparison to cross section times branch ratio curves (dashed lines) for $M_{\tilde{q}}/M_{\tilde{g}} = 1$, 1.2, 1.5 and 2.0. The mass lower limit and $\sigma_{\tilde{\chi}_1^{\pm}\tilde{\chi}_2^0}\cdot\mathrm{BR}(\tilde{\chi}_1^{\pm}\tilde{\chi}_2^0 \rightarrow 3\ell + X)$ upper limit can be read off the graph where the dashed and solid lines intersect. Clearly, as the squarks become heavier than the gluinos, the limit degrades.

[7] The 95% indicates we would detect events in 95 experiments out of 100 performed; it does not mean we are 95% sure about our result.

For the case where $M_{\tilde{q}}/M_{\tilde{g}} = 0.95$ we have two-body decays of the $\tilde{\chi}_1^{\pm}$ and $\tilde{\chi}_2^0$, so the acceptances are somewhat different. Figure 5.6 shows we set no limit for $M_{\tilde{q}}/M_{\tilde{g}} = 0.95$. Figure 5.7 is the lower limit on $M_{\tilde{\chi}_1^{\pm}}$ as a function of $M_{\tilde{q}}/M_{\tilde{g}}$. For all of these points we hold both $\tan\beta$ and μ constant and set them to 2 and -400 GeV/c^2, respectively. We also compare our $\sigma_{\tilde{\chi}_1^{\pm}\tilde{\chi}_2^0}\cdot\mathrm{BR}(\tilde{\chi}_1^{\pm}\tilde{\chi}_2^0 \to 3\ell + X)$ limit to that of D0 [46][8]. Their limit is weaker than ours for two reasons: they have somewhat poorer muon detection abilities, and use a higher P_T threshold for all of their leptons. It is very important to realize that every experiment makes slightly different assumptions about models and so limits cannot always be easily compared. D0 only examines SUGRA models (see below for that comparison).

Figure 5.8 compares the 95 % C.L. line to a variety of μ values: -200, -400 and -800 GeV/c^2. For this plot we set $\tan\beta = 2$ and $M_{\tilde{q}}/M_{\tilde{g}} = 2$. Recall that $|\mu|$ is the unmixed Higgsino mass, so as μ increases the Higgsino content of the $\tilde{\chi}_1^{\pm}$ and $\tilde{\chi}_2^0$ will decrease. However, as $|\mu|$ gets large, the masses of the $\tilde{\chi}_1^{\pm}$ and $\tilde{\chi}_2^0$ tends to increase. This decreases the production cross section, reducing our limit. This can be seen in Figure 5.8. Figure 5.9 is the lower limit on $M_{\tilde{\chi}_1^{\pm}}$ as a function of μ. For comparison, we indicate the ALEPH limit [47]. It is important to note that the ALEPH limit includes searches for hadronic final states of the $\tilde{\chi}_1^{\pm}$ and $\tilde{\chi}_2^0$, as well as the leptonic signature we use. Also, the LEP experiments (since LEP in an e^+e^- machine) are more sensitive to low values of $|\mu|$ while Tevatron experiments are more sensitive to high values of $|\mu|$. As with the D0 limit, ALEPH makes somewhat different model assumptions. They examine only SUGRA, which (see below) favors low $|\mu|$ values. However, their kinematic limit is quite model independent and can be compared with our limit.

Having varied both $M_{\tilde{q}}/M_{\tilde{g}}$ and μ, we now vary $\tan\beta$. Since the acceptance changes with $\tan\beta$, each 95% C.L. curve is on a separate plot. We show plots for $\tan\beta$ =1.1, 1.5, 2, 4 and 8. For these points we set $M_{\tilde{q}}/M_{\tilde{g}}$ and μ to 1 and -400 GeV/c^2, respectively. Figures 5.10-5.14 show the individual $\sigma \cdot BR$ plots for each $\tan\beta$ point and Figure 5.15 summarizes the lower limit on $M_{\tilde{\chi}_1^{\pm}}$ as a function of $\tan\beta$. As expected, the limit decreases as $\tan\beta$ increases.

We have also examined the $\tilde{\chi}_1^{\pm}$ mass limit for high $\tilde{q}$ mass. This region is interesting since, as mentioned above, the t-channel virtual $\tilde{q}$ exchange interferes destructively with the s-channel $W^{\pm}$ exchange. Regions of high $\tilde{q}$ mass effectively turn off t-channel production. Figure 5.16 shows the limit on $M_{\tilde{\chi}_1^{\pm}}$ for $M_{\tilde{q}} = 500$ GeV/c^2. For this plot we fix $M_{\tilde{q}}$ and allow $M_{\tilde{g}}$ to vary freely. Again, high $\tilde{q}$ masses lead to high $\tilde{\ell}$ masses, which lead to somewhat degraded limits.

Tables 5.2-5.6 list the input ($M_{\tilde{q}}$, $M_{\tilde{g}}$, $\tan\beta$ and μ) and the relevant output parameters ($M_{\tilde{\chi}_1^0}$, $M_{\tilde{\chi}_2^0}$, $M_{\tilde{\chi}_1^{\pm}}$, $M_{\tilde{\ell}_L}$, $M_{\tilde{\nu}_L}$, $M_{\tilde{\ell}_R}$ and the branching ratios to leptons) for each point examined in SiMSSM

[8] D0 plots their limit for an average branching ratio to leptons; we use a sum of branching ratios to e or μ. Thus, their result is scaled by a factor of 4 for comparison with ours.

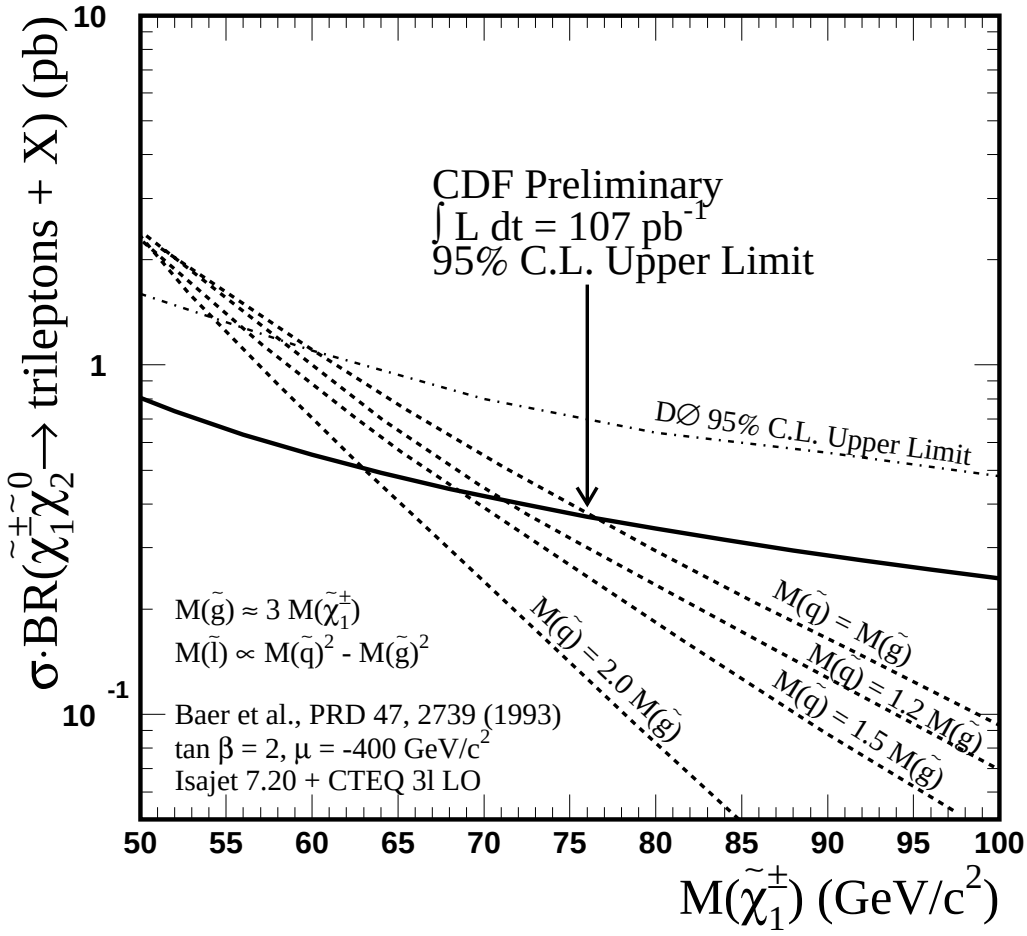

Figure 5.5: Production cross section times branching ratio to leptons (e or μ) for $\tilde{\chi}_1^{\pm}\tilde{\chi}_2^0$ production as a function of $\tilde{\chi}_1^{\pm}$ mass for $\tan\beta = 2$, and $\mu = -400$ GeV/c^2. The dashed lines are the theoretical prediction and the solid line is the 95% Confidence Level limit (using the fit to all $\tan\beta = 2$ points). We use ISAJET 7.20 with the CTEQ 3L structure functions to generate the Monte Carlo. As expected, the limit worsens as the squarks become much heavier than the gluinos. For comparison, we indicate the D0 95% C.L. limit [46].

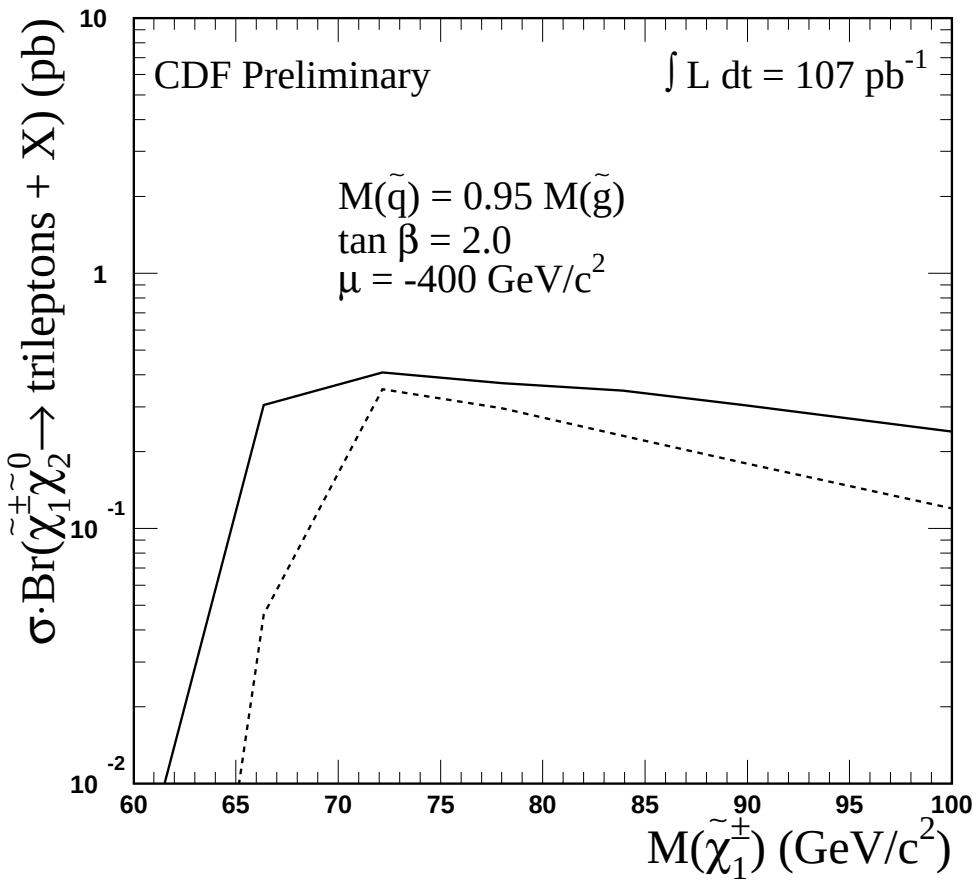

Figure 5.6: Production cross section times branching ratio to leptons (e or μ) for $\tilde{\chi}_1^{\pm}\tilde{\chi}_2^0$ production as a function of $\tilde{\chi}_1^{\pm}$ mass for $\tan\beta = 2$, $\mathrm{M}_{\tilde{q}}/\mathrm{M}_{\tilde{g}} = 0.95$ and $\mu = -400$ GeV/c^2. The dashed line is the theoretical prediction and the solid line is the 95% Confidence Level limit. We use ISAJET 7.20 with the CTEQ 3L structure functions to generate the Monte Carlo. We do not set a mass limit at this point; at low chargino masses the sneutrino is lighter than the sleptons so invisible decays dominate.

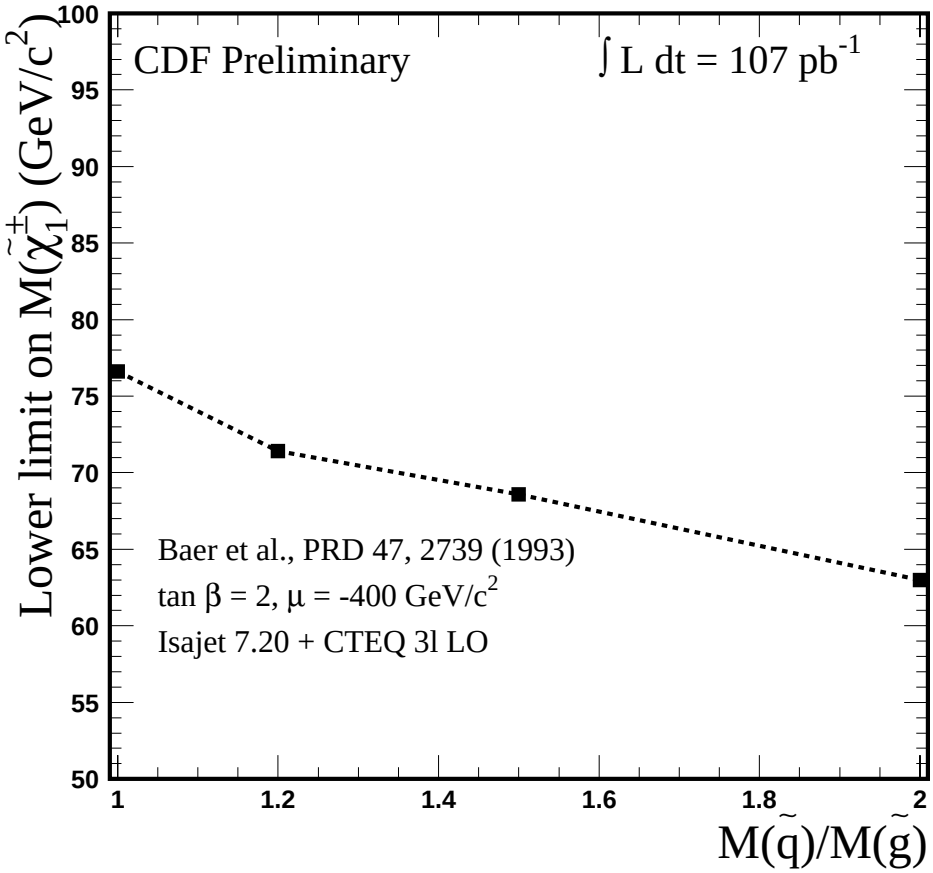

Figure 5.7: Limit on $M_{\tilde{\chi}_1^\pm}$ as a function of $M_{\tilde{q}}/M_{\tilde{g}}$. The limit decreases as the $\tilde{q}$s become much more massive than the $\tilde{g}$s since the $\widetilde{\ell}$ masses depend on the difference between them. Heavier $\widetilde{\ell}$s lead to fewer decays via virtual $\widetilde{\ell}$s and thus a smaller branching ratio to leptons.

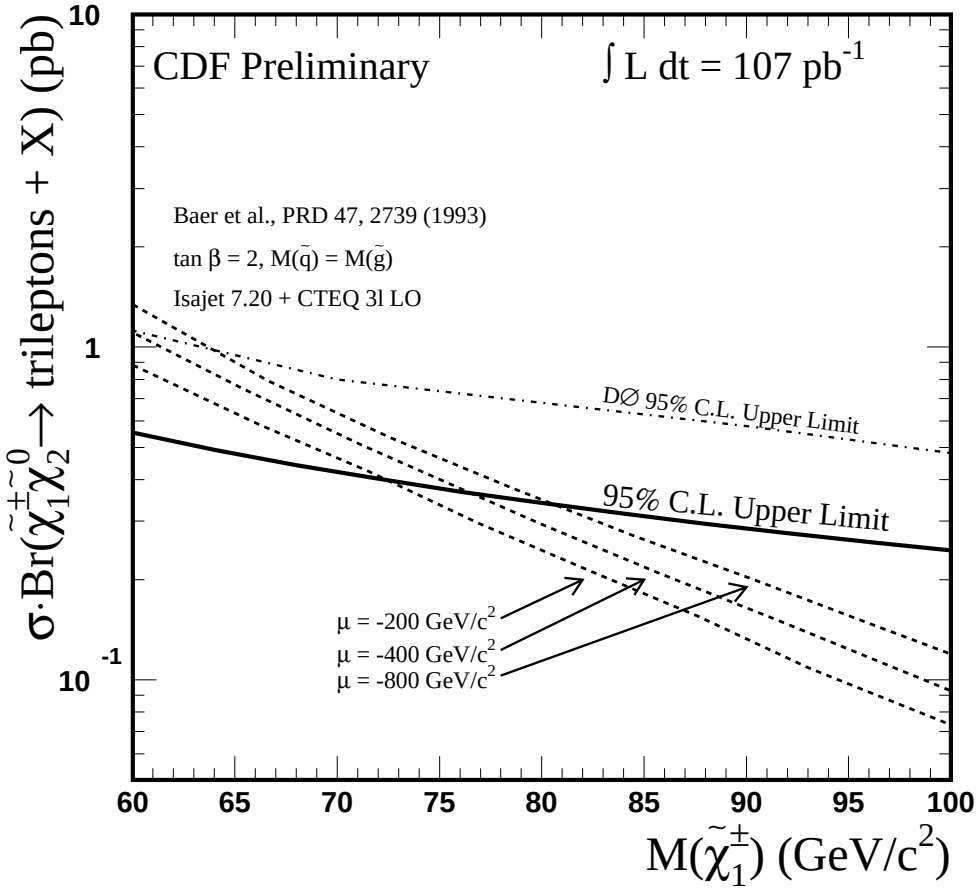

Figure 5.8: Production cross section times branching ratio to leptons (e or μ) for $\tilde{\chi}_1^{\pm}\tilde{\chi}_2^0$ production as a function of $\tilde{\chi}_1^{\pm}$ mass for $\tan\beta = 2$, and $M_{\tilde{q}} = M_{\tilde{g}}$. The dashed lines are the theoretical prediction and the solid line is the 95% Confidence Level limit (using the fit to all $\tan\beta = 2$ points). We use ISAJET 7.20 with the CTEQ 3L structure functions to generate the Monte Carlo. For comparison, we indicate the D0 95% C.L. limit [46].

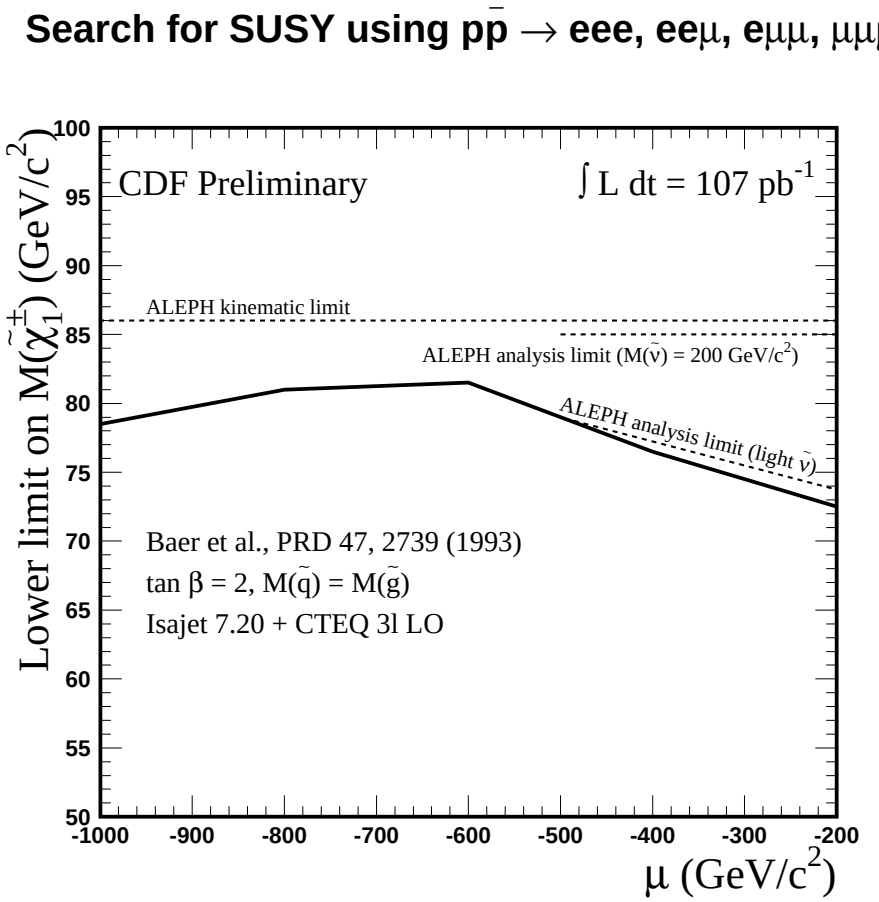

Figure 5.9: The solid curve is the limit on $M_{\tilde{\chi}_1^{\pm}}$ as a function of μ. The maximum limit is 81.5 GeV/c^2 , for μ = -600 GeV/c^2. For comparison, we show the ALEPH limit (dashed lines) [47]. The kinematic limit is half the LEP-II center-of-mass energy. It is important to realize that ALEPH searches for several final states, not only the trilepton state searched for in this analysis. Just as the s- and t-channels interfere at the Tevatron, so do they at LEP (where the production mechanism is via virtual sneutrino exchange). Thus, higher $\tilde{\nu}$ masses result in higher production cross sections, but since ALEPH searches for all possible final states, they do not have the degradation in branching ratio we do. For the best comparison, we include the ALEPH limit for light $\tilde{\nu}$. Also, ALEPH only examines SUGRA, which tends to keep $|\mu| < 500$ GeV/c^2.

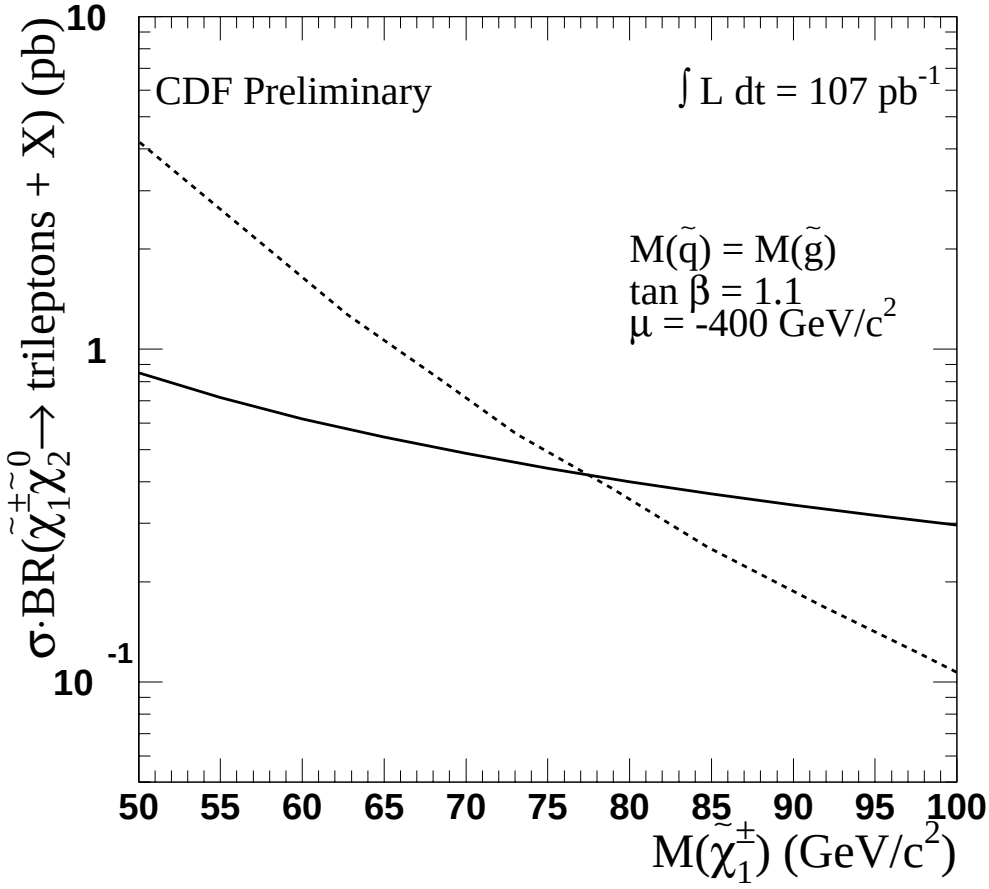

Figure 5.10: Production cross section times branching ratio to leptons (e or μ) for $\tilde{\chi}_1^{\pm}\tilde{\chi}_2^0$ production as a function of $\tilde{\chi}_1^{\pm}$ mass for $\tan\beta = 1.1$, $\mathrm{M}(\tilde{q}) = \mathrm{M}(\tilde{g})$ and $\mu = -400$ GeV/c^2. The dashed line is the theoretical prediction and the solid line is the 95% Confidence Level limit. We use ISAJET 7.20 with the CTEQ 3L structure functions to generate the Monte Carlo.

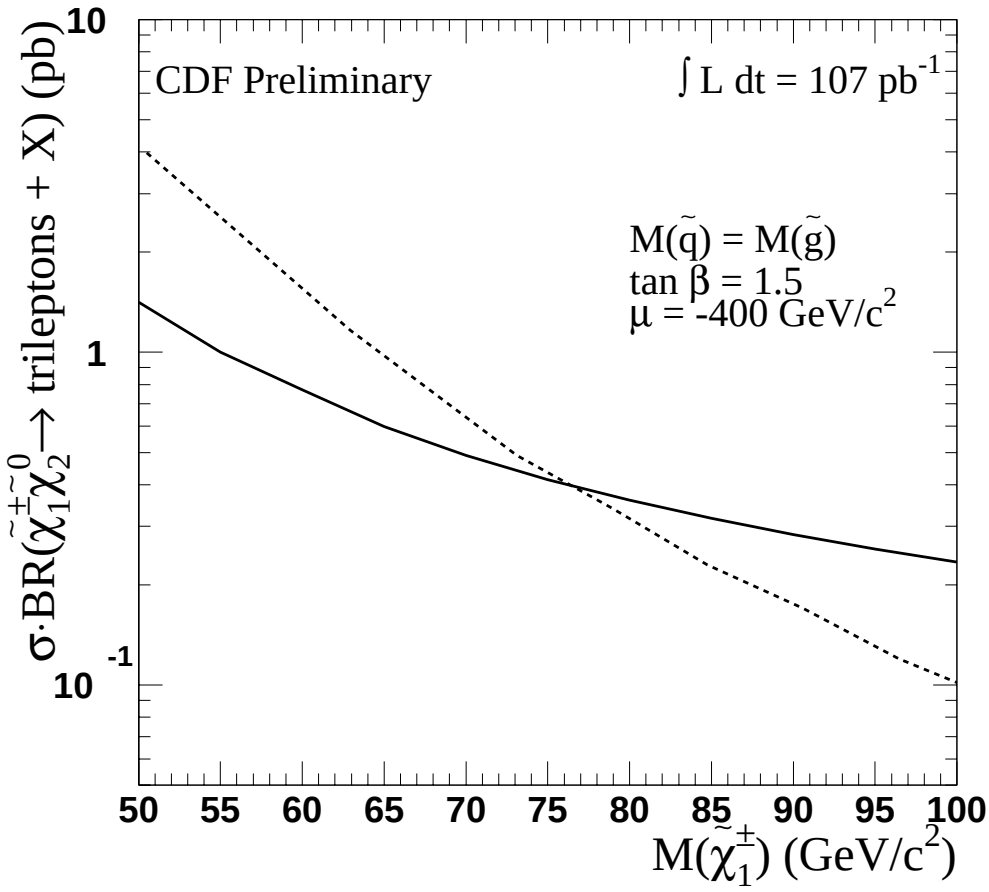

Figure 5.11: Production cross section times branching ratio to leptons (e or μ) for $\tilde{\chi}_1^{\pm}\tilde{\chi}_2^0$ production as a function of $\tilde{\chi}_1^{\pm}$ mass for $\tan\beta = 1.5$, $\mathrm{M}(\tilde{q}) = \mathrm{M}(\tilde{g})$ and $\mu = -400$ GeV/c^2. The dashed line is the theoretical prediction and the solid line is the 95% Confidence Level limit. We use ISAJET 7.20 with the CTEQ 3L structure functions to generate the Monte Carlo.

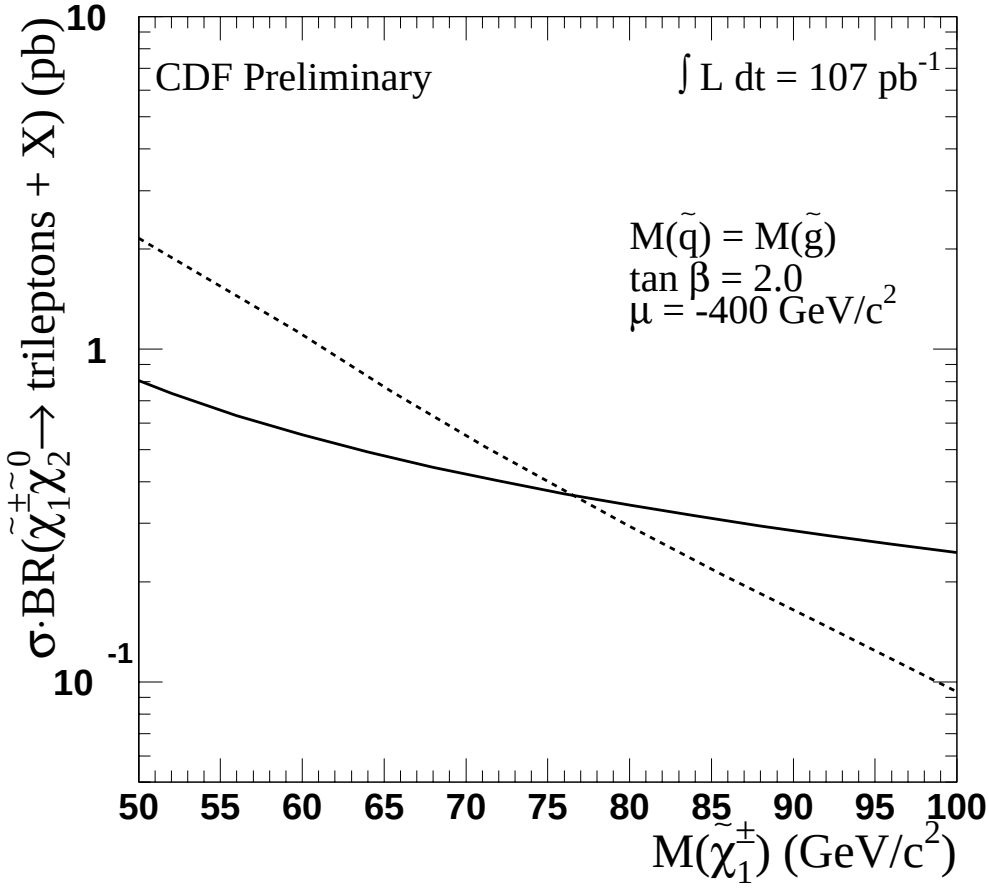

Figure 5.12: Production cross section times branching ratio to leptons (e or μ) for $\tilde{\chi}_1^{\pm}\tilde{\chi}_2^0$ production as a function of $\tilde{\chi}_1^{\pm}$ mass for $\tan\beta = 2$, $\mathrm{M}(\tilde{q}) = \mathrm{M}(\tilde{g})$ and $\mu = -400$ GeV/c^2. The dashed line is the theoretical prediction and the solid line is the 95% Confidence Level limit. We use ISAJET 7.20 with the CTEQ 3L structure functions to generate the Monte Carlo.

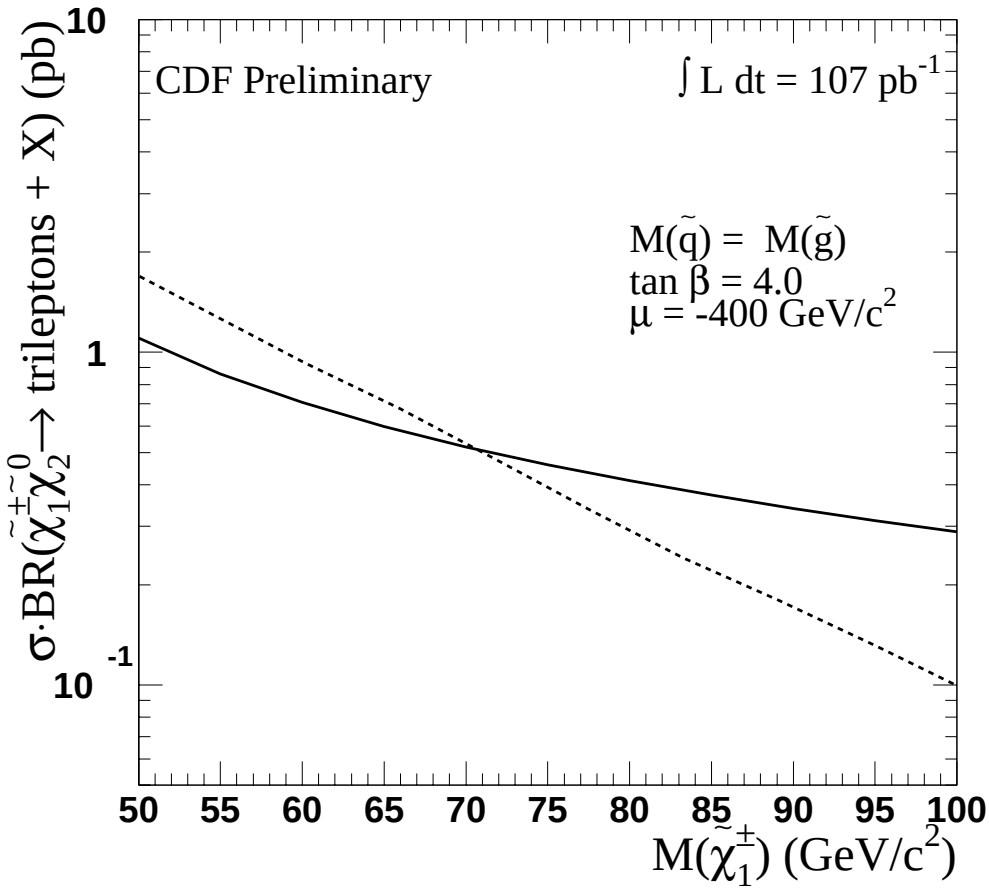

Figure 5.13: Production cross section times branching ratio to leptons (e or μ) for $\tilde{\chi}_1^{\pm}\tilde{\chi}_2^0$ production as a function of $\tilde{\chi}_1^{\pm}$ mass for $\tan\beta = 4$, $\mathrm{M}(\tilde{q}) = \mathrm{M}(\tilde{g})$ and $\mu = -400$ GeV/c^2. The dashed line is the theoretical prediction and the solid line is the 95% Confidence Level limit. We use ISAJET 7.20 with the CTEQ 3L structure functions to generate the Monte Carlo.

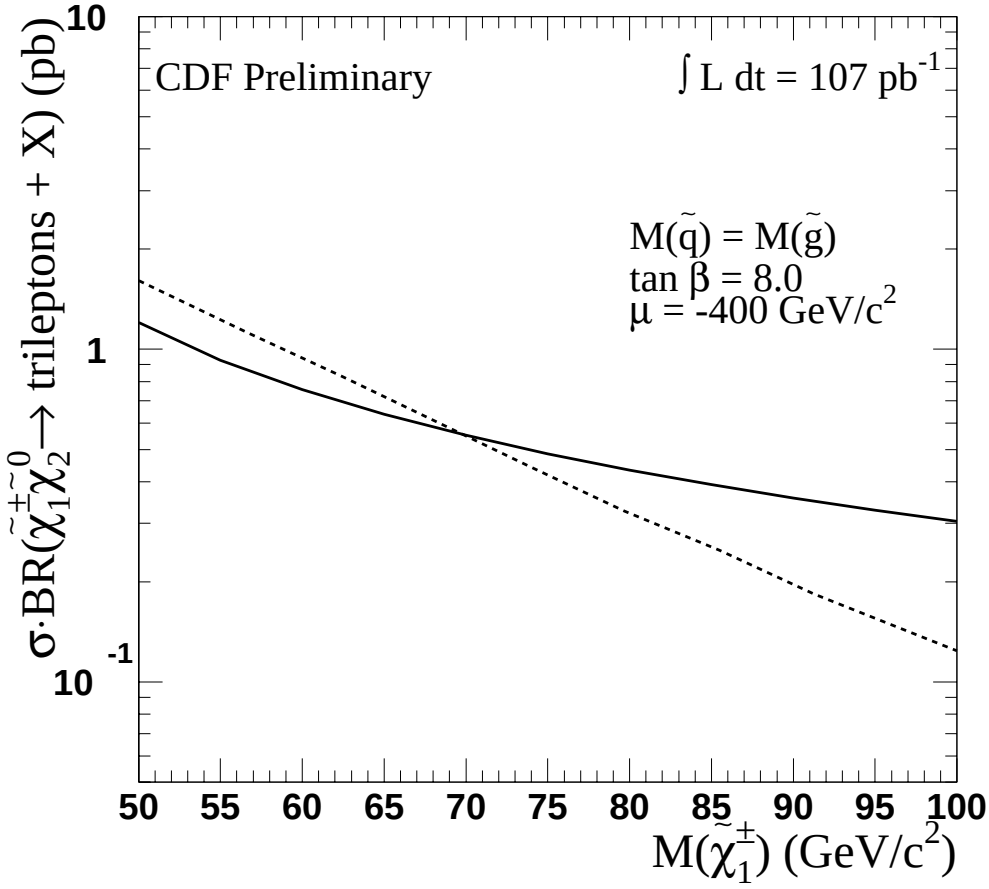

Figure 5.14: Production cross section times branching ratio to leptons (e or μ) for $\tilde{\chi}_1^{\pm}\tilde{\chi}_2^0$ production as a function of $\tilde{\chi}_1^{\pm}$ mass for $\tan\beta = 8$, $\mathrm{M}(\tilde{q}) = \mathrm{M}(\tilde{g})$ and $\mu = -400$ GeV/c^2. The dashed line is the theoretical prediction and the solid line is the 95% Confidence Level limit. We use ISAJET 7.20 with the CTEQ 3L structure functions to generate the Monte Carlo.

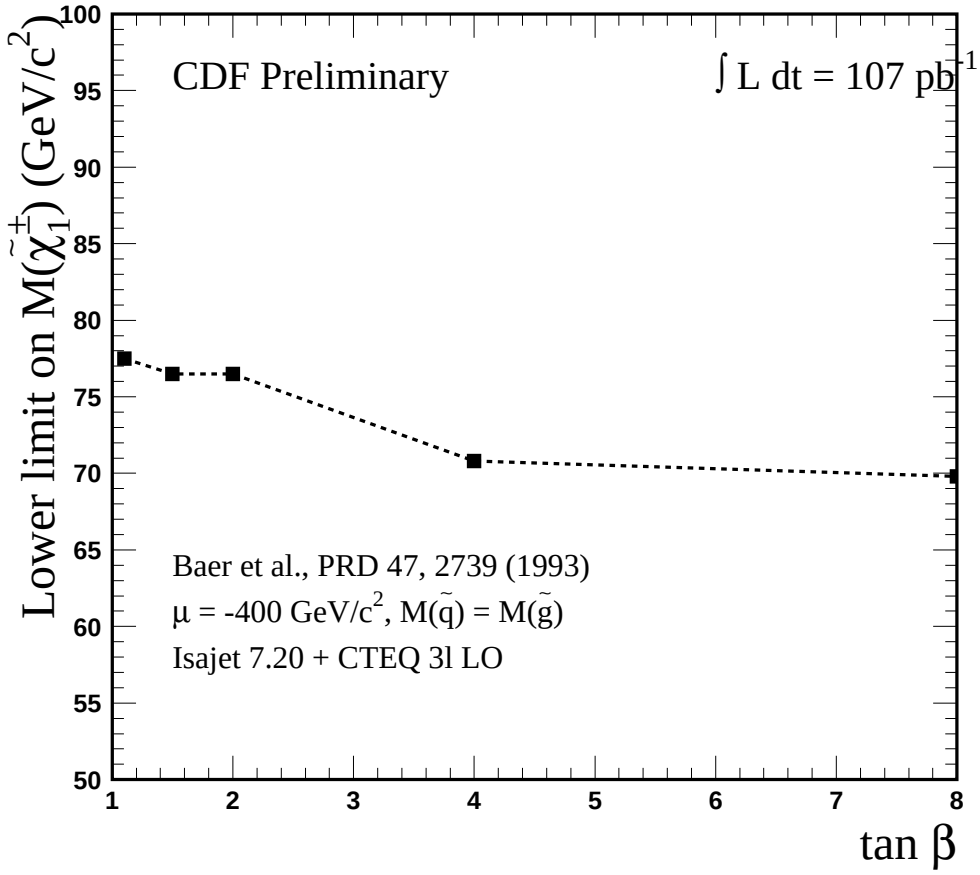

Figure 5.15: Lower limit on $\mathrm{M}(\tilde{\chi}_1^{\pm})$ as a function of $\tan\beta$ for, $\mathrm{M}(\tilde{q}) = \mathrm{M}(\tilde{g})$ and $\mu = -400$ GeV/c^2. As expected, the limit decreases as $\tan\beta$ increases.

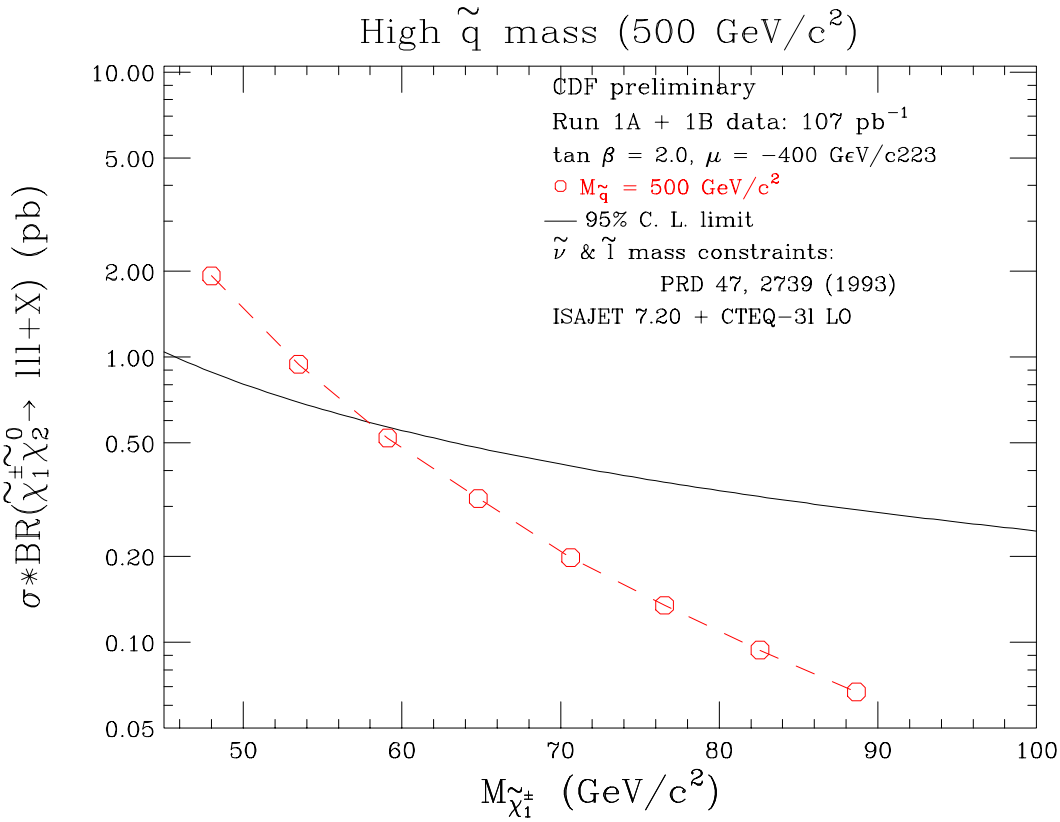

Figure 5.16: Production cross section times branching ratio to leptons (e or μ) for $\tilde{\chi}_1^{\pm}\tilde{\chi}_2^0$ production as a function of $\tilde{\chi}_1^{\pm}$ mass for $\tan\beta = 2$ and $\mu = -400$ GeV/c^{2}and $M_{\tilde{q}} = 500$ GeV/c^2. The dashed line is the theoretical prediction and the solid line is the 95% Confidence Level limit (using the fit to all $\tan\beta = 2$ points). We use ISAJET 7.20 with the CTEQ 3L structure functions to generate the Monte Carlo.

Table 5.2: Input and output parameters for the SiMSSM points scanned. All masses are in GeV/c^2 and all σ are in picobarns.

	Input		Output										
Set	$\tilde{q}$	$\tilde{g}$	$\tilde{\chi}_1^0$	$\tilde{\chi}_2^0$	$\tilde{\chi}_1^\pm$	$\widetilde{\ell}_L$	$\widetilde{\nu}$	$\widetilde{\ell}_R$	BR$\to\ell\ell$	BR$\to\ell\nu$	BR$\to 3\ell$	σ	$\sigma\cdot$BR
	(GeV/c^2)		(GeV/c^2)						$\tilde{\chi}_2^0$	$\tilde{\chi}_1^\pm$	Total		
$M_{\tilde{q}} \simeq M_{\tilde{g}}$, $\mu = -400$ GeV/c^2, $\tan\beta = 2.0$													
14.1	180	179	26.7	60.7	59.7	101.8	80.7	92.6	0.321	0.461	0.148	7.66	1.13
11	200	199	29.7	66.3	65.4	111.5	92.7	101.3	0.348	0.433	0.151	4.98	0.75
12	199	200	29.9	66.7	65.8	108.4	88.9	97.7	0.331	0.455	0.151	4.80	0.72
14.2	220	219	32.7	71.9	71.1	121.4	104.4	110.2	0.364	0.409	0.149	3.42	0.51
13	250	249	37.3	80.5	79.8	136.3	121.4	123.6	0.377	0.377	0.142	2.09	0.30
14	249	250	37.5	80.9	80.2	133.1	117.8	120.0	0.370	0.393	0.145	2.03	0.30
14.3	270	269	40.3	86.3	85.7	146.4	132.6	132.7	0.381	0.359	0.137	1.53	0.21
14.4	290	289	43.3	92.1	91.5	156.4	143.6	141.8	0.384	0.342	0.131	1.15	0.15
14.5	310	309	46.4	97.9	97.4	166.6	154.6	150.9	0.384	0.326	0.125	0.88	0.11
High $M_{\tilde{q}}$ ($M_{\tilde{q}} = 500$ GeV/c^2), $\mu = -400$ GeV/c^2, $\tan\beta = 2.0$													
15	500	160	20.5	49.2	48.0	482.4	478.4	480.8	0.212	0.222	0.047	41.08	1.93
16	500	180	23.4	54.6	53.5	477.2	473.1	475.3	0.198	0.222	0.044	21.50	0.94
17	500	200	26.4	60.1	59.1	471.3	467.2	469.0	0.187	0.222	0.041	12.58	0.52
18	500	220	29.4	65.7	64.8	464.8	460.6	462.0	0.178	0.222	0.039	8.11	0.32
19	500	240	32.5	71.4	70.6	457.5	453.3	454.1	0.171	0.221	0.038	5.23	0.20
19.1	500	260	35.6	77.2	76.6	449.4	445.1	445.4	0.166	0.221	0.037	2.61	0.09
19.2	500	280	38.7	83.2	82.6	440.6	436.2	435.9	0.163	0.221	0.036	3.67	0.13
19.3	500	300	41.8	89.2	88.6	430.9	426.4	425.4	0.162	0.221	0.036	1.87	0.07
$M_{\tilde{q}} = 1.2M_{\tilde{g}}$, $\mu = -400$ GeV/c^2, $\tan\beta = 2.0$													
34.1	180	150	21.7	51.5	50.3	131.6	116.1	126.5	0.421	0.292	0.122	23.96	2.94
30	240	200	29.1	65.0	64.1	172.5	161.0	166.0	0.418	0.261	0.109	6.40	0.70
31	264	220	32.0	70.5	69.7	189.0	178.5	181.9	0.411	0.253	0.104	4.37	0.45
32	276	230	33.5	73.3	72.5	197.3	187.3	189.9	0.407	0.249	0.102	3.68	0.37
33	288	240	34.9	76.0	75.3	205.5	196.0	197.9	0.403	0.246	0.099	3.16	0.31
34	312	260	37.9	81.6	81.0	222.1	213.3	213.9	0.392	0.241	0.094	2.34	0.22
34.2	336	280	40.8	87.2	86.6	238.8	230.6	230.0	0.379	0.237	0.090	1.85	0.17
34.3	360	300	43.7	92.8	92.3	255.4	247.8	246.1	0.363	0.233	0.084	1.31	0.11

space.

5.4 Limits on other models

The limits we set above are rather general. We can also examine somewhat more specific models and set limits on them. We examine two models: a SU(5)×U(1) Supergravity model and a somewhat more general supergravity model known simply as SUGRA.

5.4.1 SU(5)×U(1) Supergravity model

The string-derived SU(5) × U(1) one parameter supergravity model [48] predicts

Table 5.3: Input and output parameters for the SiMSSM points scanned. All masses are in GeV/c^2 and all σ are in picobarns.

	Input		Output										
Set	$\tilde{q}$	$\tilde{g}$	$\tilde{\chi}_1^0$	$\tilde{\chi}_2^0$	$\tilde{\chi}_1^\pm$	$\tilde{\ell}_L$	$\tilde{\nu}$	$\tilde{\ell}_R$	BR$\to\ell\ell$	BR$\to\ell\nu$	BR$\to 3\ell$	σ	$\sigma\cdot$BR
	(GeV/c^2)		(GeV/c^2)						$\tilde{\chi}_2^0$	$\tilde{\chi}_1^\pm$	Total		
$M_{\tilde{q}} = 1.5 M_{\tilde{g}}$, $\mu = -400$ GeV/c^2, $\tan\beta = 2.0$													
39.1	225	150	21.1	50.4	49.1	188.5	178.1	185.0	0.407	0.237	0.096	31.04	3.00
35	270	180	25.3	58.1	57.1	224.9	216.2	220.9	0.394	0.231	0.091	12.52	1.14
36	300	200	28.2	63.4	62.5	249.3	241.5	244.8	0.379	0.228	0.086	8.19	0.71
37	315	210	29.6	66.1	65.2	261.5	254.0	256.9	0.369	0.227	0.084	6.73	0.56
38	330	220	31.0	68.7	67.9	273.7	266.6	268.9	0.359	0.226	0.081	5.68	0.46
39	360	240	33.9	74.1	73.3	298.2	291.7	293.0	0.332	0.225	0.075	4.08	0.30
39.2	405	270	38.1	82.1	81.5	334.9	329.1	329.1	0.283	0.223	0.063	2.75	0.17
39.3	450	300	42.4	90.3	89.8	371.7	366.5	365.3	0.227	0.222	0.050	1.57	0.08
$M_{\tilde{q}} \simeq M_{\tilde{g}}$, $\mu = -200$ GeV/c^2, $\tan\beta = 2.0$													
214.1	160	159	24.5	62.8	60.9	92.1	68.2	83.8	0.355	0.401	0.142	5.51	0.78
214.2	180	179	27.6	67.8	66.2	101.8	80.7	92.5	0.419	0.364	0.152	3.83	0.58
214.3	200	199	30.7	72.9	71.5	111.5	92.7	101.3	0.444	0.336	0.149	2.83	0.42
214.4	220	219	33.8	78.0	76.9	121.4	104.4	110.2	0.455	0.313	0.142	2.08	0.30
211	240	239	36.9	83.1	82.3	131.3	115.8	119.1	0.456	0.292	0.133	1.61	0.21
212	260	259	40.0	88.3	87.7	141.3	127.0	128.2	0.450	0.274	0.123	1.26	0.16
213	280	279	43.0	93.5	93.1	151.4	138.1	137.2	0.435	0.258	0.112	0.97	0.11
214	300	299	46.1	98.8	98.5	161.5	149.1	146.3	0.411	0.243	0.100	0.77	0.08
$M_{\tilde{q}} \simeq M_{\tilde{g}}$, $\mu = -800$ GeV/c^2, $\tan\beta = 2.0$													
234.1	200	199	28.8	61.1	60.7	111.5	92.7	101.3	0.275	0.540	0.149	9.03	1.34
230	220	219	31.8	66.9	66.6	121.4	104.4	110.2	0.295	0.521	0.153	5.15	0.79
231	240	239	34.8	72.8	72.5	131.3	115.8	119.1	0.308	0.503	0.155	3.47	0.54
232	260	259	37.8	78.7	78.5	141.3	127.0	128.2	0.317	0.485	0.154	2.47	0.38
233	280	279	40.8	84.7	84.5	151.4	138.1	137.2	0.324	0.467	0.151	1.79	0.27
234	300	299	43.8	90.6	90.4	161.5	149.1	146.3	0.329	0.450	0.148	1.35	0.20
234.2	340	319	46.3	95.6	95.5	206.5	197.0	193.3	0.348	0.336	0.117	1.13	0.13
234.3	340	339	49.9	102.1	102.5	181.8	170.9	164.6	0.336	0.416	0.134	0.75	0.10
$M_{\tilde{q}} \simeq M_{\tilde{g}}$, $\mu = -400$ GeV/c^2, $\tan\beta = 1.5$													
15.3	160	159	23.9	57.4	55.9	89.5	74.5	81.3	0.405	0.471	0.191	10.36	1.97
15.2	180	179	26.9	62.9	61.6	99.4	86.1	90.2	0.420	0.443	0.186	6.26	1.16
270	220	219	33.0	74.2	73.1	119.4	108.6	108.3	0.429	0.395	0.169	2.88	0.49
271	240	239	36.1	79.9	78.9	129.5	119.6	117.4	0.429	0.374	0.160	2.13	0.34
272	260	259	39.1	85.6	84.7	139.6	130.5	126.5	0.427	0.356	0.152	1.52	0.23
273	280	279	42.1	91.4	90.6	149.8	141.3	135.7	0.424	0.339	0.144	1.18	0.17
274	300	299	45.2	97.2	96.5	160.0	152.1	144.9	0.421	0.325	0.137	0.91	0.12
15.1	320	319	48.3	103.1	102.4	170.2	162.8	154.1	0.418	0.311	0.130	0.68	0.09

Table 5.4: Input and output parameters for the SiMSSM points scanned. All masses are in GeV/c^2 and all σ are in picobarns.

	Input		Output										
Set	$\tilde{q}$	$\tilde{g}$	$\tilde{\chi}_1^0$	$\tilde{\chi}_2^0$	$\tilde{\chi}_1^\pm$	$\widetilde{\ell}_L$	$\widetilde{\nu}$	$\widetilde{\ell}_R$	BR$\to\ell\ell$	BR$\to\ell\nu$	BR$\to 3\ell$	σ	$\sigma\cdot$BR
	(GeV/c^2)		(GeV/c^2)						$\tilde{\chi}_2^0$	$\tilde{\chi}_1^\pm$	Total		
High $M_{\tilde{q}}$ ($M_{\tilde{q}} = 500$) GeV/c^2, $\mu = -400$ GeV/c^2, $\tan\beta = 1.5$													
277	500	200	26.6	62.4	61.0	471.3	467.2	469.0	0.261	0.222	0.058	10.47	0.61
278	500	220	29.7	68.0	66.8	464.2	461.6	461.5	0.255	0.222	0.057	6.79	0.39
279	500	240	32.7	73.7	72.6	457.0	454.3	453.7	0.250	0.222	0.056	4.57	0.25
$M_{\tilde{q}} \simeq M_{\tilde{g}}$, $\mu = -400$ GeV/c^2, $\tan\beta = 1.1$													
11.4	160	159	24.0	58.8	57.1	85.8	82.2	77.9	0.517	0.476	0.246	8.89	2.19
11.3	180	179	27.0	64.3	62.8	96.0	92.8	87.1	0.507	0.448	0.227	5.58	1.27
11.2	200	199	30.1	69.9	68.5	106.3	103.4	96.4	0.496	0.422	0.209	3.85	0.81
280	220	219	33.1	75.5	74.3	116.6	114.0	105.7	0.488	0.398	0.194	2.86	0.56
281	240	239	36.2	81.2	80.1	126.9	124.5	115.0	0.478	0.377	0.180	2.12	0.38
282	260	259	39.3	87.0	85.9	137.3	135.1	124.3	0.469	0.359	0.168	1.51	0.25
283	280	279	42.3	92.7	91.8	147.6	145.5	133.7	0.457	0.342	0.156	1.08	0.17
284	300	299	45.4	98.6	97.7	158.0	156.0	143.0	0.446	0.328	0.146	0.83	0.12
11.1	320	319	48.4	104.4	103.6	168.3	166.5	152.3	0.434	0.315	0.137	0.64	0.09
$M_{\tilde{q}} \simeq M_{\tilde{g}}$, $\mu = -1000$ GeV/c^2, $\tan\beta = 2$													
1k.2	220	219	31.5	65.7	65.5	121.3	104.3	110.1	0.278	0.554	0.154	5.72	0.88
1k.3	240	239	34.5	71.6	71.5	131.3	115.7	119.1	0.293	0.538	0.157	3.87	0.61
1k.4	260	259	37.5	77.6	77.4	141.3	127.0	128.1	0.303	0.522	0.158	2.64	0.41
1k.5	280	279	40.5	83.6	83.4	151.4	138.1	137.2	0.311	0.506	0.157	1.85	0.29
1k.6	300	299	43.5	89.6	89.4	161.5	149.1	146.3	0.316	0.490	0.155	1.41	0.21
1k.7	320	319	46.5	95.6	95.4	171.6	160.0	155.4	0.321	0.474	0.152	1.05	0.16
1k.8	340	339	49.6	101.6	101.5	181.8	170.9	164.6	0.324	0.458	0.148	0.77	0.11
$M_{\tilde{q}} \simeq M_{\tilde{g}}$, $\mu = -600$ GeV/c^2, $\tan\beta = 2$													
600.1	200	199	29.1	62.9	62.4	111.5	92.7	101.2	0.301	0.496	0.149	6.79	1.02
600.2	220	219	32.1	68.7	68.2	121.3	104.3	110.1	0.319	0.474	0.151	4.54	0.68
600.3	240	239	35.1	74.5	74.1	131.3	115.7	119.1	0.331	0.453	0.150	3.10	0.46
600.4	260	259	38.1	80.4	80.0	141.3	127.0	128.1	0.339	0.433	0.147	2.16	0.31
600.5	280	279	41.1	86.3	85.9	151.4	138.1	137.2	0.345	0.415	0.143	1.56	0.22
600.6	300	299	44.2	92.2	91.9	161.5	149.1	146.3	0.348	0.397	0.138	1.19	0.16
600.7	320	319	47.2	98.2	97.9	171.6	160.0	155.4	0.351	0.380	0.133	0.90	0.12
600.8	340	339	50.3	104.1	103.9	181.8	170.9	164.6	0.353	0.364	0.128	0.68	0.08

Table 5.5: Input and output parameters for the SiMSSM points scanned. All masses are in GeV/c^2 and all σ are in picobarns. Note that the $\tilde{\chi}_2^0$ branching ratio is quite small for the cases where the $\tilde{q}$ is lighter than the $\tilde{g}$.

	Input		Output										
Set	$\tilde{q}$ (GeV/c^2)	$\tilde{g}$	$\tilde{\chi}_1^0$	$\tilde{\chi}_2^0$	$\tilde{\chi}_1^\pm$	$\widetilde{\ell}_L$	$\widetilde{\nu}$	$\widetilde{\ell}_R$	BR$\to\ell\ell$ $\tilde{\chi}_2^0$	BR$\to\ell\nu$ $\tilde{\chi}_1^\pm$	BR$\to 3\ell$ Total	σ	$\sigma\cdot$BR
			(GeV/c^2)										
$M_{\tilde{q}} = 2M_{\tilde{g}}$, $\mu = -400$ GeV/c^2, $\tan\beta = 2$													
20.1	300	150	20.3	48.9	47.7	273.7	266.6	271.2	0.359	0.224	0.080	39.52	3.18
20.2	340	170	23.0	53.9	52.8	309.5	303.3	306.9	0.336	0.223	0.074	21.38	1.60
20.3	380	190	25.7	58.9	57.9	345.5	339.9	342.6	0.302	0.222	0.067	13.15	0.88
20.4	420	210	28.5	64.0	63.1	381.5	376.4	378.3	0.259	0.222	0.057	8.63	0.49
20.5	460	230	31.2	69.1	68.3	417.5	412.9	414.1	0.213	0.221	0.047	6.04	0.28
20.6	500	250	34.0	74.3	73.5	453.5	449.3	449.8	0.168	0.221	0.037	4.39	0.16
20.7	540	270	36.7	79.5	78.8	489.6	485.6	485.6	0.128	0.221	0.028	3.27	0.09
$M_{\tilde{q}} \sim M_{\tilde{g}}$, $\mu = -400$ GeV/c^2, $\tan\beta = 4$													
4.8	160	159	23.0	49.2	48.9	95.5	59.0	87.0	0.090	0.606	0.055	29.56	1.62
4.2	200	199	28.9	60.4	60.2	114.3	86.2	103.9	0.204	0.539	0.110	8.44	0.93
4.3	220	219	31.8	66.1	65.9	123.9	98.6	112.6	0.237	0.514	0.122	5.56	0.68
4.4	240	239	34.8	71.8	71.7	133.7	110.6	121.4	0.261	0.492	0.128	3.74	0.48
4.5	260	259	37.8	77.6	77.5	143.6	122.3	130.2	0.278	0.471	0.131	2.58	0.34
4.6	280	279	40.8	83.4	83.3	153.5	133.8	139.2	0.290	0.450	0.131	1.84	0.24
4.7	300	299	43.8	89.2	89.1	163.5	145.1	148.2	0.298	0.429	0.128	1.40	0.18
4.10	320	319	46.8	95.0	955.0	173.5	156.3	157.2	0.304	0.408	0.124	1.06	0.13
4.11	340	339	49.8	100.9	100.9	183.5	167.4	166.3	0.306	0.387	0.118	0.80	0.10
$M_{\tilde{q}} \sim M_{\tilde{g}}$, $\mu = -400$ GeV/c^2, $\tan\beta = 8$													
8.1	180	179	25.9	51.0	51.0	105.8	70.6	96.2	0.100	0.637	0.064	23.54	1.51
8.2	200	199	28.1	56.7	56.7	115.2	84.0	104.7	0.144	0.627	0.090	12.45	1.12
8.3	220	219	31.0	62.4	62.4	124.8	96.7	113.3	0.178	0.616	0.110	7.58	0.83
8.5	260	259	36.9	73.8	73.9	144.2	120.8	130.9	0.224	0.596	0.133	3.34	0.45
8.6	280	279	39.9	79.6	79.7	154.1	132.5	139.8	0.238	0.584	0.139	2.34	0.33
8.7	300	299	42.9	85.4	85.5	164.0	143.9	148.7	0.249	0.570	0.142	1.75	0.25
8.9	320	319	45.9	91.3	91.3	174.0	155.2	157.7	0.256	0.552	0.141	1.30	0.18
8.10	340	339	48.9	97.1	97.1	184.1	166.4	166.8	0.260	0.530	0.138	0.97	0.13
$M_{\tilde{q}} = 0.9\ M_{\tilde{g}}$, $\mu = -400$ GeV/c^2, $\tan\beta = 2$													
2	180	200	30.6	67.8	67.0	67.4	26.6	48.5	0.006	0.667	0.004	4.03	0.01
3	198	220	33.6	73.6	72.9	72.2	37.1	51.0	0.008	0.667	0.005	2.80	0.01
4	216	240	36.7	79.5	78.8	77.2	46.0	53.6	0.011	0.667	0.007	1.93	0.01
5	234	260	39.8	85.3	84.7	82.2	54.0	56.3	0.016	0.667	0.010	1.38	0.01
6	252	280	42.9	91.3	90.7	87.3	61.5	59.2	0.022	0.667	0.014	1.05	0.02
7	270	300	46.0	97.2	96.7	92.4	68.6	62.0	0.028	0.667	0.019	0.80	0.02

Table 5.6: Input and output parameters for the SiMSSM points scanned. All masses are in GeV/c^2 and all σ are in picobarns.

	Input		Output										
Set	$\tilde{q}$ (GeV/c^2)	$\tilde{g}$	$\tilde{\chi}_1^0$	$\tilde{\chi}_2^0$	$\tilde{\chi}_1^\pm$	$\widetilde{\ell}_L$	$\widetilde{\nu}$	$\widetilde{\ell}_R$	BR$\to\ell\ell$ $\tilde{\chi}_2^0$	BR$\to\ell\nu$ $\tilde{\chi}_1^\pm$	BR$\to 3\ell$ Total	σ	$\sigma\cdot$BR
			(GeV/c^2)										
M$_{\tilde{q}}$ = 0.95 M$_{\tilde{g}}$, $\mu = -400$ GeV/c^2, $\tan\beta = 2$													
2	190	200	30.2	67.2	66.3	90.8	66.4	77.8	0.017	0.620	0.010	4.49	0.05
3	209	220	33.3	72.9	72.2	98.5	76.5	84.1	0.197	0.576	0.114	3.09	0.35
4	228	240	36.3	78.7	78.0	106.2	86.2	90.6	0.250	0.549	0.137	2.16	0.30
5	247	260	39.4	84.5	83.9	114.0	95.7	97.1	0.283	0.525	0.149	1.56	0.23
6	266	280	42.5	90.4	89.8	121.9	105.0	103.7	0.305	0.503	0.154	1.18	0.18
7	285	300	45.5	96.2	95.7	129.9	114.1	110.3	0.321	0.482	0.155	0.89	0.14

1. a top quark mass of $\approx$ 175 GeV/c^2;
2. light $\tilde{\chi}_1^\pm$ and $\tilde{\chi}_2^0$: M$_{\tilde{\chi}_1^\pm} \approx$ M$_{\tilde{\chi}_2^0} \leq$ 90 GeV/c^2;
3. light $\widetilde{\ell}_R$: M$_{\widetilde{\ell}_R} \approx$ 45-50 GeV/c^2 $<$ M$_{\tilde{\chi}_2^0} <$ M$_{\widetilde{\ell}_L}$;
4. M$_{\tilde{q}} \approx$ 0.98 M$_{\tilde{g}}$.

In this model, the trilepton signal is nearly maximized because the $\tilde{\chi}_2^0$ decays exclusively to dileptons with dominant two-body decay modes $\tilde{\chi}_2^0 \to \ell^\pm \widetilde{\ell}_R^\mp$ ($BR = 66\%$ for e and μ) and $\widetilde{\ell}_R \to \ell \tilde{\chi}_1^0$ ($BR = 100\%$). This results in a final state with three leptons and $\not{E}_T$ (Figures 2.18 and 2.20). Since we observe zero trilepton events, we set limits on this model using ISAJET[9] with parameters supplied by J. Lopez (as listed in Table 5.7) [48].

Figure 5.17 shows the acceptance for this model as a function of $\tilde{\chi}_1^\pm$ mass. The acceptance decreases for large $\tilde{\chi}_1^\pm$ masses as the $\tilde{\chi}_1^0$ mass approaches the $\widetilde{\ell}_R$ mass (see Table 5.8) and carries away much of the energy, resulting in soft leptons. As shown in Figure 5.18, we exclude

$$M_{\tilde{\chi}_1^\pm} < 80.5 \text{ GeV/c}^2 \tag{5.2}$$

$$\sigma_{\tilde{\chi}_1^\pm \tilde{\chi}_2^0} \cdot BR(\tilde{\chi}_1^\pm \tilde{\chi}_2^0 \to 3\ell + X) > 0.4 \text{ pb.} \tag{5.3}$$

This is comparable to the ALEPH limit of 83 GeV/c^2 [47]. We do not entirely exclude the SU(5)$\times$U(1) Supergravity model. However, our analysis excludes the model for small and moderate $\tilde{\chi}_1^\pm$ masses and leaves only a small window for $\tilde{\chi}_1^\pm$s heavier than 80.5 GeV/c^2.

[9]We use ISAJET 7.06 for this section of this analysis. It does not have explicit Supergravity input parameters. However, J. Lopez calculated the necessary input parameters for use with ISAJET 7.06.

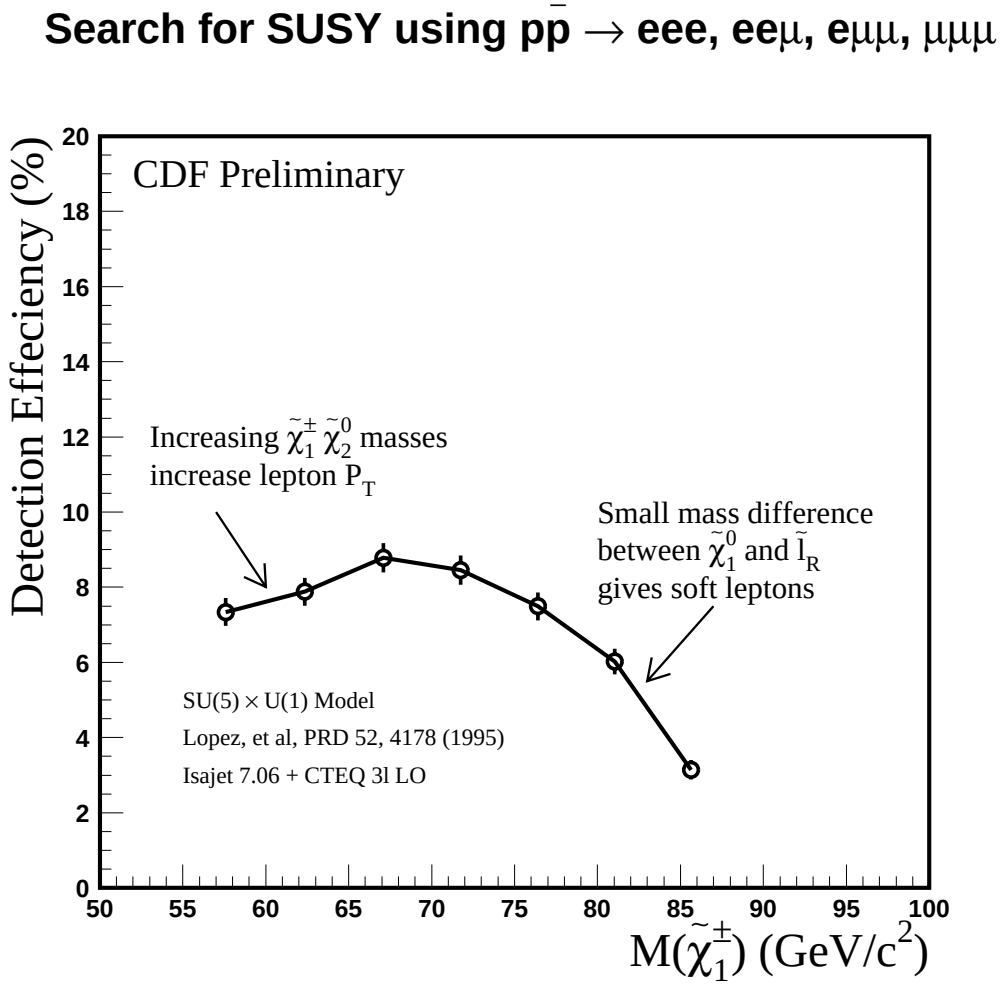

Figure 5.17: The acceptance for all four trilepton modes for SU(5) × U(1) model production of trileptons. The acceptance decreases for large $\tilde{\chi}_1^{\pm}$ masses as the $\tilde{\chi}_1^0$ mass approaches the $\tilde{\ell}_R$ mass and carries away much of the energy, resulting in soft leptons. The error bars indicate the statistical uncertainty.

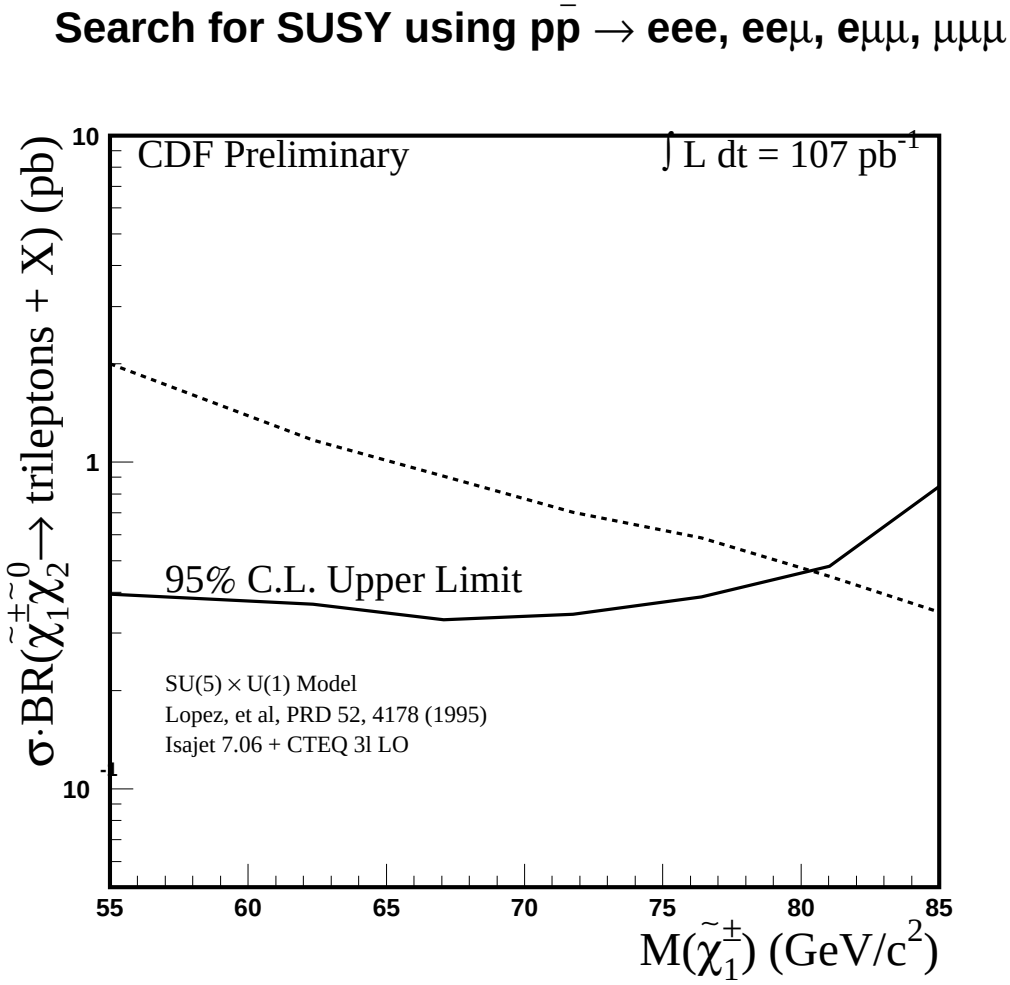

Figure 5.18: $\sigma \cdot BR$ versus $\tilde{\chi}_1^{\pm}$ mass for SU(5) $\times$ U(1) model production of trileptons. This sets a mass limit of 80.5 GeV/c^2 and a cross section times branching ratio limit of 0.4 pb.

Table 5.7: The input and output parameters used to examine the SU(5)×U(1) model. These values are courtesy of Jorge Lopez. Note that tan $\beta = 1.4$ for the entire set and all masses are in GeV/c^2.

$M_{\tilde{g}}$	$M_{\tilde{q}}$	$M_{\tilde{\ell}_L}$	$M_{\tilde{\ell}_R}$	$M_{\tilde{\nu}_L}$	$M_{\tilde{t}_L}$	$M_{\tilde{t}_R}$	A_t	$M_{\tilde{b}_L}$	$M_{\tilde{b}_R}$	μ	M_{H_A}
310.2	302.9	107.1	44.4	85.2	197.0	394.6	−211.7	328.7	308.9	242.3	295.0
322.9	315.6	111.0	45.1	89.9	205.0	405.5	−220.4	342.0	321.4	252.2	306.6
335.7	328.3	114.8	45.8	94.6	213.1	416.5	−229.1	355.4	333.9	262.1	318.3
348.4	341.0	118.7	46.6	99.2	221.4	427.5	−237.8	368.7	346.5	271.9	329.8
361.2	353.6	122.7	47.3	103.8	229.7	438.5	−246.5	382.1	359.0	281.7	341.5
373.9	366.3	126.6	48.1	108.3	238.3	449.6	−255.2	395.5	371.5	291.3	352.8
386.6	378.9	130.5	48.8	112.9	246.8	460.7	−263.9	408.9	384.1	301.0	364.3

Table 5.8: Masses of the $\tilde{\chi}_1^{\pm}$, $\tilde{\chi}_2^0$, $\tilde{\chi}_1^0$ for the points examined in the SU(5)×U(1) model. For comparison, the difference in masses between the $\tilde{\chi}_1^{\pm}$ and the $\tilde{\ell}_R$ and the detection efficiency are shown. We have reasonable efficiency as long as the mass difference is ≥ 5 GeV/c^2. All masses are in GeV/c^2 and the efficiency is in %.

$M_{\tilde{g}}$	$M_{\tilde{\chi}_1^{\pm}}$	$M_{\tilde{\chi}_2^0}$	$M_{\tilde{\chi}_1^0}$	$M_{\tilde{\ell}_R}$-$M_{\tilde{\chi}_1^0}$	efficiency
310.2	57.5	67.0	29.1	15.2	7.3
322.9	62.3	70.8	32.1	12.9	7.9
335.7	67.0	74.7	35.0	10.7	8.8
348.4	71.7	78.6	37.8	8.7	8.5
361.2	76.4	82.6	40.6	6.7	7.5
373.9	81.0	86.7	43.2	4.8	6.0
386.6	85.6	90.8	45.8	3.0	3.1

5.4.2 SUGRA

The SiMSSM as we have examined it only unifies the electromagnetic, weak and strong forces. Supergravity (or SUGRA) [49] also unifies gravity with the other three forces [13, 14]. SUGRA has a nice feature in that gauge symmetry-breaking is induced at the weak scale as a requirement of the model. However, it is a more constrained model than the SiMSSM so limits set using SUGRA are not as general. It has four and one-half free parameters: m_0, the common scalar mass; $m_{1/2}$, the common gaugino mass; the *sign* of μ; $\tan\beta$; and A_t. As seen in Section 5.3, the trilepton analysis strongly depends on the squark to gluino mass ratio and μ. These parameters are not free in the context of SUGRA which makes it more difficult to understand a limit at a particular point in SUGRA space.

SUGRA is currently quite popular, so, despite its limitations, we have examined several

points in SUGRA space. Figure 5.19 shows the detection efficiency as a function of $M_{\tilde{\chi}_1^\pm}$. Since the squark to gluino mass ratio and μ are now set inside the model, it is impossible to plot limits as a function of them. Therefore, we plot many different theoretical $\sigma_{\tilde{\chi}_1^\pm\tilde{\chi}_2^0}\cdot\mathrm{BR}(\tilde{\chi}_1^\pm\tilde{\chi}_2^0 \to 3\ell + X)$ points on the same plot for comparison with a single 95% C.L. limit curve in Figure 5.20. As before, we use ISAJET 7.20 with the CTEQ3l parton distribution function. The values of μ tend to be rather low, and as seen in Figure 5.9 that degrades our limit setting ability. We set $\tan\beta = 2$, A = 0 and require $\mu < 0$. We exclude

$$M_{\tilde{\chi}_1^\pm} < 62\ \mathrm{GeV/c^2} \tag{5.4}$$

$$\sigma_{\tilde{\chi}_1^\pm\tilde{\chi}_2^0} \cdot BR(\tilde{\chi}_1^\pm\tilde{\chi}_2^0 \to 3\ell + X) > 0.5\ \mathrm{pb}. \tag{5.5}$$

Tables 5.9-5.13 list the input and output parameters used.

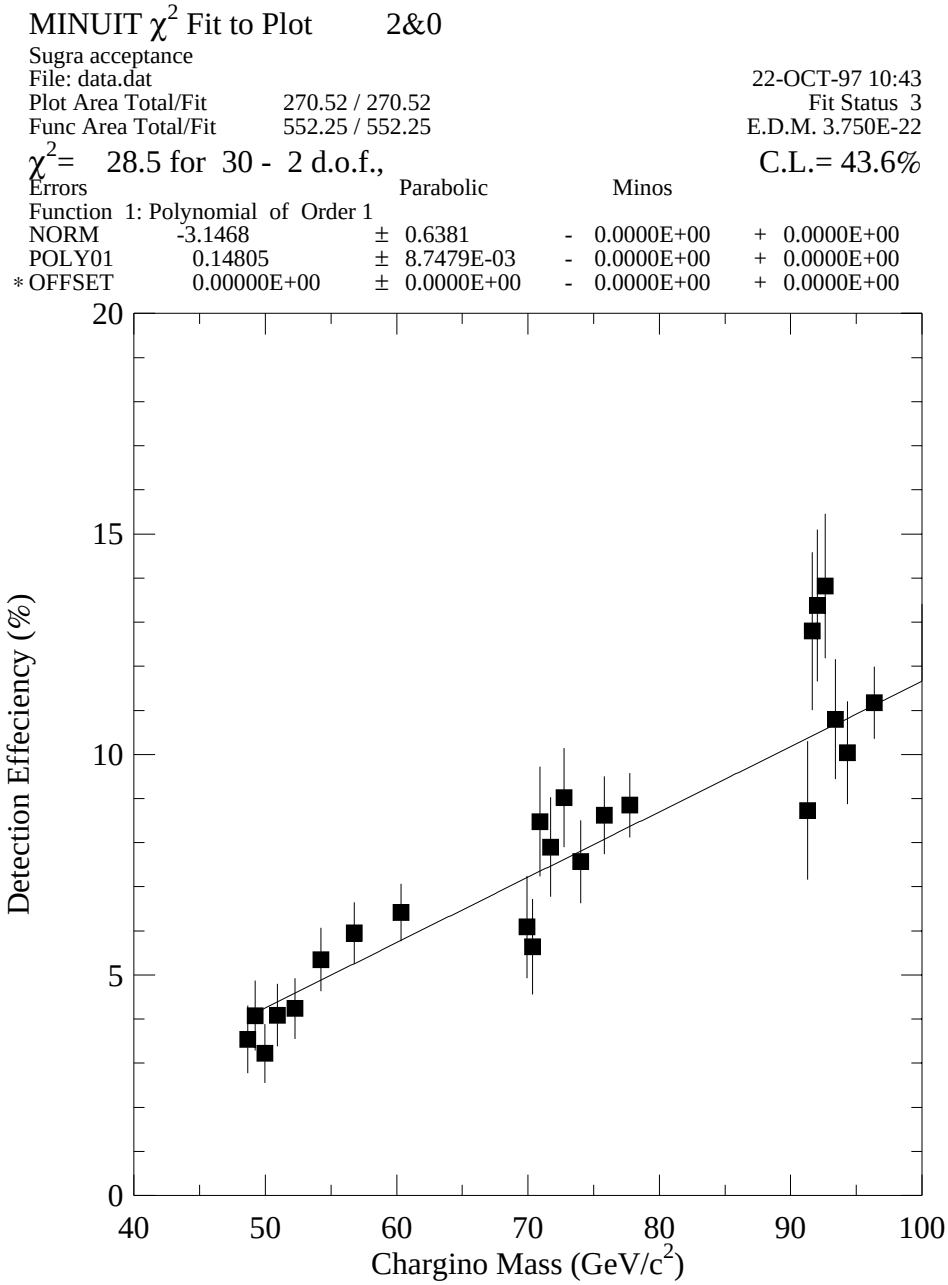

Figure 5.19: Detection efficiency as a function of $M_{\tilde{\chi}_1^\pm}$ in the framework of the SUGRA model.

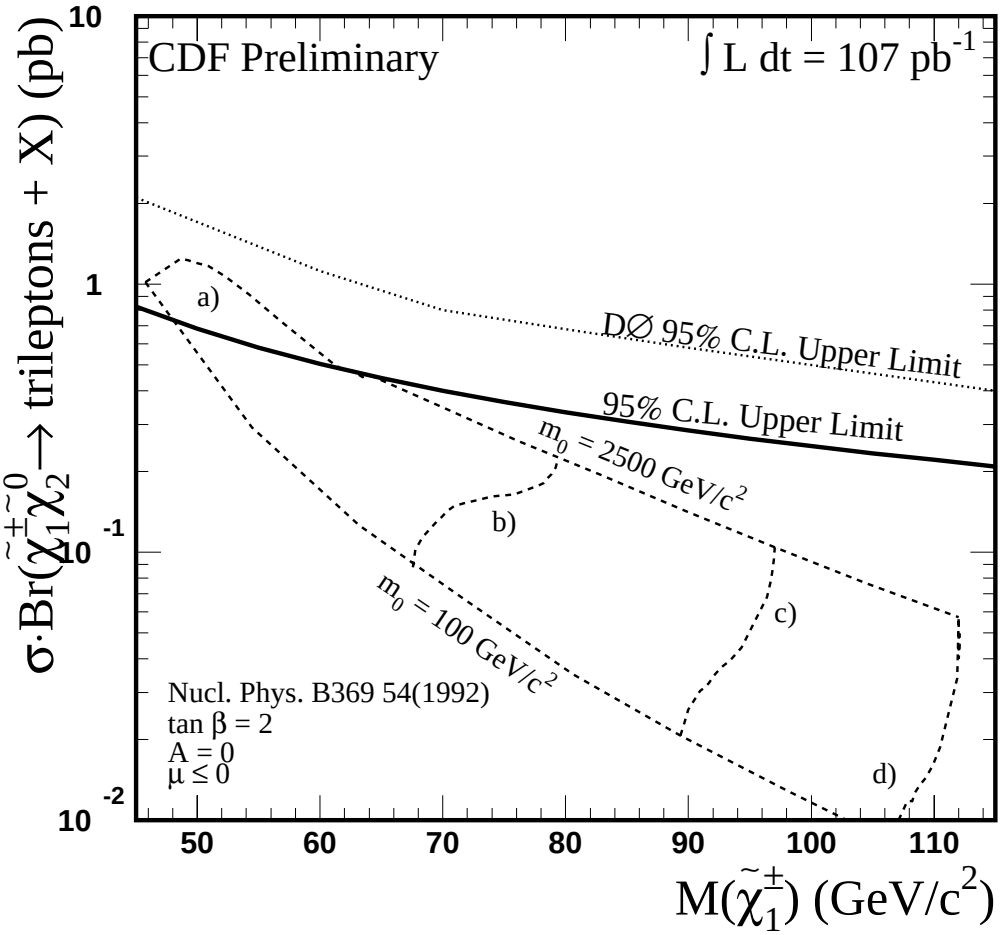

Figure 5.20: Production cross section times branching ratio to leptons for $\tilde{\chi}_1^{\pm}\tilde{\chi}_2^0$ production as a function of $\tilde{\chi}_1^{\pm}$ mass within the SUGRA framework (dashed lines). The solid line is the 95% C.L. limit curve; all points above it are excluded. We set $\tan\beta = 2$, A = 0 and require $\mu \leq 0$. For lines a)-d) we set 100 GeV/c^2 $\leq$ m$_0$ $\leq$ 2500 GeV/c^2 and (a) m$_{1/2}$ = 50 GeV/c^2, (b) m$_{1/2}$ = 75 GeV/c^2, (c) m$_{1/2}$ = 100 GeV/c^2 and (d) m$_{1/2}$ = 120 GeV/c^2 . For the lines m$_0$ = 100 GeV/c^2 and 2500 GeV/c^2 we set 50 $\leq$ m$_{1/2}$ $\leq$ 120 GeV/c^2. For comparison we show the D0 95% C.L. limit curve (dotted line).

Table 5.9: Input and output parameters for the SUGRA points scanned. All masses are in GeV/c^2. m_0 and $m_{1/2}$ are input parameters and μ is an output parameter.

Set	m_0	$m_{1/2}$	μ	Set	m_0	$m_{1/2}$	μ
1	200	50	-186.069	b1	100	75	-163.662
2	300	50	-266.678	b2	120	75	-172.144
3	400	50	-350.862	b3	140	75	-183.200
4	500	50	-444.768	b4	160	75	-194.698
5	600	50	-536.425	b5	180	75	-205.839
6	700	50	-623.811	b6	1000	75	-893.558
7	800	50	-714.489	b7	1500	75	-1345.179
8	900	50	-805.791	b8	2000	75	-1813.768
9	200	75	-219.498	b9	2500	75	-2240.462
10	300	75	-291.085	c1	100	100	-207.422
11	400	75	-371.920	c2	120	100	-214.530
12	500	75	-456.418	c3	140	100	-222.741
13	600	75	-542.042	c4	160	100	-231.186
14	700	75	-630.116	c5	180	100	-241.346
15	800	75	-716.663	c6	1000	100	-880.959
16	900	75	-803.768	c7	1500	100	-1315.166
17	200	100	-252.082	c8	2000	100	-1750.734
19	400	100	-386.463	c9	2500	100	-2216.317
20	500	100	-464.421	d1	100	120	-241.032
21	600	100	-545.403	d2	120	120	-246.732
22	700	100	-627.902	d3	140	120	-253.473
23	800	100	-709.089	d4	160	120	-261.335
24	900	100	-794.251	d5	180	120	-269.867
25	200	120	-279.473	d6	1000	120	-886.271
26	300	120	-335.698	d7	1500	120	-1313.595
27	400	120	-404.963	d8	2000	120	-1760.341
28	500	120	-476.957	d9	2500	120	-2198.631
29	600	120	-552.079	e1	2500	40	-2273.547
30	700	120	-633.072	e2	2500	50	-2274.281
31	800	120	-714.718	e3	2500	60	-2271.083
32	900	120	-794.095	e4	2500	70	-2244.072
a1	180	50	-170.656	e5	2500	80	-2259.290
a2	160	50	-156.111	e6	2500	90	-2209.621
a3	140	50	-144.023	e7	2500	100	-2216.317
a4	120	50	-129.635	e8	2500	110	-2213.630
a5	100	50	-117.714	e9	2500	120	-2198.631

Table 5.10: Input and output parameters for the SUGRA points scanned. All masses are in GeV/c^2. m_0 and $m_{1/2}$ are input parameters and μ is an output parameter.

Set	m_0	$m_{1/2}$	μ	Set	m_0	$m_{1/2}$	μ
f1	100	40	-99.201	f6	100	90	-189.670
f2	100	50	-117.714	f7	100	100	-207.422
f3	100	60	-135.514	f8	100	110	-224.225
f4	100	70	-153.708	f9	100	120	-241.032
f5	100	80	-172.995				

Table 5.11: Output parameters for the SUGRA points scanned. All σ are in picobarns.

Set	$\tilde{q}$	$\tilde{g}$	$\tilde{\chi}_1^0$	$\tilde{\chi}_2^0$	$\tilde{\chi}_1^\pm$	$\tilde{\ell}_L$	$\tilde{\nu}$	$\tilde{\ell}_R$	BR$\to\ell\ell$	BR$\to\ell\nu$	BR$\to 3\ell$	σ	$\sigma\cdot$BR
				(GeV/c^2)					$\tilde{\chi}_2^0$	$\tilde{\chi}_1^\pm$	Total		
1	237.3	168.0	23.5	62.3	60.3	206.5	197.0	203.8	0.33	0.22	0.07	7.55	0.54
2	324.3	173.1	23.2	58.5	56.8	304.4	298.0	302.5	0.26	0.22	0.06	12.85	0.73
3	417.8	177.1	23.0	55.5	54.2	403.3	398.5	401.9	0.22	0.22	0.05	18.87	0.92
4	513.6	179.2	22.8	53.2	52.3	502.6	498.8	501.5	0.19	0.22	0.04	24.78	1.07
5	611.0	181.3	22.7	51.7	50.9	602.2	599.0	601.3	0.17	0.22	0.04	30.26	1.17
6	709.2	183.5	22.6	50.6	50.0	701.8	699.1	701.1	0.16	0.22	0.03	34.66	1.20
7	807.9	185.5	22.5	49.7	49.2	801.6	799.2	801.0	0.14	0.22	0.03	38.88	1.23
8	906.9	188.0	22.4	49.0	48.6	901.4	899.3	900.8	0.13	0.22	0.03	42.84	1.24
9	275.0	236.5	34.1	78.9	77.8	210.4	201.1	204.9	0.34	0.22	0.07	2.37	0.18
10	351.0	240.6	33.9	76.8	75.8	307.0	300.7	303.3	0.23	0.22	0.05	3.24	0.16
11	438.6	246.8	33.6	74.8	74.0	405.2	400.5	402.5	0.18	0.22	0.04	4.09	0.16
12	530.2	252.0	33.4	73.3	72.7	504.2	500.4	502.0	0.15	0.22	0.03	4.77	0.16
13	624.8	255.9	33.2	72.2	71.7	603.5	600.3	601.7	0.13	0.22	0.03	5.36	0.15
14	720.7	258.9	33.1	71.3	70.9	703.0	700.2	701.4	0.11	0.22	0.03	5.84	0.15
15	817.9	262.0	33.0	70.7	70.3	802.6	800.2	801.2	0.10	0.22	0.02	6.19	0.14
16	915.3	261.6	33.0	70.2	69.9	902.3	900.2	901.1	0.10	0.22	0.02	6.39	0.14
17	316.7	298.4	44.5	97.0	96.4	215.7	206.6	206.5	0.33	0.22	0.07	0.92	0.07
19	465.9	314.2	44.0	94.8	94.3	408.0	403.2	403.3	0.15	0.22	0.03	1.34	0.04
20	552.4	319.1	43.9	93.8	93.4	506.4	502.6	502.6	0.12	0.22	0.03	1.52	0.04
21	642.9	323.4	43.7	93.0	92.6	605.3	602.1	602.2	0.10	0.22	0.02	1.67	0.04
22	736.4	327.7	43.6	92.3	92.0	704.5	701.8	701.9	0.09	0.22	0.02	1.78	0.03
23	830.8	327.5	43.7	91.9	91.7	803.9	801.5	801.6	0.08	0.22	0.02	1.85	0.03
24	926.8	330.7	43.6	91.5	91.3	903.5	901.4	901.5	0.07	0.22	0.02	1.93	0.03
25	352.2	346.8	52.8	112.3	111.9	220.9	212.0	208.1	0.33	0.23	0.07	0.46	0.03
27	489.8	361.8	52.4	110.8	110.5	410.7	406.0	404.1	0.14	0.22	0.03	0.63	0.02
28	571.3	364.3	52.4	110.2	109.9	508.5	504.7	503.3	0.10	0.22	0.02	0.71	0.02
29	659.9	374.0	52.2	109.6	109.3	607.1	603.9	602.7	0.08	0.22	0.02	0.77	0.01
30	750.6	378.6	52.1	109.0	108.8	706.1	703.3	702.3	0.07	0.22	0.02	0.83	0.01
31	844.0	379.4	52.0	108.7	108.5	805.3	802.9	802.1	0.07	0.22	0.01	0.86	0.01
32	938.1	382.9	52.1	108.4	108.2	904.7	902.6	901.8	0.06	0.22	0.01	0.88	0.01
a1	220.8	166.8	23.5	63.1	61.2	187.2	176.7	184.2	0.35	0.22	0.08	6.64	0.50
a2	205.6	165.5	23.6	63.8	62.0	168.1	156.3	164.7	0.37	0.22	0.08	5.89	0.48
a3	191.5	164.5	23.6	64.1	62.6	149.2	135.7	145.4	0.41	0.22	0.09	5.30	0.48
a4	178.0	163.3	23.6	64.3	63.4	130.6	115.0	126.2	0.44	0.22	0.10	4.55	0.45
a5	166.0	161.8	23.7	64.1	64.1	112.6	94.0	107.4	0.48	0.23	0.11	4.07	0.46

Table 5.12: Output parameters for the SUGRA points scanned. All σ are in picobarns.

Set	$\tilde{q}$	$\tilde{g}$	$\tilde{\chi}_1^0$	$\tilde{\chi}_2^0$	$\tilde{\chi}_1^\pm$	$\tilde{\ell}_L$	$\tilde{\nu}$	$\tilde{\ell}_R$	BR$\to\ell\ell$	BR$\to\ell\nu$	BR$\to 3\ell$	σ	$\sigma\cdot$BR
	(GeV/c^2)								$\tilde{\chi}_2^0$	$\tilde{\chi}_1^\pm$	Total		
b1	218	230	34.3	79.9	79.4	119.7	102.4	109.6	0.46	0.29	0.13	1.68	0.22
b2	226	229	34.3	79.9	79.2	136.8	122.0	128.1	0.46	0.25	0.12	1.78	0.21
b3	237	232	34.2	79.8	78.9	154.6	141.7	147.0	0.44	0.24	0.10	1.91	0.20
b4	248	233	34.2	79.5	78.5	172.9	161.4	166.1	0.40	0.23	0.09	2.06	0.19
b5	261	233	34.2	79.2	78.2	191.5	181.2	185.5	0.37	0.22	0.08	2.21	0.18
b6	1013	264	33.0	69.8	69.5	1002.1	1000.1	1001.0	0.09	0.22	0.02	6.63	0.13
b7	1508	272	32.8	68.5	68.4	1501.4	1500.1	1500.7	0.07	0.22	0.02	7.39	0.11
b8	2006	275	32.7	67.8	67.8	2001.0	2000.0	2000.5	0.06	0.22	0.01	7.73	0.10
b9	2504	284	32.7	67.6	67.6	2500.8	2500.0	2500.4	0.05	0.22	0.01	7.86	0.09
c1	269	291	44.7	97.4	97.0	128.9	113.0	112.6	0.40	0.36	0.14	0.74	0.10
c2	276	293	44.6	97.4	97.0	144.9	131.0	130.6	0.42	0.29	0.12	0.77	0.09
c3	285	294	44.6	97.4	96.8	161.8	149.4	149.2	0.41	0.26	0.11	0.80	0.08
c4	294	295	44.6	97.3	96.7	179.3	168.3	168.1	0.39	0.24	0.09	0.84	0.08
c5	305	297	44.6	97.2	96.6	197.3	187.4	187.2	0.36	0.23	0.08	0.88	0.07
c6	1023	334	43.6	91.1	90.9	1003.1	1001.2	1001.3	0.07	0.22	0.02	2.01	0.03
c7	1514	344	43.4	90.1	90.0	1502.1	1500.8	1500.9	0.05	0.22	0.01	2.17	0.03
c8	2010	353	43.4	89.7	89.6	2001.5	2000.6	2000.7	0.05	0.22	0.01	2.24	0.02
c9	2508	355	43.5	89.4	89.4	2501.2	2500.4	2500.5	0.04	0.22	0.01	2.25	0.02
d1	310	340	52.9	112.3	112.0	137.4	122.6	115.5	0.36	0.41	0.15	0.39	0.06
d2	316	342	52.9	112.4	112.1	152.5	139.4	133.2	0.39	0.32	0.12	0.40	0.05
d3	324	343	52.9	112.4	112.1	168.6	156.8	151.4	0.39	0.27	0.11	0.41	0.04
d4	332	344	52.9	112.4	112.0	185.5	174.9	170.1	0.38	0.25	0.09	0.43	0.04
d5	342	345	52.9	112.3	112.0	203.0	193.3	189.0	0.35	0.23	0.08	0.44	0.04
d6	1033	384	52.0	108.0	107.8	1004.2	1002.3	1001.6	0.06	0.22	0.01	0.92	0.01
d7	1521	395	52.0	107.2	107.1	1502.8	1501.5	1501.1	0.05	0.22	0.01	0.99	0.01
d8	2015	406	52.1	106.9	106.8	2002.1	2001.1	2000.8	0.04	0.22	0.01	1.03	0.01
e1	2501	168	17.7	37.1	37.1	2500.4	2499.7	2500.3	0.07	0.22	0.02	3482	55.0
e2	2502	201	22.0	45.8	45.8	2500.5	2499.7	2500.3	0.06	0.22	0.01	72.02	1.02
e3	2502	234	26.3	54.5	54.5	2500.6	2499.8	2500.3	0.06	0.22	0.01	22.62	0.29
e4	2504	267	30.6	63.2	63.2	2500.7	2500.0	2500.4	0.05	0.22	0.01	10.81	0.13
e5	2505	295	34.9	71.9	71.9	2500.9	2500.1	2500.4	0.05	0.22	0.01	5.99	0.07
e6	2506	329	39.1	80.7	80.6	2501.0	2500.3	2500.5	0.04	0.22	0.01	3.58	0.03
e7	2508	355	43.5	89.4	89.4	2501.2	2500.4	2500.5	0.04	0.22	0.01	2.25	0.02
e8	2509	383	47.8	98.2	98.1	2501.4	2500.6	2500.6	0.04	0.22	0.01	1.50	0.01
e9	2511	411	52.1	106.7	106.7	2501.6	2500.9	2500.7	0.04	0.22	0.01	1.05	0.01

Table 5.13: Output parameters for the SUGRA points scanned. All σ are in picobarns.

Set	$\tilde{q}$	$\tilde{g}$	$\tilde{\chi}_1^0$	$\tilde{\chi}_2^0$	$\tilde{\chi}_1^\pm$	$\widetilde{\ell}_L$	$\widetilde{\nu}$	$\widetilde{\ell}_R$	BR$\rightarrow\ell\ell$	BR$\rightarrow\ell\nu$	BR$\rightarrow 3\ell$	σ	$\sigma\cdot$BR
				(GeV/c^2)					$\tilde{\chi}_2^0$	$\tilde{\chi}_1^\pm$	Total		
f1	147.6	136.6	19.2	57.9	58.9	110.5	91.5	106.8	0.45	0.21	0.09	5.94	0.56
f2	166.0	161.8	23.7	64.1	64.1	112.6	94.0	107.4	0.48	0.23	0.11	4.07	0.46
f3	186.5	189.2	28.0	70.3	69.9	115.1	97.1	108.2	0.49	0.25	0.12	2.82	0.35
f4	207.0	215.0	32.3	76.7	76.2	118.1	100.5	109.1	0.47	0.28	0.13	1.99	0.26
f5	228.8	243.2	36.4	83.3	82.8	121.4	104.4	110.1	0.45	0.30	0.14	1.44	0.20
f6	249.2	268.1	40.5	90.2	89.8	125.0	108.6	111.3	0.42	0.33	0.14	1.03	0.14
f7	269.4	291.9	44.7	97.4	97.0	128.9	113.0	112.6	0.40	0.36	0.14	0.74	0.10
f8	290.6	318.0	48.8	104.8	104.5	133.0	117.7	114.0	0.37	0.38	0.14	0.54	0.08
f9	310.8	340.8	52.9	112.3	112.0	137.4	122.6	115.5	0.36	0.41	0.15	0.39	0.06

Chapter 6

Conclusion

We have searched for evidence of Supersymmetry using the CDF detector and the Fermilab Tevatron. After searching 107 pb^{-1} for three lepton events, we find no evidence for $\tilde{\chi}_1^{\pm}\tilde{\chi}_2^0$ production.

We set limits on $\mathrm{M}_{\tilde{\chi}_1^{\pm}}$ and $\sigma_{\tilde{\chi}_1^{\pm}\tilde{\chi}_2^0}\cdot\mathrm{BR}(\tilde{\chi}_1^{\pm}\tilde{\chi}_2^0 \rightarrow 3\ell + X)$ in several models. Table 6.1 lists the limits for a general MSSM, Table 6.2 lists the limit for the SU(5)×U(1) supergravity model, and Table 6.3 lists the limits for a general SUGRA model.

In Section 2.5 I introduced the concept of naturalness. In Figure 2.21 we see the naturalness of the $\tilde{\chi}_1^{\pm}$. The limit set by this analysis is well away from the minimum in that plot and begins to approach non-natural (or unlikely) values. Also, if the model assumptions we make are correct, we see that the naturalness of the squark, gluino and slepton masses are starting to move away from their most natural values (see Figure 6.1). We are beginning to challenge SUSY.

It is appropriate to wonder what reach the Tevatron will have during Run II. At high gluino mass the best search mode is $\tilde{\chi}_1^{\pm}\tilde{\chi}_2^0$ or $\tilde{\chi}_1^{\pm}\tilde{\chi}_1^{\pm}$: the production cross section for gluinos and squarks becomes quite small (as seen in Figure 6.2), while the $\tilde{\chi}_1^{\pm}$ and $\tilde{\chi}_2^0$ masses tend to be $\sim 1/3$ the gluino masses. Table 6.4 lists the upper reach for CDF during Run II, for either 1 or 2 fb^{-1}.

Either Supersymmetry will be discovered during Run II at the Tevatron or its viability as a physically acceptable theory will be greatly compromised.

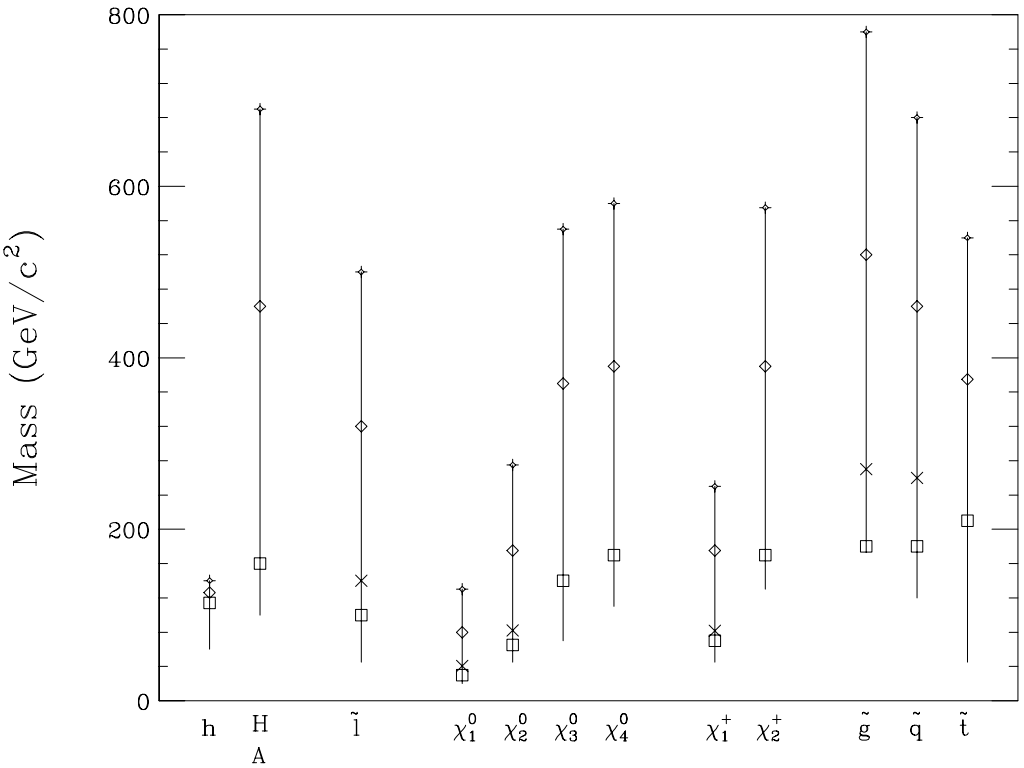

Figure 6.1: The naturalness for a variety of different sparticles. The bottom of each line is the world limit prior to this analysis, the box (□) represents a naturalness of 1, the diamond (◇) a naturalness of 5 and the top of the line (+) a naturalness of 10. The limits from this analysis (primarily for $\tilde{\chi}_1^{\pm}$ and $\tilde{\chi}_2^0$, but also for $\widetilde{\ell}$, $\tilde{g}$ and $\tilde{q}$) are represented by the cross (×). We have excluded the most natural values. Adapted from Ref. [25].

Table 6.1: Limits on chargino and neutralino masses within the framework of the SUGRA-inspired MSSM. All masses are in GeV/c^2.

Input Parameters				Limits			
$M_{\tilde{g}}$	$M_{\tilde{q}}$	$\tan\beta$	μ	$M_{\tilde{\chi}_1^\pm}$	$M_{\tilde{\chi}_2^0}$	$M_{\tilde{\chi}_1^0}$	$\sigma\cdot$ BR (pb)
220	330	2	-400	68.0	69.0	29.2	0.45
220	264	2	-400	71.0	72.1	32.0	0.40
200	200	2	-200	72.5	73.4	30.7	0.40
240	240	2	-400	76.5	77.1	36.1	0.37
260	260	2	-600	81.5	82.2	38.1	0.34
270	270	2	-800	81.0	81.0	39.3	0.35
260	260	2	-1000	78.5	78.4	37.5	0.36
200	500	2	-400	58.0	59.0	26.4	0.60

Table 6.2: Limits on chargino and neutralino masses within the framework of the SU(5)×U(1) model. All masses are in GeV/c^2. Recall for this model $\tan\beta = 1.4$.

Input Parameters			Limits			
$M_{\tilde{g}}$	$M_{\tilde{q}}$	μ	$M_{\tilde{\chi}_1^\pm}$	$M_{\tilde{\chi}_2^0}$	$M_{\tilde{\chi}_1^0}$	$\sigma\cdot$ BR (pb)
373.9	366.3	291.3	81.0	86.7	43.2	0.4

Table 6.3: Limits on chargino and neutralino masses within the framework of SUGRA. All masses are in GeV/c^2. Recall we used $\tan\beta = 2$ and $A = 0$.

Input parameters		Limits						
m_0	$m_{1/2}$	$M_{\tilde{g}}$	$M_{\tilde{q}}$	μ	$M_{\tilde{\chi}_1^\pm}$	$M_{\tilde{\chi}_2^0}$	$M_{\tilde{\chi}_1^0}$	$\sigma\cdot$ BR (pb)
200	50	237.3	168.0	-186.1	62.3	60.3	23.5	0.5

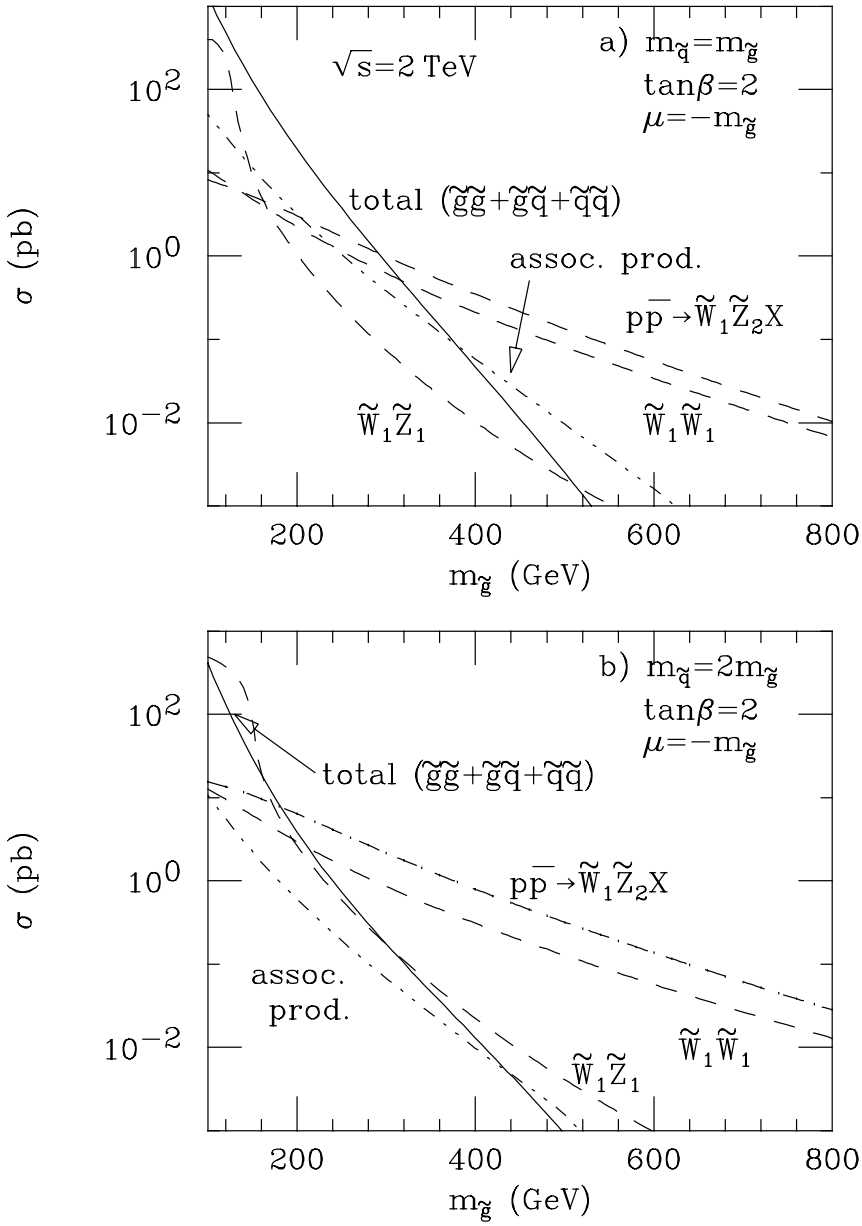

Figure 6.2: Production cross section for a variety of processes at the upgraded Tevatron. Clearly, the best search modes are $\tilde{\chi}_1^{\pm}\tilde{\chi}_2^0$ or $\tilde{\chi}_1^{\pm}\tilde{\chi}_1^{\pm}$. Adapted from Ref. [9].

Table 6.4: Lower limits for several searches using Run II at the Tevatron. For the various gluino and squark searches, OS means searching for opposite sign dilepton + jets, SS is same sign dilepton + jets, 3ℓ is trilepton + jets, and $\not\!\!E_T$ is $\not\!\!E_T$ + jets. Adapted from Refs. [9] and [50].

Particle	Search Method	Limit (GeV/c^2) 1 fb^{-1}	2 fb^{-1}
$\tilde{\chi}_1^{\pm}\tilde{\chi}_2^0$	$3\ell + \not\!\!E_T$	150	210
$\tilde{g}$ and $\tilde{q}$:			
$m_{\tilde{q}} = m_{\tilde{g}} + 10$ GeV	$\not\!\!E_T$	260	
	OS	290	
	SS	320	
	$3\ \ell$	425	
$m_{\tilde{q}} = m_{\tilde{g}} - 10$ GeV	$\not\!\!E_T$	265	
	OS	235	
	SS	325	
	$3\ \ell$	440	
$m_{\tilde{q}} = 2m_{\tilde{g}}$	$\not\!\!E_T$	200	
	OS	180	
	SS	210	
	$3\ \ell$	260	
$\tilde{t}$	all	125	150
$\tilde{\ell}$	all	100 (for 25 fb^{-1})	

Bibliography

[1] *Webster's New World Dictionary*, 2nd College Edition, 1984.

[2] K. G. Wilson, Phys.Rev.**D10**:2445-2459 (1974); G. Altarelli and G. Parisi, Nucl.Phys. **B126**:298 (1977).

[3] S. L. Glashow, Nucl. Phys. **22**, 579-588, 1961; S. Weinberg, Phys. Rev. Lett. **19**, 1264-66, 1967; A. Salam, in *Elementary Particle Theory*, N. Svartholm, ed. (Stockholm: Almquist and Wiksell, 1968).

[4] F. Abe, *et al.* (The CDF Collaboration), March 1995, Phys. Rev. Lett. **74**:2626-2631,1995.

[5] Particle Data Group, *Review of Particle Physics*, Phys. Rev. **D54**, 1 July 1996.

[6] M. Drees and S. Martin, *Implications of SUSY Model Building*, Report of the DPF Working Group on "Electroweak Symmetry Breaking and Beyond the Standard Model",March 1995, hep-ph/9504324.

[7] See http://www-spires.slac.stanford.edu/find/hep.

[8] M. Drees, *An Introduction to Supersymmetry*, Lectures given at Inauguration Conference of the Asia Pacific Center for Theoretical Physics (APCTP), Seoul, Korea, 4-19 Jun 1996, hep-ph/9611409.

[9] H. Baer, *et. al.*, *Low Energy Supersymmetry Phenomenology*, Report of the DPF Working Group on "Electroweak Symmetry Breaking and Beyond the Standard Model", March 1995, hep-ph/9503479.

[10] J. Lopez, Rept. Prog. Phys. **59**:819-865,1996.

[11] A.H. Chamseddine, R. Arnowitt, and P. Nath, Phys. Rev. Lett. **49**, 970 (1982); R. Barbieri, S. Ferrora, and C.A. Savoy, Phys. Lett. **B119**, 343 (1982); L. Hall, J. Lykken, and S. Weinberg, Phys. Rev. **D27**, 2359 (1983). For a recent review, see R. Arnowitt and P. Nath, "Supersymmetry and Supergravity: Phenomenology and Grand Unification," Proceedings of VIIth J.A. Swieca Summer School, Campos de Jordao, Brazil, 1993 (World Scientific, Singapore, 1994).

[12] R. Phillips and V. Barger, *Collider Physics*, Addison-Wesley (1987).

[13] L.E. Ibañez, C. Lopez, and C. Muoñz, Nucl. Phys. **B256**, 218 (1985); G.G. Ross and R.G. Roberts, Nucl. Phys. **B377**, 571 (1992); R. Arnowitt and P. Nath, Phys. Rev. Lett. **69**, 725 (1992); S. Kelley, J.L. Lopez, D.V. Nanopoulos, H. Pois, and K. Yuan, Nucl. Phys. **B398**, 31 (1993); G.L. Kane, C. Kolda, L. Roszkowski, and J.D. Wells, Phys. Rev. **D49**, 6173 (1994). In this analysis we use formulae in H.Baer *et al.*, Phys. Rev. **D47**, 2739 (1993).

[14] M.Drees and M.Nojiri, Nucl. Phys. **B369**, 54 (1992).

[15] See the references in G.L. Kane, HEPPH-9709318. Invited talk at 5th International Conference on Supersymmetries in Physics (SUSY 97), Philadelphia, PA, 27-31 May 1997.

[16] For example T.S. Kosmas and J.D. Vergados, Phys. Rev. **D55**:1752-1764 (1997).

[17] G. Anderson, private communication.

[18] J. Kubo, M. Mondragon and G. Zoupanos, Nucl.Phys. **B424**:291-307 (1994).

[19] D. Griffiths, *Introduction to Elementary Particles*. John Wiley & Sons, Inc, 1987.

[20] F. Halzen and A. Martin, *Quarks & Leptons: An Introductory Course in Modern Particle Physics*, John Wiley & Sons, Inc., 1984.

[21] F. Abe, *et al.* (The CDF Collaboration), Phys. Rev. Lett. **76**:2006-2010, (1996).

[22] F. Abe, *et al.* (The CDF Collaboration), Phys. Rev. Lett. **75** 1017, 1995. F. Abe, *et al.* (The CDF Collaboration), in preparation.

[23] F. Abe, *et al.*, Phys. Rev. Lett. **76**, 4307 (1996).

[24] G. Anderson and D. Castaño, Phys. Letters **B347**, 300 (1995).

[25] G. Anderson and D. Castaño, Phys. Rev. **D52**, 1693 (1995).

[26] J. Huston, FERMILAB-TM-1909 (1994).

[27] For a description of the original CDF detector, see F. Abe, *et al.*, (The CDF Collaboration), Nucl. Instrum. Methods **A271**, 387 (1988) and the references within.

[28] For a description of the CDF upgrades, see F. Abe, *et al.*, (The CDF Collaboration), Phys. Rev. **D50**, 2966 (1994); D. Amidei, *et al.*, Nucl. Instrum. Methods **A350**, 73 (1994) and the references within.

[29] A. Beretvas, *et. al*, CDF Note 3599 (1995).

[30] F. Abe, *et al.*, (The CDF Collaboration), Phys.Rev. **D50**:2966, 1994.

[31] S. Kuhlmann, *et al.*, CDF Note 413 (1986); CDF Note 282.

[32] J.P. Done *et al.*, CDF Note 4218 (1997).

[33] F. Abe, *et. al*, (The CDF Collaboration), Phys. Rev. **D 52** 2624 (1994).

[34] S. Kopp and C. Grosso-Pilcher, CDF Note 1992 (1993).

[35] M. Krasberg and T. LeCompte, CDF Note 2032 (1993).

[36] H. Baer, F.E. Paige, S.D. Protopopescu, and X. Tata, "Simulating Supersymmetry with ISAJET 7.0/ISASUSY 1.0," Proceedings of Workshop on Physics at Current Accelerators and the Supercollider, eds. J. Hewett, A. White and D. Zeppenfeld (Argonne National Laboratory, 1993).

[37] S. Tether, CDF Note 3566 (1996).

[38] The trigger efficiencies come from a variety of CDF Notes: CDF-2391, CDF-2391, CDF-2367, CDF-2186, CDF-3622, CDF-2435, XCES efficiency from CDF-2795, CDF-3060, CDF-2367, CDF-4017, CDF-2954, CDF-4076, CDF-3622, CDF-2596, CDF-2596, CDF-2367, CDF-2367, CDF-3532, CDF-3532, CDF-2191 and CDF-3028.

[39] B. Tannenbaum, CDF Note 2962 (1995).

[40] Andy Beretvas, private communication.

[41] J.P. Done *et al.*, CDF Note 4182 (1997).

[42] K. Byrum and A.B. Wicklund, CDF Note 3665 (1996). The Level 2 trigger efficiency for CEM_9_SEED_9_SH_7_CFT_9_2_V2 in Run 1A is $\epsilon_{L2} = (92.4 \pm 1.7\ ^{+3.0}_{-4.7})\%$. We shift the Run 1A trigger efficiency curve by 1 GeV and fold with XCES efficiencies (100% at plateau) from CDF Note 2795; As for the Level 1 trigger efficiency, we take the Run 1A result ($\epsilon_{L1} = (99.2 \pm 0.1)\%$) from CDF Note 2391 and shift the curve by 1 GeV for Run IB; As for the Level 3 trigger efficiency for Run IB, we take the Run 1A result ($\epsilon_{L3} = (95.2 \pm 1.5)\%$) from CDF Note 2596; The total efficiency of L1∗L2∗L3 is $(87.3^{+3.5}_{-4.9}$(stat.+syst.))%.

[43] J.P. Done *et al.*, CDF 4017 (1997). The Level 2 trigger efficiency in Run IB is $\epsilon_{L2} = (95.1 \pm 1.2 \pm 0.8)\%$; As for the Level 1 trigger efficiency, we have the Run IB result ($\epsilon_{L1} = (93.1 \pm 1.1 \pm 1.0)\%$) from CDF Note 3028; As for the Level 3 trigger efficiency, we take the Run 1A results ($\epsilon_{L3} = (98.4 \pm 0.4 \pm 2.0)\%$) from CDF Note 2596 for Run IB; The total efficiency of L1∗L2∗L3 is (87.1±2.9(stat.+syst.))% .

[44] B. Tannenbaum and T. Kamon, CDF Note 3538 (1996).

[45] Y. Kato, D.Sc. Dissertation, (1996).

[46] B. Abbott, *et al.*, hep-ex/9705015 (1997).

[47] Glen Cowen, CERN Particle Physics Seminar, 25 February 1997, http://alephwww.cern.ch/-ALPUB/seminar/cowen-172-jam/cowan.html.

[48] J. Lopez, D. Nanopoulos, A. Zichichi, Phys. Rev. **D52**, 4178 (1995) and **D53** 5253 (1996).

[49] H. Baer, *et al* Phys. Rev. D51,1046 (1995) and references within.

[50] R. Blair, *et al* (The CDF II Collaboration), *The CDF II Detector Technical Design Report*, FERMILAB-Pub-96/390-E (1996).

[51] R. Barbieri and G. F. Giudice, Nucl. Phys, **B306**, 63 (1988); J. Ellis, K. Enqvist, D.V. Nanopoulos, and F. Zwirner, Mod. Phys. Lett. **A1**, 57 (1986).

[52] F. Abe, *et. al*, (The CDF Collaboration), Phys. Rev. **D 52** 4784 (1995).